Conjugated porous polymers: incredibly versatile materials with far-reaching applications

Chem Soc Rev

REVIEW ARTICLE

Conjugated Porous Polymers: Incredibly Versatile Materials with Far-reaching Applications

Received 00th January 20xx
Accepted 00th January 20xx

DOI: 10.1039/x0xx00000x

Dominic Taylor,[a] Scott J. Dalgarno,*[a] Zhengtao Xu*[b] and Filipe Vilela*[a]

Conjugated porous polymers (CPPs) are a class of amorphous polymer networks that are, in their design, fully cross-linked and fully π-conjugated. The cross-linked nature of CPPs means that they have permanent intrinsic porosity (on the nanometer scale), which, in combination with the fully π-conjugated framework, makes these materials unique among the wider class of porous polymeric materials. In recent years, the need for new and efficient functional materials has driven the development of CPPs as versatile platforms for applications including (photo)catalysis, light harvesting, gas separation and storage, chemosensing, environmental remediation and energy storage. The efficiency of these materials towards these described applications is heavily influenced by the choice of molecular building blocks and synthetic conditions, allowing for facile tailoring and optimisation of the structure and properties. The aim of this review is to highlight select works on CPPs, including basic structural design principles, various synthetic protocols and topical applications of these versatile materials.

1 Introduction

Functional porous materials play many important roles in our society and are being intensively developed for various applications.[1–8] In addition to mimicking naturally occurring porous inorganic materials such as zeolites[9,10] and silicates,[11,12] significant attention has been recently devoted to porous polymeric materials. These include materials such as metal-organic frameworks (MOFs),[13–15] porous aromatic frameworks (PAFs),[16,17] covalent organic frameworks (COFs),[18–23] hyper-cross-linked polymers (HCPs),[24] polymers of intrinsic microporosity (PIMs),[25–28] and conjugated porous polymers (CPPs).[29,30]

Besides the overarching characteristic of porosity, each class in itself features unique aspects in methods of synthesis, physiochemical stability, degree of conjugation and origin of porosity, which can closely impact the final properties and applications of the material.[4,31]

Among porous materials, CPPs are of particular interest because they offer a convenient combination of high surface area/permanent porosity and an extended π-conjugated electronic system throughout the interconnected polymer network.[29,30] Such a powerful combination is especially conducive to various key applications including gas separation and storage, optoelectronics and energy storage,[32,33] chemical sensors,[34–36] and photocatalysis.[37–40] As a result, the field of

[a] School of Engineering and Physical Science, Heriot-Watt University, Riccarton, Edinburgh, EH14 4AS, UK. E-mail: f.vilela@hw.ac.uk, s.j.dalgarno@hw.ac.uk
[b] Department of Chemistry, City University of Hong Kong, 83 Tat Chee Avenue, Kowloon, Hong Kong. E-mail: zhengtao@cityu.edu.hk

Dominic Taylor, from Grangemouth in Scotland, was born in 1996. He received his MChem in Chemistry with Materials in 2018 from Heriot-Watt University in Edinburgh, Scotland. Choosing to remain at Heriot-Watt University, Dominic is currently undertaking a PhD under the joint supervision of Dr Filipe Vilela and Dr Scott Dalgarno as part of the EPSRC funded Critical Resource Catalysis (CRITICAT) centre for doctoral training. His research focuses on developing novel photocatalytic materials that utilise aspects of both polymer and supramolecular chemistry, in particular using calixarenes as a motif for host-guest chemistry.

Scott Dalgarno was born in Aberdeen, Scotland in 1978. He obtained both his MChem (2001) and PhD (2005) at the University of Leeds, the latter working under the supervision of Professors Colin Raston and Michaele Hardie. Following this, he took up a postdoctoral research position with Professor Jerry Atwood at the University of Missouri before being appointed as a lecturer at Heriot-Watt University and promoted to reader. He is a previous winner of the RSC Harrison Meldola Memorial Prize (2010), the inaugural Chemical Communications Emerging Investigator Lectureship (2011) and the RSC Sir Edward Frankland Fellowship (2015).

conjugated porous polymers has grown rapidly since the initial work was first reported by Cooper and coworkers in 2007.[41]

For CPPs, the general design strategy is to connect π-conjugated organic building blocks in a manner that extends the conjugation and establishes an extended network. For this purpose there are a number of bond-forming reactions which can be utilised,[42] including Suzuki-Miyuara,[39,40,43,44] Sonogashira-Hagihara,[39,45–48] or Yamamoto coupling reactions,[36,49–52] direct arylation,[53–56] as well as Friedel-Crafts type chemistry,[57–60] Schiff-base formation,[61–63] the Knoevenagel condensation,[64,65] and electropolymerisation.[66–69] Furthermore, synthetic routes can be utilised in conjunction with various templating effects to control the pore structure or with post-synthetic modification steps to alter the structure or function.

The synthetic reactions commonly used establish strong covalent bonds, which impart CPPs with superior chemical stability in comparison to COFs and MOFs, which, in contrast, rely on the reversible bond formation. CPPs have demonstrated remarkable stability towards organic solvents, hydrofluoric acid,[45,70] and even high intensity γ-radiation.[71,72] The amorphous nature of most CPPs imposes less constraint on the structures of the repeat units in comparison to crystalline porous materials. Therefore, a most useful characteristic of CPPs is derived from the diverse array of organic π-systems available for incorporation into CPPs.[73] By careful selection of building blocks, the porosity, specific surface area and optoelectronic structures of CPPs can be tailored to suit their intended application. Of particular interest is the facile integration of complex units or functionalities such as ionic charges,[74] radical species,[75] chiral centres,[76] and metal-ligand complexes (such as salen or carbene complexes)[77,78] into a solid polymeric framework. Such flexible control is vital as a CPPs structure is closely related to its properties and application.

In this review, we seek to highlight the diverse body of research that has been performed since CPPs were first reported over a decade ago. This will include a brief summary of how both the electronic structure and morphology of the CPP can heavily influence its function. Discussion of design and synthetic protocols followed by a review of reported applications covering catalysis, adsorption of gases, metals and small molecules, chemosensing and energy storage.

1.1 Structural Design and Synthesis

1.1.1 Choice of Monomer Units One salient feature of CPP materials is the broad array of suitable π-conjugated building blocks available. This diversity is important since even a slight modification of the CPP structure at the molecular level can lead to drastic variations in the materials properties. As an example, the simple conceptual design of substituting a benzene ring for a triazine ring leads to improvements in the CO_2 capture properties of the material.[79] This modification on paper exchanges CH groups for nitrogen atoms but in practice enhances interaction between adsorbate and adsorbent. Furthermore, this diversity in available building blocks allows relatively complex units to be incorporated into CPPs, leading to truly versatile heterogeneous platforms.

In order to generate an extended network, a certain fraction of the building block monomers must possess at least three distinct points for connection. This can then undergo self-condensation or react with other building blocks present, but in the latter case, the other monomers must possess at least two reactive sites in order to generate a cross-linked polymer. From a design viewpoint, CPPs are completely cross-linked, although this is not achieved when synthesising the material as defects, such as unreacted functional groups, can occur. Studies based on acetylene containing CMPs have demonstrated a mechanism for network formation.[80] The monomers react to form soluble oligomers, which combine to form larger insoluble clusters. Solid state cross-linking of these clusters leads to the formation of the microporous network.

The other criterion for forming CPPs is that the reaction between two building blocks must lead to π-conjugation across multiple monomer residues. This means that building blocks with sp^3 hybridised carbon centres that completely interrupt the π-conjugation of the polymer back-bone, such as tetra(4-bromophenyl)methane, are not suitable for constructing CPPs: there are many instances in the literature where porous organic polymers have been incorrectly defined as CPPs despite not

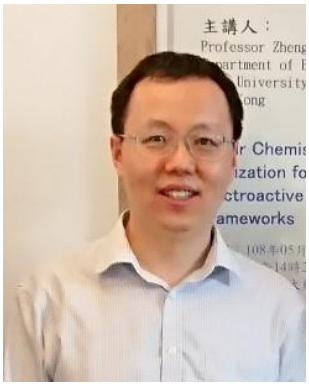

After his BS (1996) at Peking University, Zhengtao Xu had a plan for organic chemistry, only to join Stephen Lee's group at Michigan and receive a PhD from Cornell for works on coordination networks (MOFs). After a postdoc with David Mitzi (IBM, 2001-03), he moved to George Washington University as an assistant professor to open his work on sulfur-equipped MOFs. As life would have it, he then started anew in Hong Kong (from 2005), and became a professor in 2015. His group has an interest in bridging the two worlds of coordination and covalent frameworks.

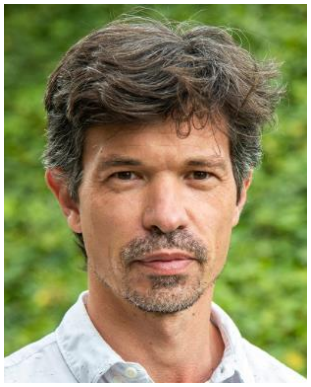

Filipe Vilela under the supervision of Professor David C. Sherrington FRS completed in 2008 his PhD in the field of polymer chemistry at the University of Strathclyde, Glasgow, Scotland. Since then Dr Vilela has worked in organic electronics (Strathclyde), and in heterogeneous photocatalysis at the Max Planck Institute of Colloids and Interfaces, Potsdam, Germany. Filipe Vilela is currently an Assistant Professor at Heriot-Watt University in Edinburgh, Scotland, with research interests centred on developing photoactive polymers for photocatalytic and sensing applications

possessing full π-conjugation. However, POPs derived from a structurally related building block, 3,3',6,6'-tetrabromo-9,9'-spirobi[fluorene], could arguably be classified CPPs as, despite possessing the spiro- carbon, the π-conjugation between adjacent monomer residues is not entirely disrupted by its presence.

1.1.2 Synthesis and Processing The general strategy towards assembling CPPs is by linking building blocks together through the formation of strong covalent bonds. The most widely employed methods utilise metal-mediated coupling reactions such as Suzuki-Miyuara coupling,[39,40,43,44] Sonogashira-Hagihara coupling,[39,45–48] Yamamoto coupling,[36,49–52] Glaser coupling,[81] and direct arylation (Fig. 1).[53–56] Other metal catalysed polymerisations include utilising cyclotrimerisation,[82,83] and Friedel-Craft type chemistry.[57–60] Within these reactions there exists an array of novel techniques that can be employed including mechanochemistry,[84] copper-free Sonogashira-Hagihara coupling variants,[85,86] utilising acetylene gas as a building block,[87] or using microwave heating.[52,88]

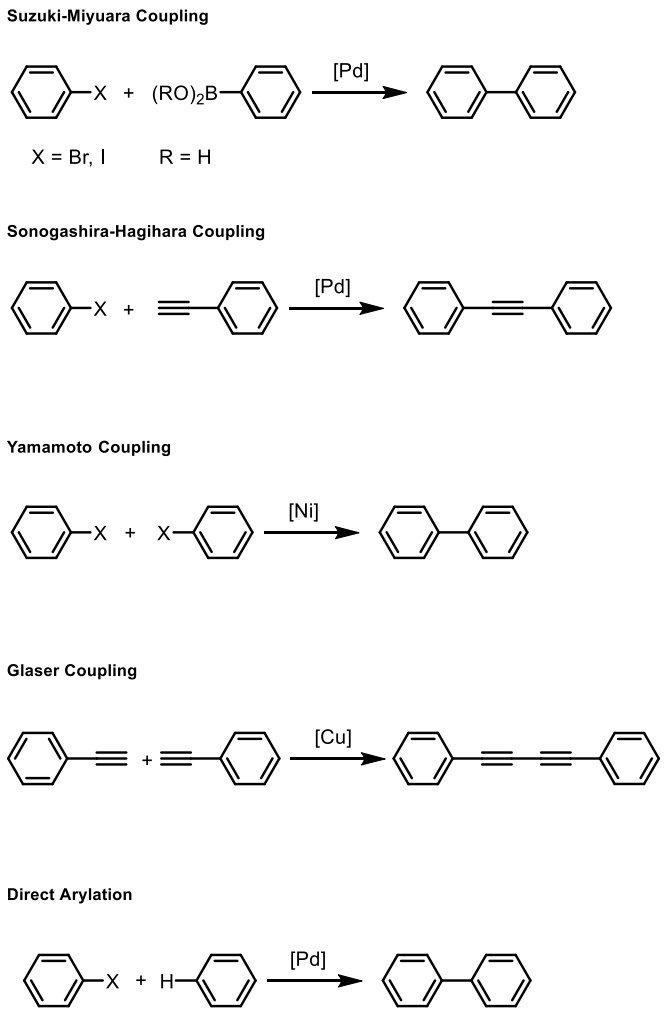

Fig. 1 Schematic representation of a selection of the common metal catalysed bond-forming processes used for CPP synthesis. The most commonly used methods are the Sonogashira-Hagihara followed by the Suzuki-Miyuara coupling reactions.

Although these metal-catalysed reactions are suitable for the polymerisation of a wide variety of building blocks, it is possible for residual metal catalyst to be trapped within the porous framework during synthesis. While some evidence has suggested that trace metals either have no effect or are not detrimental to applications including Stille coupling or hydrogen evolution, CPPs are often subjected to meticulous removal procedures such as Soxhlet's extraction in order to eliminate any remaining catalyst.[89,90]

An alternative approach to CPP synthesis is to entirely avoid the use of metal catalysts during the polymerisation step. This eliminates the problem of metals becoming trapped and thus trace levels are no longer problematic. There have been many reported examples of CPPs prepared by metal free polymerisations using reactions such as phenazine ring fusion (Fig. 2),[91] Schiff-base formation,[61–63,92] porphyrin formation,[77,93] dithiooxamide/formyl condensation,[94,95] cationic polymerisation,[96] Knoevenagel condensation (Fig. 3),[64,65] or Aldol condensation (Fig. 4).[97] Electropolymerisation techniques can also be utilised, yielding thin films of CPPs with controllable thicknesses mounted on electrodes.[66–69]

Due to their cross-linked nature, CPPs are usually obtained as powders that are insoluble in most common solvents, and they possess various morphologies including tubes, spheres, platelets *etc*. In addition to powders, CPPs can also be prepared in a variety of other physical forms. For example, one method involves performing polymerisation without stirring, which can lead to monolithic structures.[43] Thin films of CPP can be prepared either by electrochemical polymerisation, polymerisation of thin monomer films or by carrying out

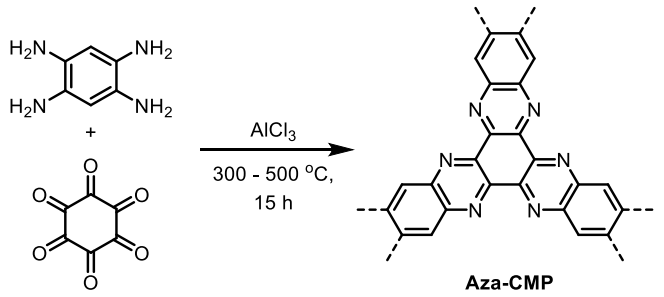

Fig. 2 Synthesis of **Aza-CMP** via phenazine ring fusion.[91]

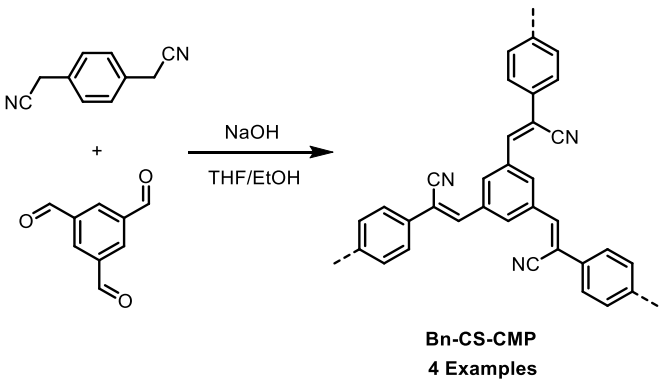

Fig. 3 Synthesis of porous organic polymers via the Knoevenagel condensation.[65]

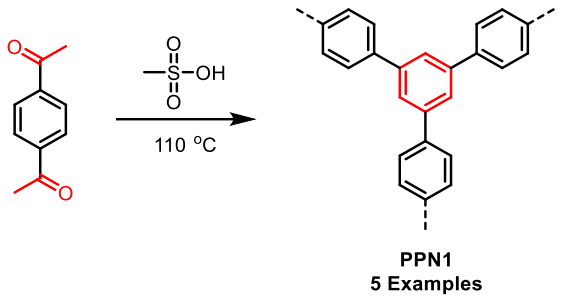

Fig. 4 Synthesis of porous organic polymers via a triple Aldol condensation.[97] The red highlights indicate the parts of the monomer/CPP involved with or formed by the Aldol condensation.

polymerisation at the interface between two immiscible phases.[68,98,99]

While their insolubility does simplify recovery and recycling of the material, it does severely limit processing. There are, however, reported examples of soluble CPPs. Pyrene based CPPs featuring *tert*-butyl groups that are soluble in common solvents such as tetrahydrofuran (THF), dichloromethane (DCM) and toluene have been studied by Cooper and coworkers. (Fig. 5).[100] Following synthesis the polymer could be obtained from solution by different methods including precipitation from an antisolvent (e.g. petroleum ether) and solution casting (e.g. from dichloromethane).

Chen *et al*. have reported on a method to prepare free-standing CMP nanofilms by performing Sonogashira-Hagihara coupling and Schiff base reactions at oil-water interfaces.[98] The organic phase in the former contained the conjugated monomers and $Pd(PPh_3)_2Cl_2$, whilst the aqueous phase contained triethylamine and copper (I) iodide, leading to reaction at the interface between the two phases to form a thin film. Since this film is insoluble in either of the two phases, monomers and catalysts are precluded from reacting, preventing the layer from increasing in thickness. The thickness of the film was observed to increase linearly with the monomer concentration from 30 to 186 nm. The latter reaction type followed a similar strategy, with the monomers dissolved in xylene and using acetic acid as the catalyst.

The synthetic methods mentioned above can all be used to introduce functionality into the CPP by utilising building blocks that feature the required functional groups. For example, Cooper and coworkers have demonstrated that Sonogashira-Hagihara cross coupling can be used to synthesise a range of CPPs, with the polymerisation technique tolerant to methyl, fluoro- and trifluoromethyl, hydroxy-, methoxy-, amino and pyridyl groups to name but a few.[101] An alternative approach to introducing functionality is to modify the CPP post synthesis. For example, thiol-yne chemistry can be used to modify acetylenic based CPPs (Fig. 6).[102] This leads to the introduction of thioalkyl groups that have been reported to improve the dispersibility of the CPP in water.[103] However, this process also leads to changes in the porosity and structural morphology due to the different connecting groups. Similarly, post synthetic amidation of the amine bearing **CMP-1-NH$_2$** has been reported to provide a route for the incorporation of chirality (Fig. 7).[104] Another simple method for modification is by the adsorption of functional species. For example, the distribution of palladium nanoparticles (which could be used for various applications) using supercritical CO_2 has been reported.[105]

1.1.3 Influencing the Porous Structure CPPs can be further classified by the size of their pores. Pores with a diameter less than 2 nm are classified as micropores according to the IUPAC definitions; thus CPPs with pores in this regime are referred to as conjugated microporous polymers (CMPs).[106] CPPs with pores in the region of 2 - 50 nm are termed mesoporous while pores larger than 50 nm are macroporous. In addition, materials can possess porous features from multiple different classifications, leading to hierarchical porosity. With CMPs, a pore size of ultramicroporous is occasionally specified: this refers to pores that have a diameter of less than 0.7 nm.[107]

Since the porous structure of CPPs is a major influence on its applications, much effort has been invested in establishing methods for controlling porosity and surface area. Early work established that the pore structure, surface areas and bulk density can be influenced by factors such as strut length (length of the bridging groups/cross-linkages),[51,108,109] monomer geometry,[49,110] and reactions conditions (solvent used,[111]

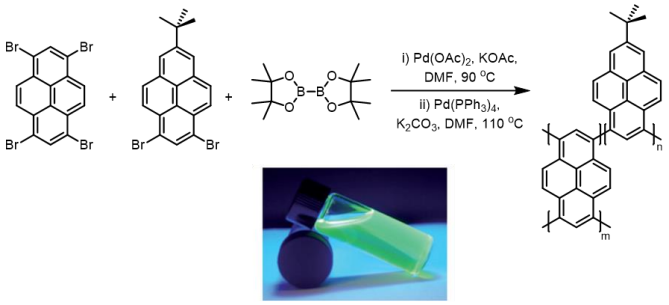

Fig. 5 Synthesis of soluble CMPs. Inset: A soluble CMP dissolved in THF. Adapted from Ref. 100 with permission of Wiley-VCH, copyright 2015.

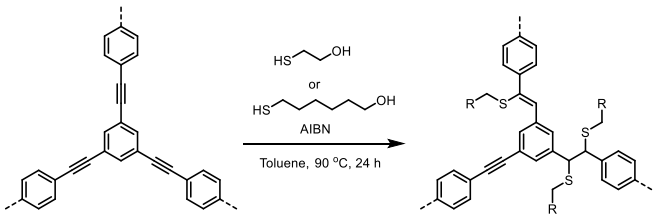

Fig. 6 Post synthetic modification of a CMP using thiol-yne chemistry. Modification by reaction with 1 or 2 equivalents of thiol are highlighted. AIBN = 2,2'-Azobis(2-methylpropionitrile).[102]

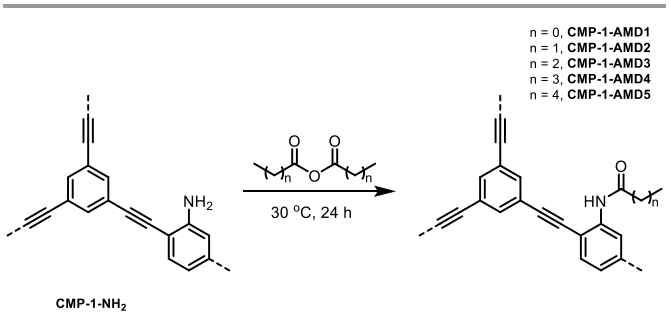

Fig. 7 Post-synthetic modification of **CMP-1-NH$_2$** using amidation reactions.[104]

catalyst used,[112] microwave heating, monomer feed ratios).[113] For an in-depth review of these effects and how they impact porosity, the reader is directed to an earlier review by Jiang and coworkers.[73]

The porosity characteristics of a CPP can also be fine-tuned via the use of templates during polymer synthesis. For example, CMPs based on the benzo[*c*][1,2,5]thiadiazole (BTZ) unit have been prepared via Sonogashira-Hagihara coupling utilising silica nanoparticles as templates (Fig. 8).[45] Formation of the network occurred around the nanoparticles, which were subsequently removed post synthesis via chemical etching with ammonium hydrogen difluoride (NH_4HF_2). Although these conditions are rather harsh, the overall structure of the CMPs were maintained. The use of the silica nanoparticles as templates led the Brunauer-Emmett-Teller (BET) surface area to increase from its initial value of 270 $m^2\ g^{-1}$ for the untemplated CPP up to 660 $m^2\ g^{-1}$ (when using 60 mg of silica per mL of reaction mixture). Nguyen and coworkers have also utilised a similar approach by carrying out CPP synthesis inside a mesoporous silica aerogel template that can be removed using hydrofluoric acid.[114]

A similar strategy has also been explored using an electrospun poly(vinylpyrrolidone) (PVP) membrane as a sacrificial template.[115] By performing Sonogashira-Hagihara coupling of 1,3,5-triethynylbenzene and 1,4-diiodobenzene in the presence of the electrospun PVP, a membrane (**PVP@CMP**) consisting of PVP nanofibres with an average diameter of 200 nm covered in a 50 nm thick shell of CMP was obtained. Removing the PVP fibres by extraction with solvent led to hollow, tubular fibres with an internal diameter of ca. 200 nm (Fig. 9).

CPPs containing benzo[*c*][1,2,5]thiadiazole and fluorene groups prepared by polymerisation of high internal phase emulsions (HIPEs) have demonstrated hierarchical porosity.[43,116,117] Formation of the CPP occurred around the droplets of the dispersed phase, which were then removed when the polymer was dried. This led to hierarchical porosity, with macropores derived from the templating effect and microporosity characteristic of the polymer network.

Lee *et al*. have demonstrated a unique strategy for tuning the pore structure, as well as the electronic properties, of CMPs assembled by Schiff-base chemistry by varying the strength of the acid catalyst (Fig. 10A).[118] Regardless of the strength of the acid catalyst, Schiff-base chemistry between triphenylene-1,5,9-triamine and terephthaldehyde was first used to form the uncyclised CMPs, **ucCMP**. These exhibited a low surface area, which was attributed to the tilted geometry of the uncyclised structure that obstructed the pores. Treatment of the **ucCMP** with strong acids (trifluoroacetic, *p*-toluenesulfonic, hydrochloric and triflic acids) led to varying extents of *in situ* cyclisation and the formation of cyclised CMPs, **cCMP**. The BET surface area was observed to increase linearly with the pKa of the acid catalyst, such that triflic acid yielded the largest surface area of 806 $m^2\ g^{-1}$ due to the greatest degree of cyclisation (Fig. 10B). Significant deviation from this linear trend can be observed when using acetic acid as the catalyst. While acetic acid was able to catalyst the imine formation, in comparison to the other, much stronger acid catalysts, it was unable to produce high degrees of cyclisation and led to a low BET surface area (3.7 $m^2\ g^{-1}$).

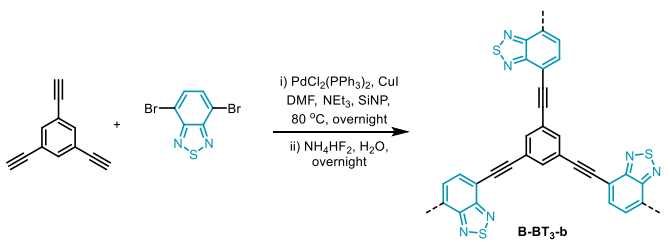

Fig. 8 Templated synthesis of BTZ containing CMPs.[45] SiNP = silica nanoparticles. BTZ groups are highlighted in blue.

1.1.4 Characterisation of CPPs Whilst arguably beneficial in certain applications, the insolubility of CPPs limits characterisation of CPPs to solid-state techniques. Given that the function and application of this class of materials are closely linked not only with its chemical composition, but also its morphology and pore structure, thorough characterisation of CPPs is essential. In this section, we will highlight some of the most important characterisation techniques for CPPs in general and what information can be gained from such analysis. Although the techniques mentioned here provide in-depth information on the structure and composition of CPPs, this is by

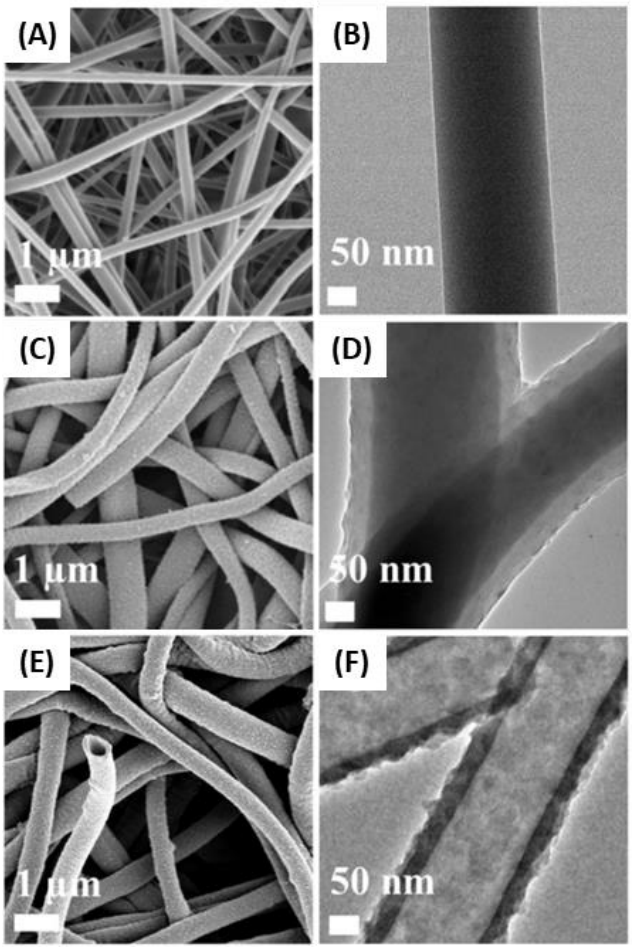

Fig. 9 SEM (left) and TEM (right) images of (A, B) electrospun PVP membrane, (C, D) **PVP@CMP** (C,D), and (E, F) the CMP membrane. Adapted from 115 with permission from Springer Nature, copyright 2017. Available under CC-BY-4.0.

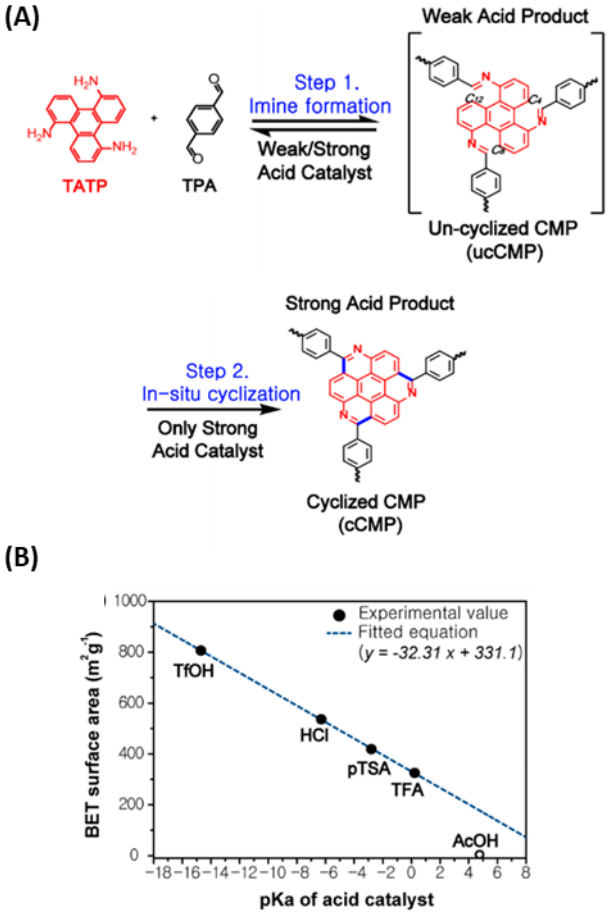

Fig. 10 (A) Synthesis of CMPs by Schiff-base chemistry followed by *in situ* cyclisation in the presence of strong acid catalysts. (B) Plot of BET surface area against the pKa of the acid catalyst. Adapted with permission from Ref. 118. Copyright (2018) American Chemical Society.

no means an exhaustive list. For example, for photocatalytic applications, solid state or suspension UV-Vis absorption spectroscopy provides information about what wavelengths of light the material will absorb and subsequently what light is most useful. Similarly, performing electrochemical measurements on CPPs, namely cyclic voltammetry, can provide information about the materials redox potential, thus allowing it to be matched to the redox potential of substrates for photocatalysis. Other such specific techniques include contact angle measurements, fluorescence spectroscopy *etc.*

1.1.4.1 Composition and Structural Characterisation The chemical composition of CPPs is primarily analysed via the use of CHN analysis. CHN analysis is a technique that is often also applied to small molecules to establish their empirical formula by monitoring the products of carbon, hydrogen and nitrogen combustion. Performing this technique on CPPs will provide information about the composition of the bulk material but will only elucidate information about a materials carbon, hydrogen and nitrogen content. Analysers which can determine a materials sulfur and oxygen content are also available, but these have not been widely utilised for analysis of CPPs. With CHN analysis, deviation from the expected chemical composition is expected as the repeat unit selected for CPPs is idealised and is not completely reflective of the material's true composition. For example, unreacted functional groups could remain, trapped by the growing pores and precluded from reaction, or on the surface of the CPP. One drawback of using CHN analysis is that incomplete combustion can give an inaccurate reading of the composition.

Characterisation of the bulk material via CHN analysis can be complemented by techniques to detect trace contaminants such as residual metal catalyst remaining from synthesis or materials consisting of elements other than C, H, N, O or S.[5] This is commonly done via energy dispersive x-ray (EDX) spectroscopy or techniques such as inductively coupled plasma-optical emission spectroscopy (ICP-OES), ICP-atomic emission spectroscopy (ICP-AES) or ICP mass spectrometry (ICP-MS).

Infrared (IR) spectroscopy is a simple yet powerful technique that can be used to determine the functional groups present in CPPs and can be used to identify unreacted polymerizable groups or to monitor the progress of post-synthetic modifications. Similar information can also be obtained from solid-state NMR spectroscopy. The signals observed by solid-state NMR spectra are very broad due to the existence of anisotropic interactions and dipolar couplings. This can be compared to solution state NMR, where the interactions are averaged by Brownian motion, leading to sharp signals. These interactions can be somewhat mitigated by spinning the sample at an angle of 54.74° with respect to the magnetic field direction (called the magic angle).[119,120] Solid state cross-polarisation magic angle spinning (SS CP/MAS) ^{13}C NMR is commonly applied to CPPs to determine the structure of the repeat unit by providing information on the environment carbon atoms are located or to identify carbon-based contaminants.[5] To date, there has, to the best of our knowledge, been no reported analyse of CPPs using any solid state ^{1}H NMR techniques: this is most likely due to the significant line-broadening effects arising from strong ^{1}H-^{1}H dipolar couplings.[121,122]

1.1.4.2 Surface Area Characterisation Given that the porous structures of CPPs is one of their defining features and is often related to the materials properties, thorough investigation of the surface area and pore structure are highly important to allow for comparison between different polymers. The technique that is utilised for this is gas adsorption: a process that measures the increase in the concentration of gas molecules adsorbed onto the surface of samples. An important step during this process is outgassing, which involves heating the material under vacuum to remove residual adsorbates. It is therefore recommended to perform thermal gravimetric analysis (TGA) prior to carrying out gas adsorption in order to assess if the CPP is chemically or structurally altered by periods of sustained heating. Various adsorptives can be utilised for gas adsorption including N_2, CO_2, Ar, He, CH_4 *etc.*, although the most common and standard method for the analysis of micro- and mesopores is using N_2 at 77 K.[123] However, various studies have demonstrated that the use of N_2 under cryogenic temperatures kinetically restricts its access to ultramicropores.[124–126] An alternative approach is to use CO_2 at 273 K. Due to the higher

temperatures and pressures used, diffusion of CO_2 is much faster and pores as small as 0.4 nm can be analysed. However, it should be noted that CO_2 at 273 K can only be used to probe pores smaller than 1 nm.

According to IUPAC recommendations, six general adsorption/desorption isotherms can be identified, with characteristic forms that are indicative of the porous features of the material (Fig. 11).[123] For CPPs, the most important isotherms are type I and type IV. Type I isotherms are characteristically concave to the p/p^o axis and approach a limiting adsorption value governed not by the internal surface area but instead by the accessible micropore volume. At low values of p/p^o, type I isotherms exhibit a steep gradient, arising from increased adsorbent-adsorptive interactions in the narrow micropores. Type I isotherms can be further separated into type I(a) and type I(b): the former is characteristic of microporous materials with narrow micropores (<1 nm) while the latter is observed with materials with wider micropores or narrow mesopores (< 2.5 nm). Type IV isotherms are characteristic of mesoporous materials and, like type I isotherm, can be separated into type IVa and type IVb. The particular classification of an isotherm as type IVa or IVb is dependent on the width and shape of the mesopores.[127] Gas adsorption/desorption isotherms can also exhibit hysteresis loops arising from differences in the adsorption and desorption processes. The form that these hysteresis loops take can provide additional information about the shape/size of pores and for more information on this, and gas adsorption experiments in general, we can direct the reader to a review by Cychosz *et al*. [127] The units of pressure used in gas adsorption isotherms are relative pressure, which is derived from the equilibrium pressure divided by the vapour pressure. The reason pressure is expressed in this way is that this eliminates the variation in pressure from small temperature changes (these can drastically change the vapour pressure).

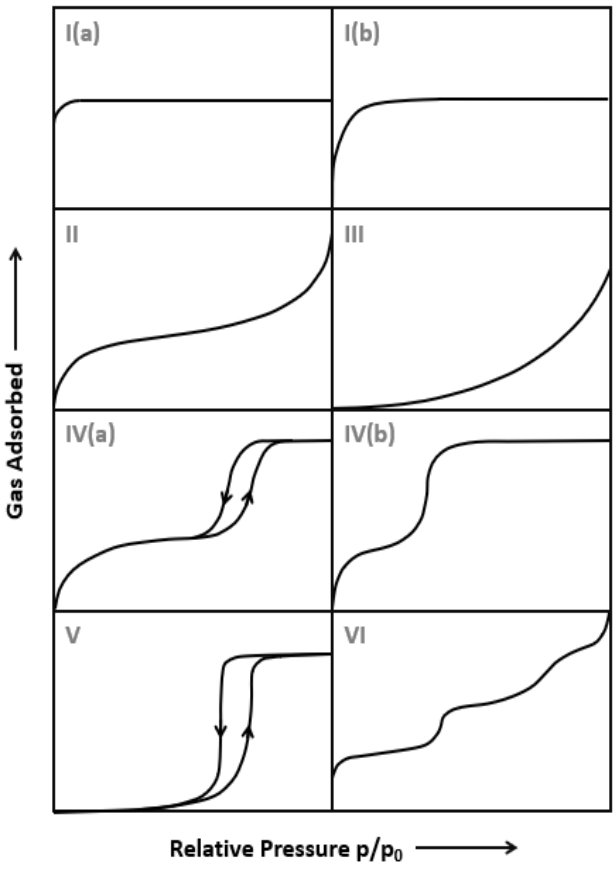

Fig. 11 IUPAC recommended classification of physisorption isotherms. Hysteresis loops illustrated for type IV(a) and type V isotherms.[123]

Evaluation of the physisorption isotherms can provide information about the specific surface area of the porous sample. There are many different models which can be applied to interpret the physisorption but the most commonly used method for CPPs is the Brunauer-Emmett-Teller (BET) theory.[128] This model, first proposed in the 1930s, extends the Langmuir monolayer model to multilayer adsorption.[129–131] There are two stages to application of BET theory: first conversion of the physisorption isotherm into a BET plot from which the monolayer capacity and BET surface area (SA_{BET}) can be obtained. For more information on the applicability and limitations of this model, we can direct the reader to the IUPAC guidelines for gas adsorption in porous materials.[123]

In addition to the specific surface area, gas adsorption experiments can also provide information about pore size distribution. This is an important property to understand since it is the basis for classifying what specific type of porosity is present in CPPs i.e. micro-, meso- and/or macroporosity, in accordance with IUPACs recommendations. Various methods can be used and are widely based on density functional theory (DFT). These methods are capable of describing the adsorbed phase accurately at the molecular level and can be used to calculate an accurate pore size distribution over both the micro- and mesoporous regimes. In comparison, macroscopic thermodynamic models can often underestimate pore size as they cannot accurately describe fluid confined within the pore.[123,132] Improvements to DFT have been made using non-local density functional theory (NLDFT), which allows accurate information to be obtained using the hysteresis loops of isotherms. Through these DFT methods, adsorption isotherms are predicted for individual pore size. The theoretic series of isotherms, referred to as the kernel, can be used to derive a pore size distribution function by comparison to the experimental adsorption isotherm.

1.1.4.2 Morphology Characterisation Investigation of CPP morphology is most often carried out using electron microscopy techniques, namely scanning electron microscopy (SEM) and transmission electron microscopy (TEM). Both techniques utilise beams of high-energy electrons to construct nanoscale images of samples and can be used to identify the morphology of CPPs, which have been reported to feature morphologies such as tubes, spheres, platelets, rods and rings (Fig. 12). These are features that cannot be observed using optical microscopy, which at best can provide a resolution of ca. 1 μm. By comparison, SEM and TEM can offer resolutions of up to 1 nm and 0.1 nm respectively.

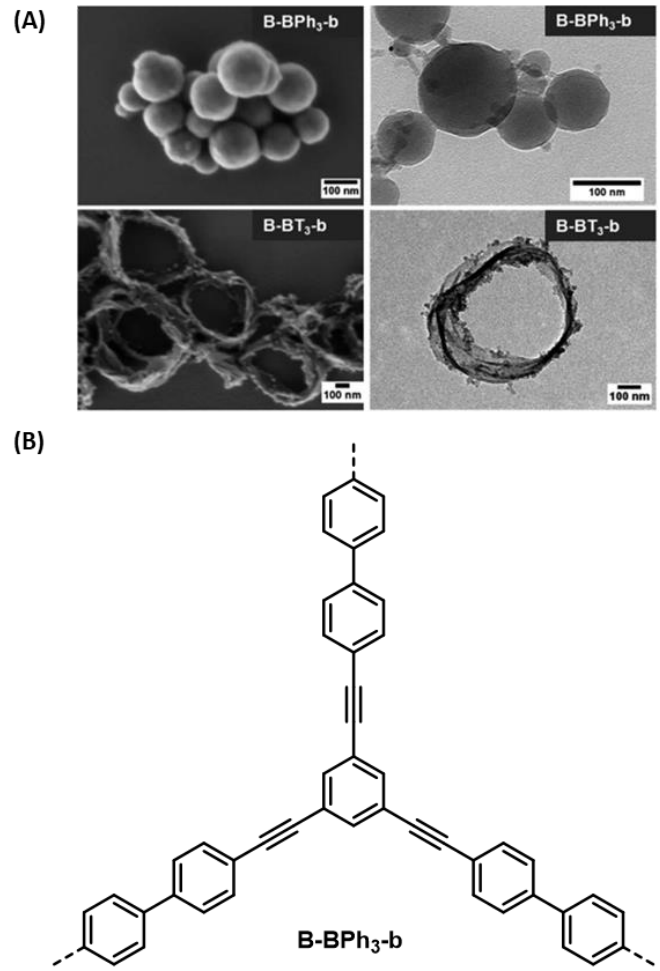

Fig. 12 (A) Examples of SEM (left) and TEM (right) images of CPPs possessing spherical (top) and ring (bottom) morphologies. (B) Structure of **B-BPh$_3$-b**. The structure of **B-BT$_3$-b** is shown in Fig. 8. Adapted from Ref. 39 with permission from the Royal Society of Chemistry, copyright 2015.

2 CPPs as Versatile Catalysts

2.1 CPPs as Photocatalysts

The extensive π-conjugation present in CPPs allows them to harvest light and use this captured energy to drive chemical reactions.[23] In particular, the extended π-systems present in CPPs results in low band gap character that is suited to the absorption of mainly visible light and by careful consideration of the photophysical properties of the building blocks, it is possible to engineer efficient CPP photocatalysts.[133] One approach is to select building blocks consisting of both strong electron acceptor and weak electron donors.[43] This mismatch in the acceptor-donor strength combination slows down recombination of hole-electron pairs and facilitates intersystem crossing. Another option could to take advantage of El-Sayed's rule, where the rate of ISC from the singlet state to the triplet manifold is large if the process is accompanied by a change in orbital character.[134,135] This phenomenon has been observed in various heterocycles including *N*-heterocyclic aromatics (such as carbazoles) and carbonyl compounds.[136] One could also take advantage of the heavy atom effect: heavy atoms such as halogens (bromine, iodine) or transition metals (Pt, Ir, Ru) result in increased spin-orbit coupling which facilitates ISC.[137,138] However, the use of the heavy atom effect in relation to the photophysical properties of CPPs has not received that much attention. With the case of halogen atoms, this could be because these are often consumed in transition-metal catalysed synthetic procedures. Further structural levers that can be tuned to control the photophysical and photochemical properties of CPPs include varying the ratio of strong electron acceptor to weak electron donors,[43] introducing strained rings,[139] and altering the length of the bridging units.[140]

2.1.1 Singlet Oxygen Generation In its ground state molecular oxygen possesses triplet spin multiplicity, which prohibits it from reacting with most organic species, which usually occupy the singlet state. By contrast, its low lying first excited singlet state is far more reactive and has potential applications in chemical synthesis, biological decontamination and photodynamic therapy.[141,142] However, direct excitation from the ground state to these states is forbidden by the laws of spin conservation. Many methods can be used to generate singlet oxygen but the simplest and most commonly employed method in laboratory research is photosensitisation (Fig. 13). This method requires light, molecular oxygen and a photosensitiser with a triplet state of energy at least 95 kJ mol^{-1} relative to the ground state.[143] Upon absorbing a photon of light of sufficient energy, the photosensitiser will be electronically excited first to the singlet state. From this state, energy can be lost via fluorescence or via intersystem crossing to the triplet state. The photosensitiser can then either relax via phosphorescence or transfer its energy to the ground state

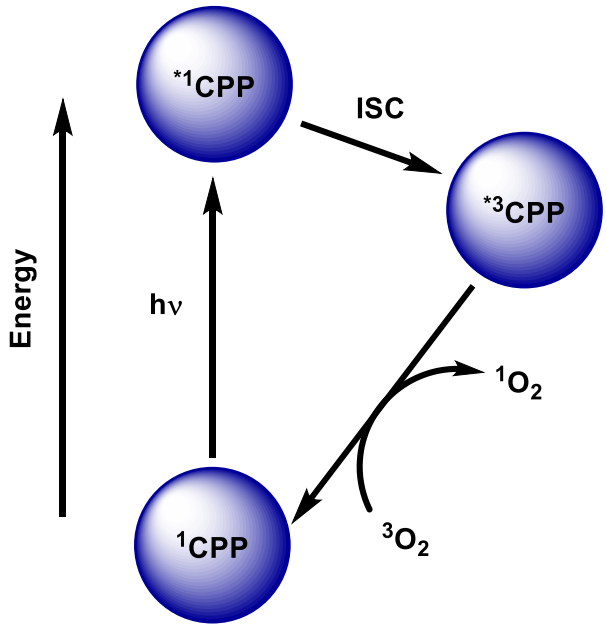

Fig. 13 Simplified schematic representation of the generation of singlet oxygen using a CPP photosensitiser. Excitation of ^{1}CPP, the ground state photosensitiser, will yield ^{*1}CPP that will undergo intersystem crossing (ISC) to the triplet state, ^{*3}CPP. Triplet-triplet annihilation with $^3O_2$ will yield $^1O_2$.

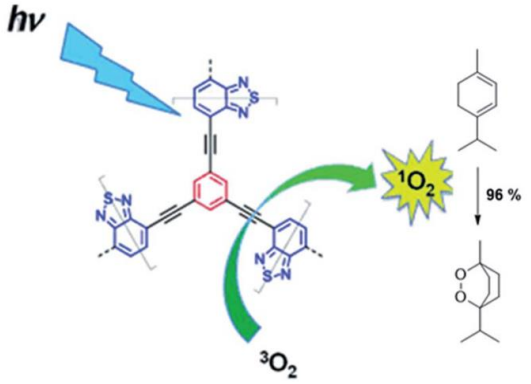

Fig. 14 Generation of singlet oxygen using BTZ containing CMPs and the conversion of α-terpinene into ascaridole. Reproduced from Ref. 45 with permission of Wiley-VCH, copyright 2013.

oxygen, simultaneously exciting oxygen to the first excited state and regenerating the ground state photosensitiser.

One common application of CPPs is in the generation of singlet oxygen. For example, CPPs based on the BTZ moiety have been used to generate singlet oxygen under 420 nm light.[45] In order to monitor the generation of singlet oxygen, the conversion of α-terpinene into ascaridole, an example of [4+2] cycloaddition, was selected as the benchmark reaction (Fig. 14). Under both batch and flow conditions, ascaridole was obtained thus suggesting the generation of singlet oxygen. Using silica nanoparticles (diameter approximately 12 nm) as templates, the surface area of the CPPs could be tuned and this was reflected in their photocatalytic activity. Later work on these polymers would address the hydrophobicity of these polymer networks by introducing mercaptopropionic acid groups via a post-synthetic thiol-yne reaction.[103] These hydrophilic groups enhanced the singlet oxygen generation in water by improving the dispersability of the material in the reaction solvent.

Boron-dipyrromethene (BODIPY) based CMPs prepared by Tobin *et al*. using two different routes have also demonstrated efficient singlet oxygen generation (Fig. 15).[40] The first of these, **BDP_CMP**, involved assembly of building blocks via Suzuki-Miyuara polycondensation, resulting in the BODIPY group being incorporated into the polymer skeleton. Synthesis of the other CMP, **PHTT_BDP**, involved post-synthetic modification of an aldehyde bearing CMP using a typical BODIPY synthesis procedure.[144] When applied to the conversion of α-terpinene into ascaridole (530 nm light), both CMPs displayed high conversions (81 to >99%). However, repeated use of **PHTT_BDP** led to a 10% loss in photoactivity, with the greater photostability of **BDP_CMP** attributed to the inclusion of the photoactive unit within the framework backbone of the material.

Metallophthalocyanine-based CMPs containing complexed Co(II), Ni(II), Cu(II) and Zn(II) ions have also been demonstrated to generate singlet oxygen.[62] These polymers were prepared by Schiff-base formation under solvothermal conditions (Fig. 16). The singlet oxygen generating abilities of these polymers were studied at 700 nm using the oxidation of 1,3-diphenylbenzofuran (DPBF), as the progress of the reaction can

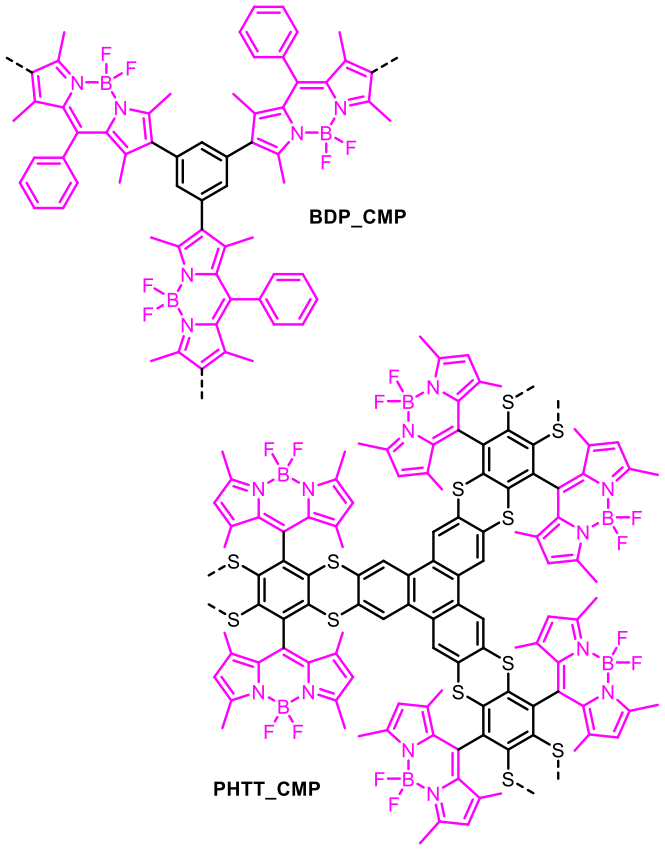

Fig. 15 Structure of BODIPY based CMPs. **BDP_CMP** was prepared by Suzuki-Miyuara cross coupling while **PHTT_BDP** was prepared using a typical BODIPY synthesis from an aldehyde-bearing CMP precursor.[144] BODIPY-groups are highlighted in pink.

be followed by UV-vis spectroscopy; this is achieved by tracking the decrease in absorption at 410 nm as DPBF is consumed. The nature of the metal centre was found to play a role in influencing the photoactivity of the material, with metal ions featuring open shell electron configurations exhibiting weaker photoactivity. Consequently, the Zn(II) metallophthalocyanine CMP with its full *d*-electron configuration displayed the highest photoactivity. Later work by the same authors would expand upon the scope of building blocks usable by studying copper phthalocyanine-based CMPs.[61]

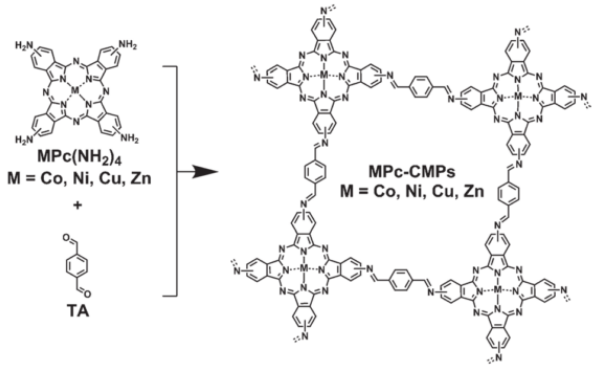

Fig. 16 Synthesis of metallophthalocyanine based CMPs via Schiff-base chemistry. Reaction conditions: Dimethylacetamide (DMA). Reproduced from Ref. 62 with permission from Wiley-VCH, copyright 2013.

2.1.2 Photooxidation One application of reactive oxygen species (ROS) generated from CPPs is for the oxidation of organic substrates. For example, there have been several reports demonstrating the oxidation of organic sulfides, which can serve as a model compound for the chemical warfare agent sulfur mustard. CPPs featuring *tert*-butyl carbonate (Boc) groups have been applied to the photocatalytic oxidation of thioanisole.[116] These polymers were prepared by HIPE polymerisation with the Boc groups acting as spacers that could be removed post synthesis under vacuum (Fig. 17). Under conditions of 460 nm light and using air as the oxygen source, the Boc-protected and deprotected polymers demonstrated moderate to high conversions (33-99%) and selectivity for the sulfoxide (95 - >99%).

Liras *et al*. have also demonstrated the oxidation of thioanisole by singlet oxygen using a BODIPY-based CMP (Fig. 18).[46] Using 0.1 mol% of the CPP, a conversion of 99% and a turnover of 990 within 24 hr could be obtained (150 W quartz-halogen lamp with 500 nm cut-off filter). It should be noted that more efficient oxidation of thioanisole was achieved when using the CMP as a photocatalyst instead of soluble monomeric analogues under equivalent conditions (24–44% conversion).

Su *et al*. have also demonstrated photooxidation of sulfides using a carbazole based CMP, **C-CMP** (Fig. 19A).[145] Using visible light, the authors were able to achieve high yields for oxidising a range of sulfides (>90%), with high selectivity for the sulfoxide over the sulfone (Fig. 19B). In addition, Su *et al.* also demonstrated catalytic photooxidation of various amines. With primary amines, this resulted in homocoupling to form imines (Fig. 19C, photooxidative coupling is discussed in more detail in section 2.1.4). With secondary amines, including nitrogen containing heterocycles, photooxidation using the carbazolic CMP resulted in dehydrogenation in reasonable yields (61 – 76%) (Fig. 19D).

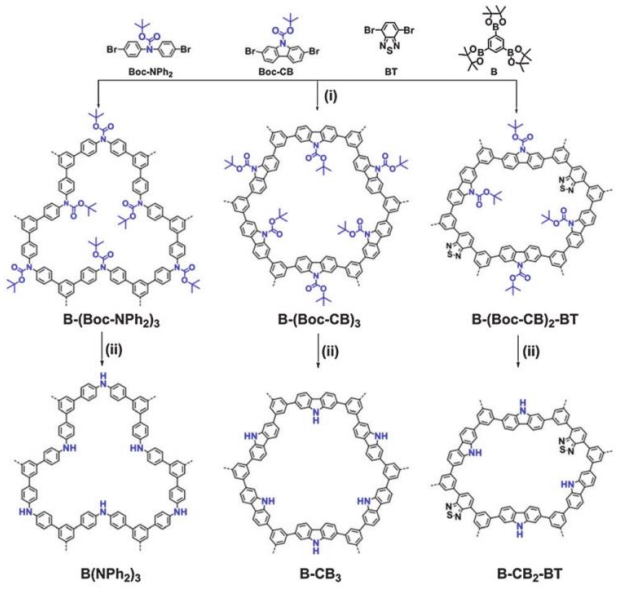

Fig. 17 Synthesis of Boc-containing and Boc-removed conjugated porous polyHIPEs. Following synthesis, the Boc groups could be removed under vacuum. Reaction conditions i) $Pd(PPh_3)_4$, Span80, toluene:H_2O (1:9), 80 °C, overnight. (ii) 250 °C, vacuum, 12 h. Reproduced from Ref. 116 with permission from the Royal Society of Chemistry, copyright 2014.

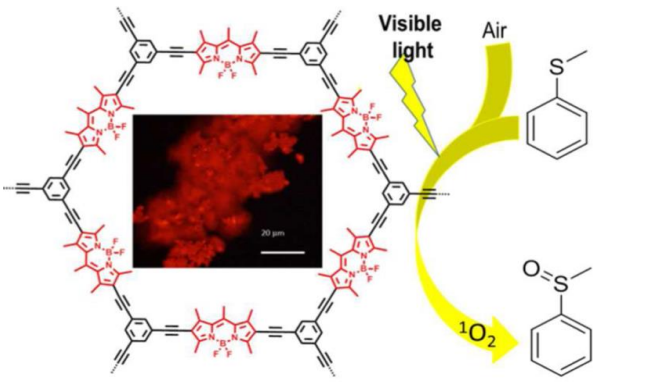

Fig. 18 BODIPY-based CMP for the photocatalytic oxidation of thioanisole using singlet oxygen. Image is a fluorescence microscope image of the CMP. Reprinted with permission from Ref. 46. Copyright (2016) American Chemical Society.

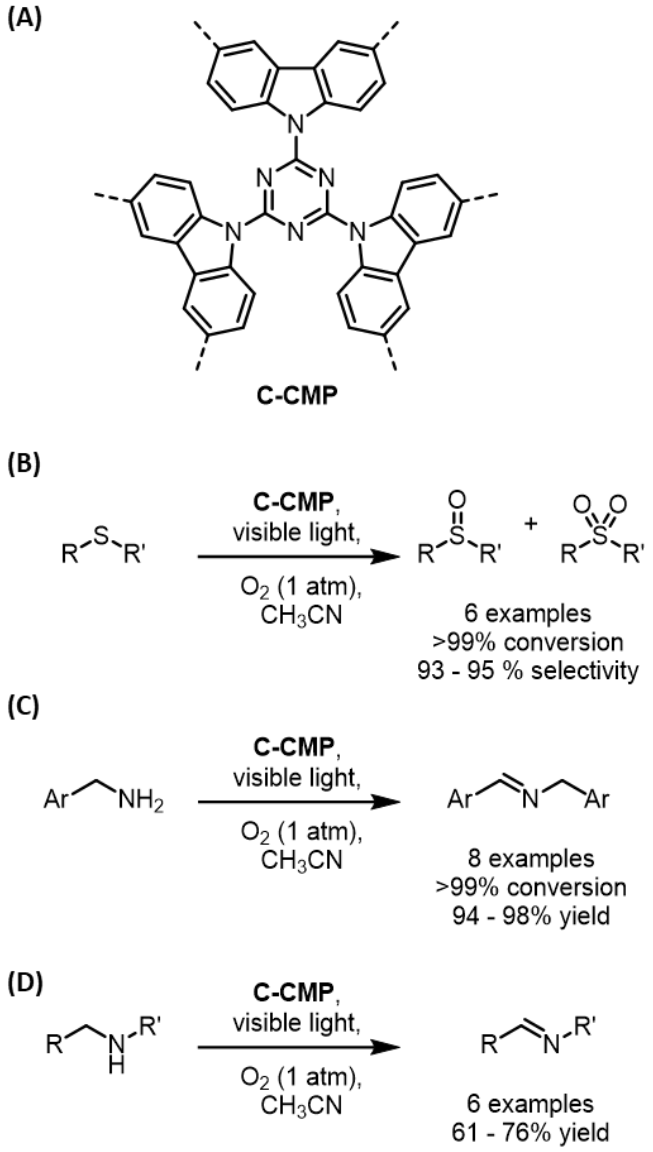

Fig. 19 (A) Structure of carbazoles based CMP **C-CMP** and reaction schemes for (B) photochemical homocoupling of primary amines, (C) dehydrogenation of secondary amines and (D) oxidation of sulfides primary to the corresponding sulfoxide [145]

Zhang and coworkers have demonstrated the selective oxidation of aldehydes and ketones utilising a thiophene based covalent triazine framework utilising molecular oxygen as the oxidant.[146] **CTF-Th@SBA-15** was prepared on a mesoporous silica support coated with the dicyanothiophene (DCT) monomer by cyclotrimerisation of its cyano- groups (Fig. 20), resulting in a BET surface area of 548 $m^2 g^{-1}$. Based on the pore size of the unadulterated mesoporous silica (5.7 nm) and the pore size of the CPP on silica (3.8 nm), the thickness of the CPP layer was inferred as ca. 1.9 nm. Utilising visible light (460 nm, 4 hours), high conversions (>78%) of various aromatic aldehydes with high selectivity (72 - >99%) could be obtained. The mesoporosity induced by utilising the silica was observed to influence the reaction, as its removal led to a reduction in conversion to 17%. This was attributed to a collapse in the pore structure leading to a decrease in surface area (from 548 $m^2 g^{-1}$ to 57 $m^2 g^{-1}$). Mechanistic investigations were performed to investigate the active ROS in the reaction. The addition of scavengers for photogenerated holes ($CuCl_2$ and benzoquinones), photogenerated electrons (ammonium oxalate) and $^1O_2$ (NaN_3) resulted in a decrease in the conversion of benzyl alcohol to benzaldehyde using **CTF-Th@SBA-15** while scavengers for the hydroxyl radical (*tert*-butyl alcohol) had little effect on the conversion. In combination with detection via spin trap electron paramagnetic resonance (EPR) spectroscopy of $O_2^{-\bullet}$ (trapped with 5,5-dimethyl-1-pyrroline N-oxide) and $^1O_2$ (with 2,2,6,6-tetramethylpiperidine), demonstrates that these are the two ROS involved in the oxidation and the hydroxyl radical is not.

Further work by Zhang and coworkers have also demonstrated the use of thiophene and BTZ-based CMPs for the photocatalytic cleavage of C=C bonds to form aldehydes, utilising reactive oxygen species as the source of the carbonyl oxygen (Fig. 21A).[147] The mechanism for the reaction involves excitation of CMP photocatalyst using visible light, leading to charge separated states. The photogenerated hole in the CMP highest occupied molecular orbital then oxidises the alkene to form the radical cation, which is trapped by the superoxide radical anion or singlet oxygen. This generates an oxetane which yields the 1,2-diol upon reaction with water and subsequently the aldehyde upon C-C bond cleavage (Fig. 21B).

2.1.3 Photochemical Degradation of Pollutants In addition to adsorptive mechanisms to remove pollutants, which are discussed later in this review, the extended π-system present in CPPs allows for photocatalytic degradation routes via generation of ROS such as $^1O_2$ or the superoxide radical anion, $O_2\bullet$-. For example, conjugated microporous polymer nanoparticles based on BTZ were found to be capable of photodegrading the dye rhodamine B in solution under air using visible light (23 W household lightbulb).[39] The polymers were prepared using either Sonogashira-Hagihara or Suzuki-Miyuara coupling, resulting in shapes such as spheres, rods and rings. In this case it was determined that degradation was principally due to singlet oxygen ($^1O_2$), although other ROS were also observed. Further examples of rhodamine B photodegradation by CPPs have also been reported by Duan and coworkers.[148–150] Similarly, CPPs have also been applied to the degradation of the dyes Congo red,[151] methyl orange,[152] and methylene blue[153]

It is also possible to combine both adsorptive and photochemical methods for the removal of contaminants. CPPs exhibiting this behaviour constructed from 9,9'-bifluorenylidene via Suzuki-Miyuara coupling have been reported by Wang *et al.*[154] These materials demonstrated dye adsorption capacities as high as 99% of the initial concentration or 1905 mg g^{-1}, with no observable decrease in efficiency over 10 cycles. Furthermore, these materials were also capable of achieving photochemical degradations as high as 92% using visible light (λ > 450 nm). The authors performed mechanistic

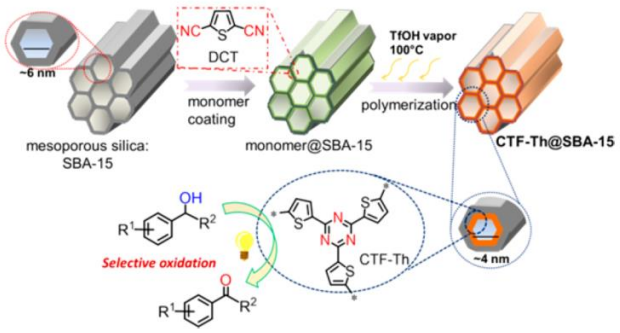

Fig. 20 Preparation of thiophene based CTF on mesoporous silica. Reprinted with permission from Ref. 146. Copyright (2017) American Chemical Society.

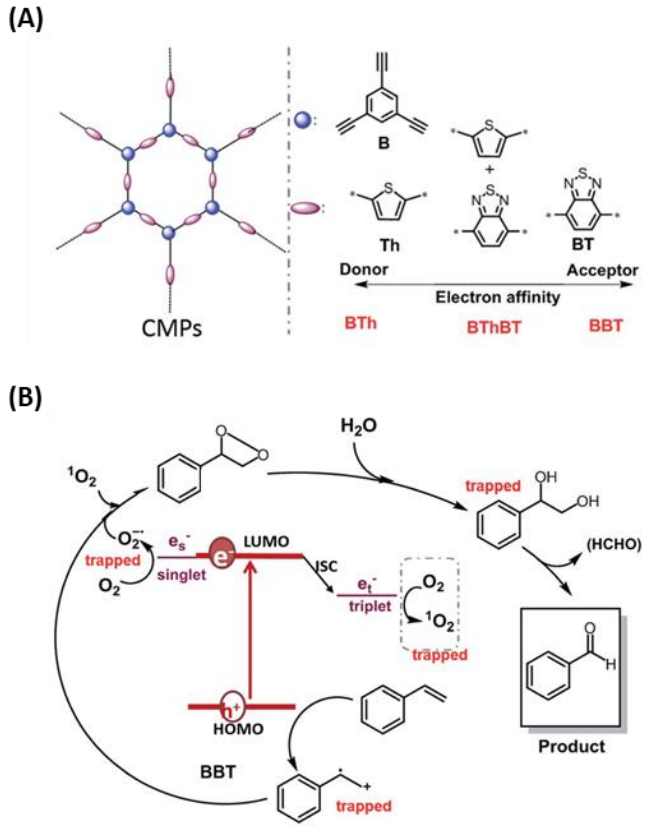

Fig. 21 (A) Structures of a series of thiophene and BTZ-based CMPs. (B) Proposed mechanism for the aerobic cleavage of C=C double bonds using CMP photocatalyst. Reproduced from Ref. 147 with permission from the Royal Society of Chemistry, copyright 2018.

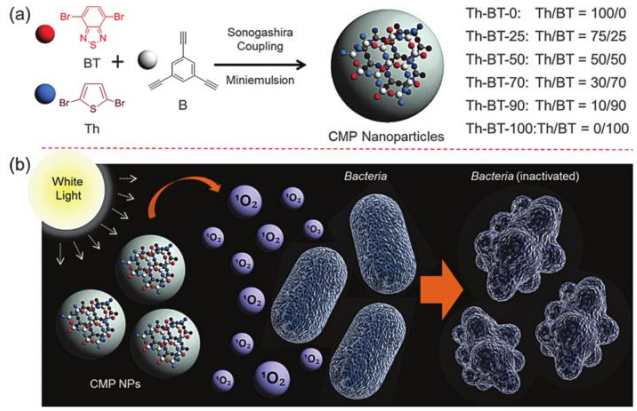

Fig. 22 (A) Structures and synthetic scheme for the CMP nanoparticles. (B) Application of the CMP nanoparticles to the inactivation of bacteria using *in situ* generated singlet oxygen. Reproduced from Ref. 155 with permission from the Royal Society of Chemistry, copyright 2016.

studies by using sodium azide, benzoquinone, isopropanol or ammonium oxalate as ROS scavengers (for $^1O_2$, the superoxide ion, the hydroxyl radical and photogenerated hole respectively). The only prominent decrease in activity was observed using benzoquinone, demonstrating the superoxide ion generated was the responsible ROS.

Photodegradation using CMPs can be expanded to include biological species, in addition to organic contaminants. Photoinactivation of the bacteria *E. coli K-12 and B. subtilis* by CMPs has been demonstrated by Ma *et al*., with singlet oxygen identified as the main species responsible.[155] By successively doping electron-withdrawing BTZ groups into a CMP based on the electron-donating thiophene group (Fig. 22A), greater performance for inactivation of bacteria was observed (Fig. 22B).

Ghasimi *et al*. have reported on the photoreduction of Cr(VI) to Cr(III) catalysed by conjugated microporous poly(azulene) networks as a means for treating water contaminated with heavy metals.[156] The CMPs initially obtained by Sonogashira-Hagihara cross coupling, **P-Az-1** and **P-Az-2**, were hydrophobic (Fig. 23A). Treating these materials with trifluoroacetic acid (TFA) protonates the electron-rich cyclopentadienyl ring to form the tropylium cation in **P-Az-1h** and **P-Az-2h**, which makes the CMPs hydrophilic and improves their dispersibility in water (Fig. 23B). Under visible light (23 W household lightbulb), both **P-Az-1h** and **P-Az-2h** were able to reduce the highly toxic Cr(VI) ions (from $K_2Cr_2O_7$) to the less toxic Cr(III) in quantitative conversions within 60 minutes. This result was achieved without the use of a sacrificial electron donor, although the authors also demonstrated that by adding excess formic acid as a sacrificial electron donor led to near-quantitative conversion within 30 minutes. In addition, the authors also describe the use of Fe(III) or Cu(II) ions as co-catalysts. These have reduction potentials below that of Cr(VI) and therefore facilitate reduction of Cr(VI) via the formation of a cascade cycle.

Xiang *et* al. have reported on a series of CMPs based on the dibenzo[b,d]thiophene-5,5-dioxide moiety (Fig. 24), and their subsequent application in the photochemical degradation of nitrogen monoxide gas (NO) by oxidation to the nitrate anion (NO_3^-).[157] Using visible light, 40 – 56% removal of NO was observed within 30 minutes of irradiation. The authors propose that the main active species in this reaction was the superoxide radical with both singlet oxygen and photogenerated holes also playing a role.

2.1.4 Photochemical Coupling Reactions One common photocatalytic applications of CPPs is in coupling reactions to form new chemical bonds between two species. Oxidative coupling of benzylamines to form imines has been demonstrated using CPPs as photocatalysts. For example, such conversion has been achieved using CPPs based on benzodifuran where these groups were formed via *in situ* intramolecular cyclisation during polymerisation (Fig. 25).[158] Upon irradiation with visible light (blue LED, λ_{max} = 460 nm), the polymer was able to achieve conversions as high as 98% under an oxygen atmosphere.

The homocoupling of amines using sunlight has been reported using a truxene based CMP, **Tx-CMP** (Fig. 26).[159] The

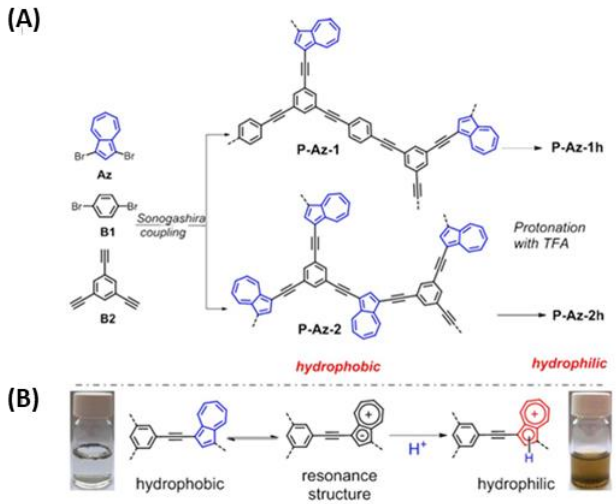

Fig. 23 (A) Synthetic scheme to **P-Az-1h** and **P-Az-2h**. (B) Illustration of the changes in hydrophobicity of azulene based CMPs upon protonating the cyclopentadiene ring. Reproduced from Ref. 156. with permission from Wiley-VCH, copyright 2016.

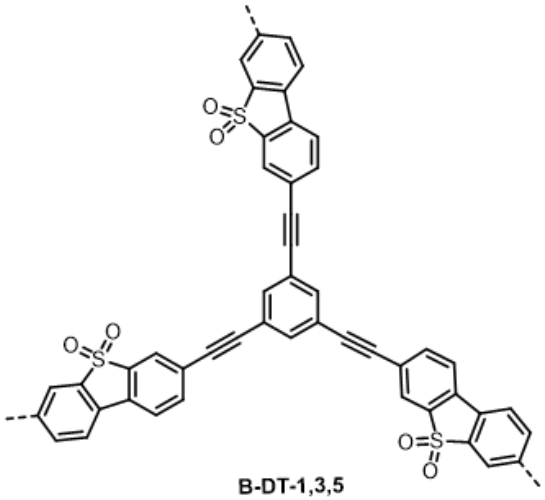

Fig. 24 Structure of dibenzo[b,d]thiophene-5,5-dioxide based CMP **B-DT-1,3,5.**[157]

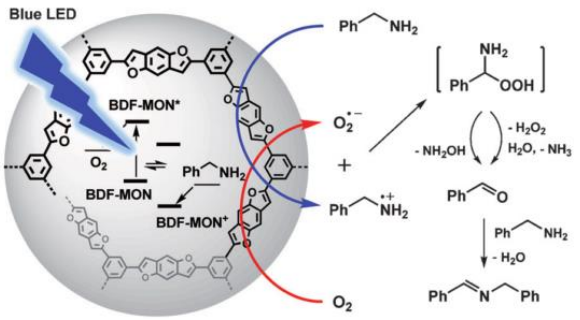

Fig. 25 The mechanism proposed for the homocoupling of benzylamines using benzodifuran based CPPs. Reproduced from Ref. 158. with permission from Wiley-VCH, copyright 2013.

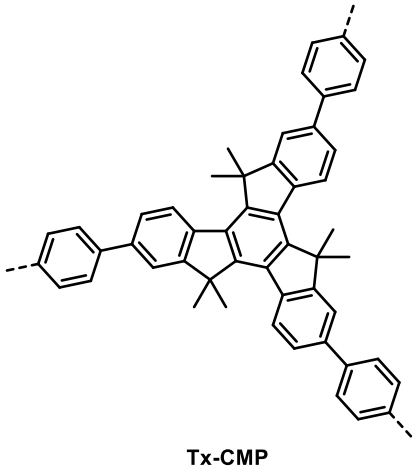

Fig. 26 Structure of truxene based CMP **TX-CMP.**[159]

CMP demonstrated high amine conversion (>99%) and selectivity (80-100%) across five uses. The scope examined demonstrated that the reaction could be applied to both the oxidative homocoupling of benzylamines and heterocyclic amines. However, homocoupling could not be achieved with aliphatic amines.

The homocoupling of amines has also been explored by Zhang and coworkers using a series of conjugated microporous poly(benzochalcogenadiazoles) (Fig. 27).[160] By modifying the chalcogen element, the position of valence and conduction bands could be engineered. The greatest photocatalytic activity was observed with **B-BT**, where the chalcogen element was sulfur, which obtained a conversion of 74% (blue LED, 3 h). In comparison, **B-BO** and **B-BS** (chalcogens are oxygen and sulfur respectively) gave conversions of 48 and 74% respectively. The authors attribute the superior photocatalytic properties of **B-BT** to the larger overpotential and a greater amount of electron-hole pairs generated upon irradiation. Zhang and coworkers also demonstrated that by altering the connectivity of benzo[*c*][1,2,5]oxadiazole based CMPs, the band gap could also be engineered for efficient photochemical amine homocoupling.[161]

Further work by Zhang and coworkers utilised conjugated microporous poly(benzothiadiazoles) (**B-BT**, Fig. 27) containing

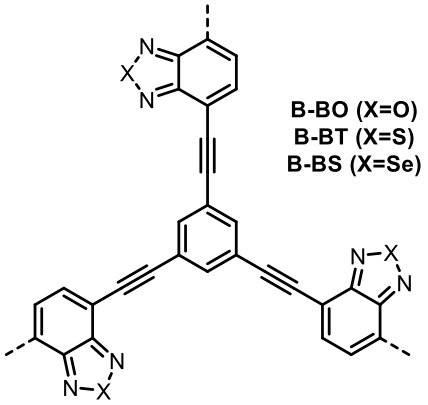

Fig. 27 Structure of a series of benzochalcogenide based CMPs containing oxygen (**B-BO**), sulfur (**B-BT**) and selenium (**B-BS**).[160]

immobilised TiO_2 nanoparticles for photochemical reactions.[162] By using the hybrid system of an organic CMP and inorganic TiO_2 nanoparticles, the charge separation obtained on photoirradiation was increased, leading to greater catalytic efficiency than was obtained using either the unmodified CMP or TiO_2 nanoparticles independently. With the photooxidative coupling of benzylamine, the CMP and TiO_2 nanoparticles gave conversions of 82% and <1% when used independently. This rose to a maximum of 98% upon doping the CMP with 80 wt% of TiO_2 when tested under the same conditions.

Zhang and coworkers have also reported on using band gap engineering of conjugated porous poly(benzobisthiadiazole) networks (Fig. 28).[163] Copolymerisation of 1,3,5-

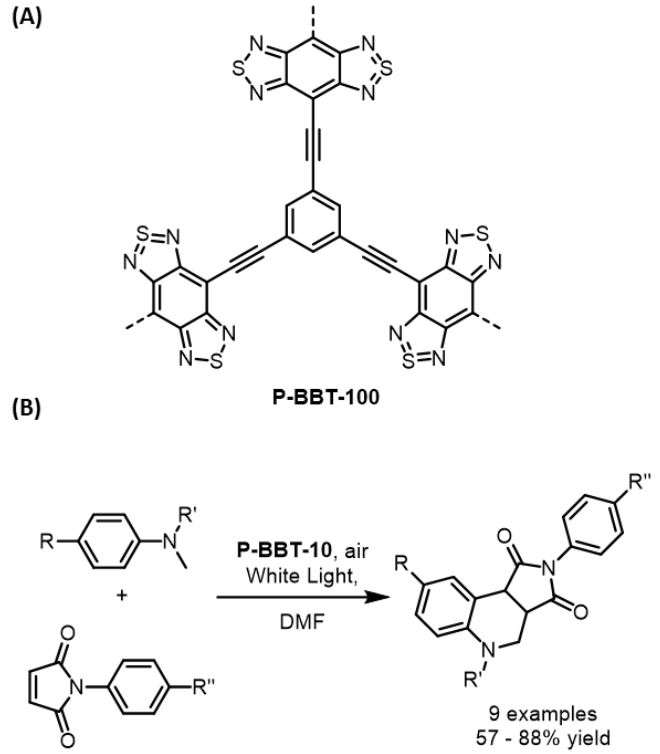

Fig. 28 (A) Structure of a benzobis(thiadiazole) based CMP. (B) Reaction scheme for the oxidative cyclisation of with *N*-phenylmaleimides with *N,N*-dialkylanilines.[163]

triethynylbenzene with varying ratios of the strongly electron withdrawing benzobisthiadiazole group and the weakly electron donating *p*-phenylene group allowed for control over the position of the valence and conduction bands. The optimal bandgap was obtained using 10% of the benzobisthiadiazole group. Oxidative cyclisation of *N,N*-dimethylaniline with *N*-phenylmaleimides to form tetrahydroquinoline using this CPP gave a yield of 82% (white LED, 24 h). Although the higher redox potentials were observed when 0% of the benzobisthiadiazole group was present, this CPP did not absorb enough visible light to be photocatalytically active.

Highly efficient aza-Henry reactions between nitroalkanes and tetrahydroisoquinolines have been reported using CPPs incorporating the organic dye Rose Bengal (Fig. 29).[164] The CPPs possessed high surface areas (801 – 833 $m^2 g^{-1}$) and could result in up to 100% conversion using visible light (60 W household bulb). The authors explored a wide substrate scope that demonstrated that the CPP catalysed process could tolerate various functional groups on the tetrahydroisoquinoline and various chain lengths of nitroalkanes. Good to excellent yields (80 – 97%) were obtained in each case and repeated use of the CPP 10 times did not result in significant loss in photoactivity. Similarly, high conversions have also been observed with CPPs based on Eosin Y, an organic dye with a similar structure to Rose Bengal.[165] The aza-Henry reaction has also been performed with ruthenium complexes as photocatalysts prepared by post synthetic modification of BODIPY CMPs as well phenanthroimidazole based CMPs.[88,166]

Efficient room temperature Suzuki-Miyuara coupling has been demonstrated by Zhang and coworkers using **B-BO** (Fig. 27) containing immobilised palladium nanoparticles with sizes ranging from 5 to 10 nm.[167] Using a white LED source, conversions as high as 98% were obtained with reaction times varying between 2 and 16 hours. The authors propose that the mechanism for this involves light induced charge separation, forming an electron-hole pair (Fig. 29). This electron then facilitates breaking of the carbon-halogen bond while the hole activates the carbon-boron bond of the boronic acid species.

Further work by Zhang and coworkers demonstrated that CMPs could also be applied to various Stille coupling reactions,

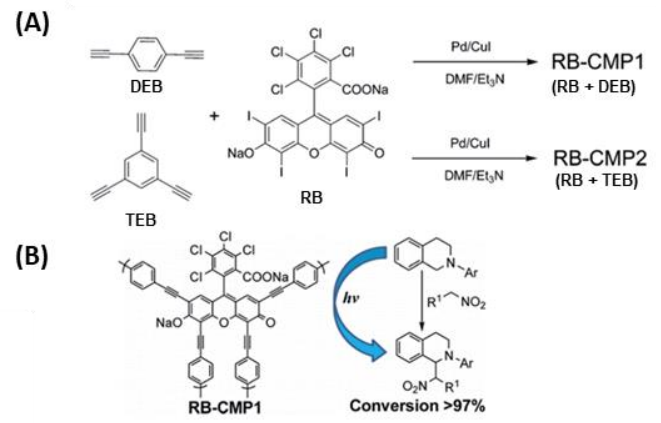

Fig. 29 (A) Synthetic scheme for preparing the rose Bengal CPPs. (B) The photochemical aza-Henry reaction using rose Bengal based CPPs as photocatalysts. Adapted with permission from Ref. 164. Copyright (2013) American Chemical Society.

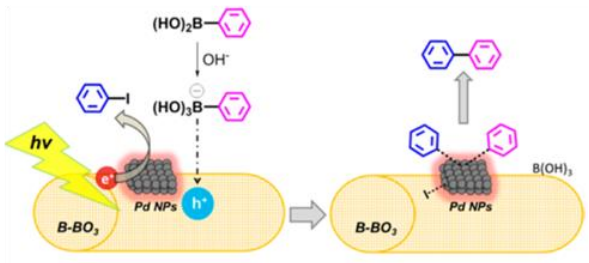

Fig. 30 Proposed mechanism for the Suzuki-Miyuara coupling reaction under light. Reprinted with permission from Ref. 167. Copyright (2015) American Chemical Society.

notably without the use of palladium as a catalyst (Fig. 31).[90] Irradiation of azulene based CMPs (1.2 W cm^{-2} white LED) resulted in the formation of an aryl radical by oxidative destannylation, which could react with an aryl iodide, activated by electron transfer from the excited LUMO. For electron deficient aryl halides (e.g. nitroarenes, cyanoarenes), good to excellent yields (56 – 93%) were obtained with electron rich arylstannanes, such as those bearing furan, thiophene and indole groups. However, the reaction did not tolerate non-electron deficient aryl iodides or electron poor arylstananes (pyridine, oxazoles), yielding no product or trace quantities only. Additionally, while the photocatalytic Stille coupling was successful with aryl iodides, no conversion was obtained when aryl bromides or aryl chlorides were tested. While **P-Az-B**, synthesised by Sonogashira-Hagihara cross coupling, did contain ca. 7 ppm of residual palladium, the authors demonstrate that this residue was not responsible for the catalysis as the reaction did not yield product in the absence of light.

2.1.5 Photoredox Catalysis Photoredox catalysis has recently emerged as a powerful tool for the activation and transformation of organic molecules. Many of the reported examples of photoredox chemistry utilise polypyridyl

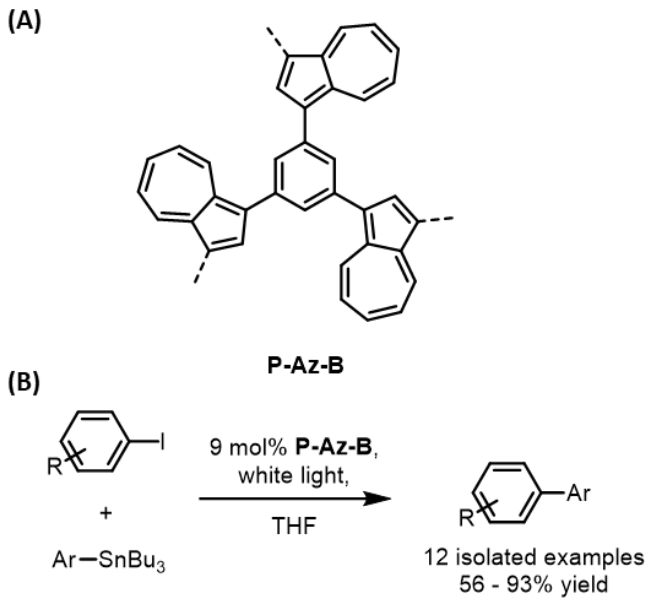

Fig. 31 (A) Structure of azulene based CMP, **P-Az-B.** (B) Reaction scheme for the photochemical Stille coupling using **P-Az-B.**[90]

ruthenium or iridium complexes, although organic photoredox catalysts have also received significant attention. The latter includes organic catalysts such as acridiniums, xanthenes and thiazines *etc*. With regards to CPPs, this is an emergent area of research with only a few reported examples. For a more general and in-depth explanation of photoredox catalysis, we direct the reader to representative reviews by MacMillan and coworkers.[168,169] and Romero and Nicewicz.[170]

Photochemical formylation and thiocyanation of indoles selectively in the C3 position has been reported with carbazole based CMPs.[171] Both of these reactions proceeded under ambient conditions using visible light (14 W LED lamp), with yields as high as 99% and a wide scope for substituent groups reported. In comparison, graphitic carbon nitride obtained a 31% reaction yield under the same formylation conditions. The proposed mechanism for the reaction involves the photoexcited CMP oxidising tetramethylethylenediamine (TMEDA) molecules to form radical cations, which then afforded iminium ions (Fig. 32). These ions can then undergo electrophilic addition to the indole, forming a tertiary amine intermediate. A second photoredox cycle converts this to an imine intermediate that is then hydrolysed to generate the formyl group. The thiocyanation reaction proceeds via a similar pathway, with the excited CMP reacting with the thiocyanate anion (from either KSCN or NH_4SCN), forming a thiocyanate radical that will react with the indole.

Photochemical hydroxylation of arylboronic acids has been reported in CPPs prepared via Knoevenagel condensation (Fig. 33A).[64] Using visible light (1.2 W/cm^2 LED lamp), yields in the region of 76 – 79% were obtained. The proposed mechanism for this reaction involved generation of the superoxide radical anion, which reacted with the boronic acid forming a peroxide radical. This species then abstracts a hydrogen atom from the sacrificial amine with subsequent rearrangement and hydroxylation yielding the corresponding phenol (Fig. 33B).

Wang *et al*. have reported on the use of a conjugated porous poly(benzobisthiadiazole) networks prepared by HIPE polymerisation as a photocatalyst for the reductive dehalogenation of α-bromoacetophenones to yield the corresponding acetophenone derivative (Fig. 34).[172] Even using a 23 W household energy saving light bulb, conversions greater than 95% could be obtained within 4 to 5 hours.

Recently, Ou *et al*. have reported on the application of carbazolic-cyano CMPs (**CC-CMP**) (Fig. 35A) to the visible light induced 1,2-formylarylation of *N*-arylacrylamides.[173] This process involves the generation of *tert*-butyloxy radicals by the excited state **CC-CMP** that could subsequently induce regioselective C-H activation of 1,3-dioxolane (Fig. 35B). The resulting alkoxyalkyl radical can subsequently undergo addition

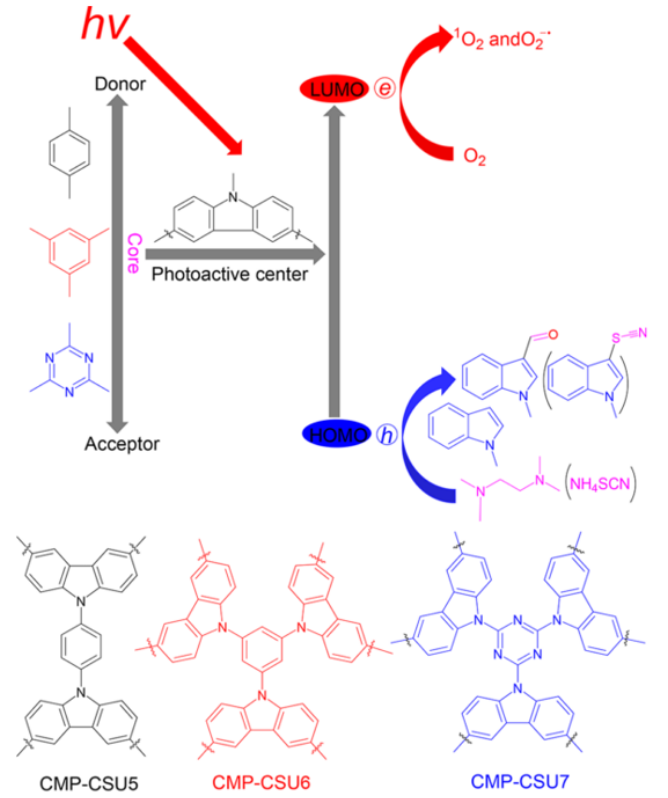

Fig. 32 Structure of carbazole based photoredox catalysts and their applications to the formylation and thiocyanation of *N*-methylindole. Adapted with permission from Ref. 171. Copyright (2018) American Chemical Society.

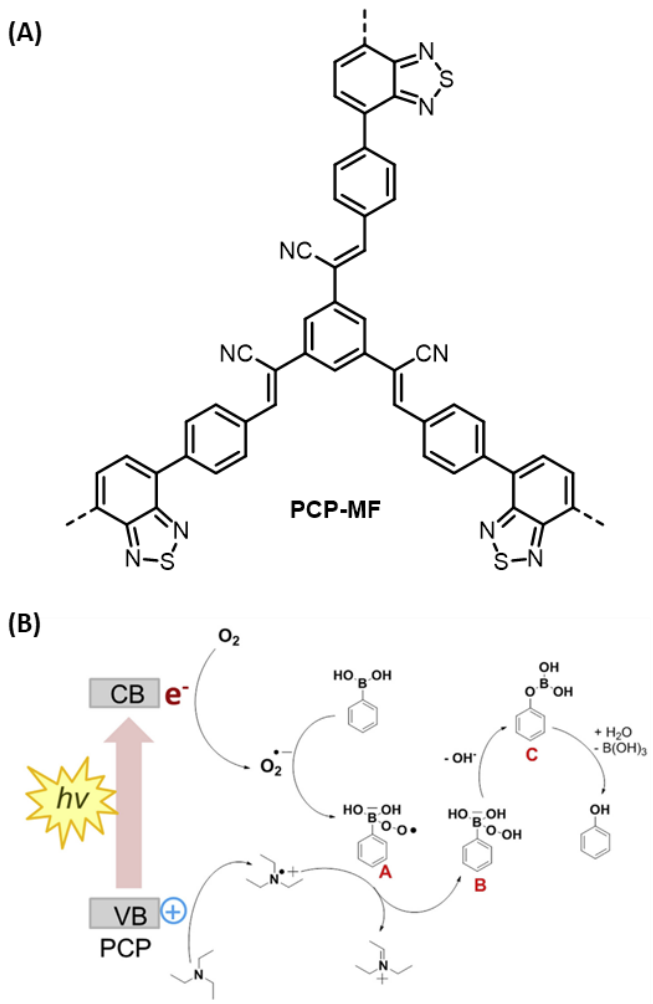

Fig. 33 (A) Structure of a BTZ-based CMP prepared via Knoevenagel condensation. (B)Proposed mechanism for arylboronic acid hydroxylation under photochemical conditions. Reproduced from Ref. 64 with permission from Elsevier, copyright 2017.

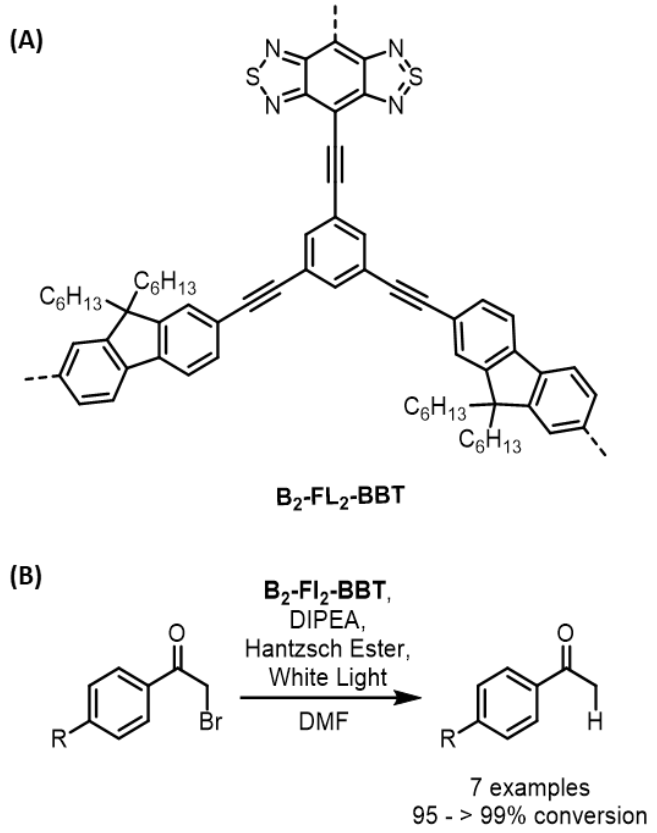

Fig. 34 (A) Structure of benzobis(thiadiazole)/fluorene based CMPs **B_2-FL-BBT**. (B) Reaction scheme for the reductive dehalogenation of α-bromoacetophenones using **B_2-FL-BBT**.[172]

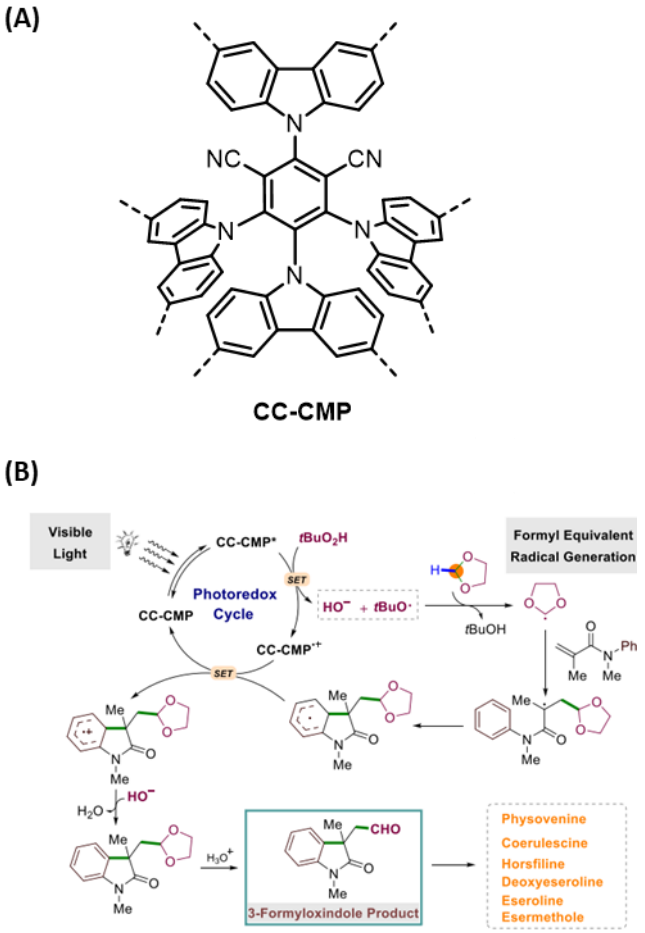

Fig. 35 (A) Structure of **CC-CMP**. (B) Proposed mechanism for the photocatalytic cascade 1,2-formylarylation of *N*-arylacrylamides using **CC-CMP**. Modified with permission from Ref. 173. Copyright (2019) American Chemical Society.

to the *N*-arylacrylamides. Intramolecular cyclisation, rearomatisation and hydrolysis of the acetal group resulted in 3-formyloxindoles in moderate to excellent yields (60-81%). The authors further demonstrate the utility of this metal free cascade reaction as part of a larger synthetic pathway for various bioactive alkaloids. Utilising 3-formyloxindoles as starting materials, the authors were able to synthesis alkaloids such as (±)-desoxyeseroline and (±)-esermethole, with scale up to gram quantities demonstrated.

2.1.6 Photochemical Polymerisations Photoinitiation of methyl methacrylate (MMA) polymerisation has been reported using a CMP based on the pH indicator phenolphthalein.[174] The mechanism for the initiation started with the excitation of the CMP to the triplet state using light > 420 nm. The photoexcited triplet CMP then reacted with the triethylamine hydrogen donor to generate the initiating radical species (Fig. 36). The reactions resulted in conversions typically in the range of 45 – 80%. Subsequent usage of the CPP photoinitiator resulted in decreased conversions (25%) possibly due to the consumption of the ketone group involved in the initiation step. It is noteworthy that the heterogeneous nature of CMP photocatalysts allows for separation of the catalyst from the reaction mixture by facile filtration, followed by precipitation to yield the final polymer. By contrast, employing homogeneous dyes as photopolymerisation catalysts, colouration of the resulting polymer can occur due to trace levels of the photocatalyst trapped during precipitation.

A CPP containing the thioxananthone (TX) group, **TX-CMP**, has been applied to the free radical polymerisations of methyl methacrylate (MMA) and to the cationic polymerisation of cyclohexene oxide.[175] The free radical polymerisations of MMA were carried out using either triethylamine or the $Ph_2I^+PF_6^-$ salt as the co-initiator. For the cationic polymerisation, $Ph_2I^+PF_6^-$ was

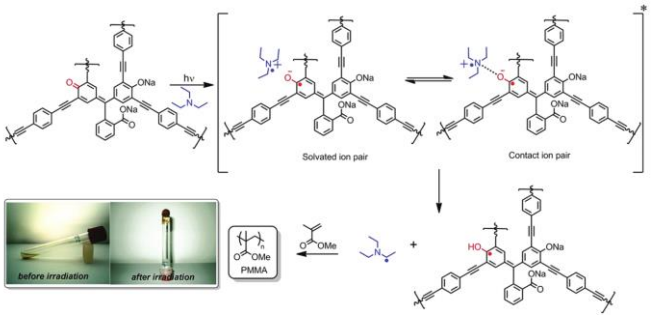

Fig. 36 Proposed initiation mechanism for methyl methacrylate polymerisation using a phenolphthalein-based polymer network. Reprinted with permission from Ref. 174. Copyright (2012) American Chemical Society.

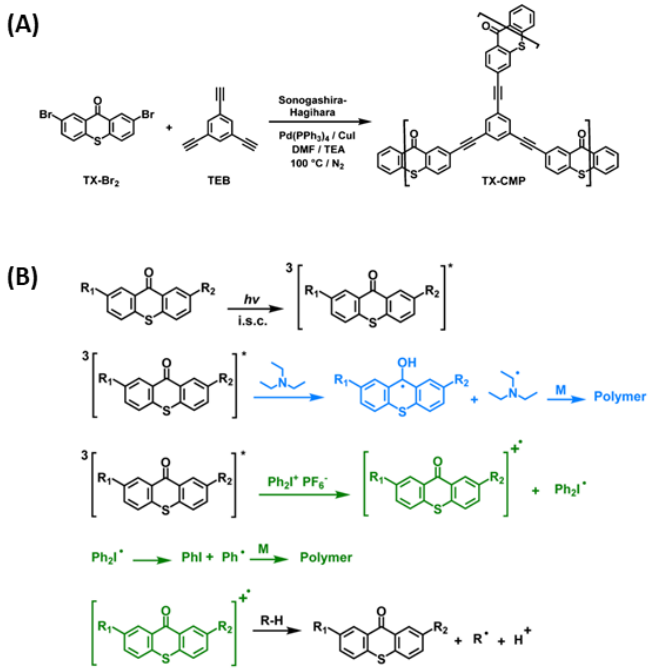

Fig. 37 (A) Synthetic scheme for preparing **TX-CMP** and (B) proposed mechanism for initiation of free radical polymerisation using thioxanthone based CPP and an amine or iodonium salt co-initiator. Adapted with permission from Ref. 175. Copyright (2014) American Chemical Society.

used as co-initiator in conjunction with dimethylacetamide (DMA) or THF as hydrogen donor compounds (Fig. 37).

Photochemically initiated radical polymerisation of MMA has also been demonstrated in hierarchically porous polyHIPEs containing carbazole and benzooxadiazole groups.[176] The reaction was carried out at room temperature using triethylamine as the co-initiator and using a 23 W household energy saving bulb as the source of light. The suggested mechanism for the initiation process involved oxidation of triethylamine by the photogenerated hole within the CPP, forming a radical cation. Reaction of this species with another molecule of triethylamine yields a radical that initiates polymerisation of MMA (Fig. 38).

2.1.7 Photochemical Hydrogen Production As an alternative to fossil fuels and nuclear energy, generating energy from combustion of hydrogen is considered to be a relatively green and environmentally friendly process. This has led to it being extensively researched over several decades. Industrial production of hydrogen from water typically involves electrolysis, however, photocatalytic water splitting has also been explored. This has mainly been explored using inorganic semiconductor photocatalysts but in recent years CPPs have demonstrated that they also have application in this area.

The mechanism for the photochemical water splitting process starts with the catalyst absorbing light of sufficient energy. This leads to excited electrons occupying the conduction band, generating holes (h^+) in the valence band (Fig. 39). These exciton pairs can then drive the individual components of process, described by equations (1) and (2).

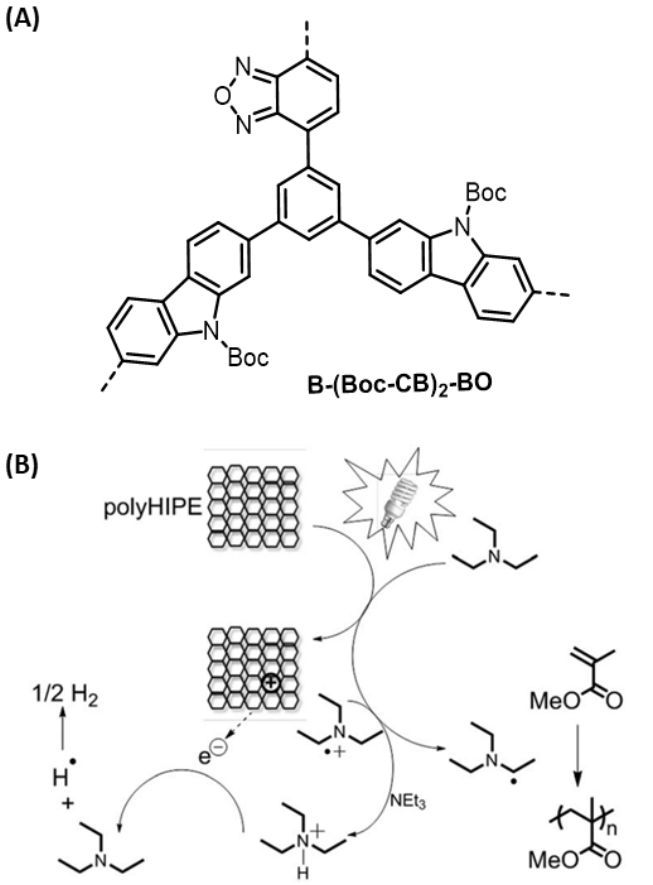

Fig. 38 (A) Structure of benzooxadiazole-carbazole based CMP **B-(Boc-CB)$_2$-BO**. (B) Proposed mechanism for initiation of MMA polymerisation under visible light using a conjugated porous polyHIPE. Reproduced from Ref. 176 with permission from the Royal Society of Chemistry, copyright 2014.

$$2\ H_2O + 4\ h^+ \rightarrow 4\ H^+ + O_2 \quad (1)$$

$$2\ H^+ + 2\ e^- \rightarrow H_2 \quad (2)$$

The first equation represents the oxidation reaction in which the photochemically generated hole drives the splitting of water into protons and oxygen. The excited electron occupying the conduction band then drives the reduction reaction (2),

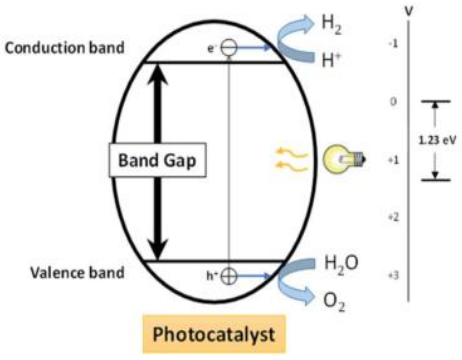

Fig. 39 Representation of water splitting using semi-conductor materials. Reproduced from Ref. 37 with permission from the Royal Society of Chemistry, copyright 2017.

leading to the generation of the H_2 gas that will be used as a fuel. Combining these half-cell equations results in the overall redox equation describing photochemical water splitting (3).

$$2\ H_2O(l) \rightarrow 2\ H_2(g) + O_2(g) \qquad (3)$$

The overall water splitting process is endergonic, with a Gibbs free energy change of 237 kJ mol^{-1} or a reduction potential of 1.23 V. Therefore, the band gap of any prospective material should exceed 1.23 eV, corresponding to a 1008 nm photon of light.

Some of the first reports of hydrogen evolution with porous conjugated polymers relates to graphitic carbon nitrides (g-C_3N_4).[177] Antonietti and coworkers reported that carbon nitrides, prepared via heating cyanamide to temperatures in between 673 and 873 K, could evolve hydrogen from water at a rate of 0.1 – 4 µmol h^{-1} even without the use of a noble metal (Fig. 40).[178] Upon addition of 2-4% of Pt metal, the photocatalytic activity was observed to increase. An analogous material to graphitic carbon nitride are heptazine-based networks (HEP-g-C_3N_4). Thomas and coworkers have reported on the synthesis of such networks by the reaction of cyanuric chloride with different aromatic diamine linkers at room temperature.[179] Under UV irradiation, 3 wt% Pt and using triethanolamine as an sacrificial agent, the heptazine based materials were able to attain H_2 evolutions rates as high as 21 µmol h^{-1}.

Hydrogen evolution has been reported in a series of CPPs by Sprick *et al*. prepared using feed ratios of benzene and pyrene monomers (Fig. 41A).[89] The materials obtained possessed surface areas ranging from 597 to 1710 $m^2\ g^{-1}$ and were all capable of producing hydrogen at a steady rate under visible light illumination. Notably, this could occur in the absence of a noble metal co-catalyst, however it was suggested that residual palladium from synthesis could be an influence. As the HOMO and LUMO of phenylene lie higher and lower, respectively, than the equivalent phenylene MOs, increasing pyrene content leads to a bathochromic shift in the band gap (Fig. 41B). The result of this is that photons from most of the visible spectrum are able to be used to generate electrons to drive the reaction. For the most part the optical band gap correlated with both the hydrogen evolution and the rate of hydrogen evolution. This

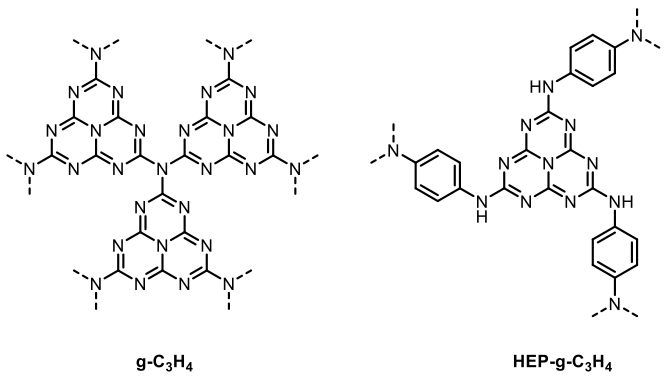

Fig. 40 Structures of graphitic carbon nitride and heptazine-based g-C_3N_4.

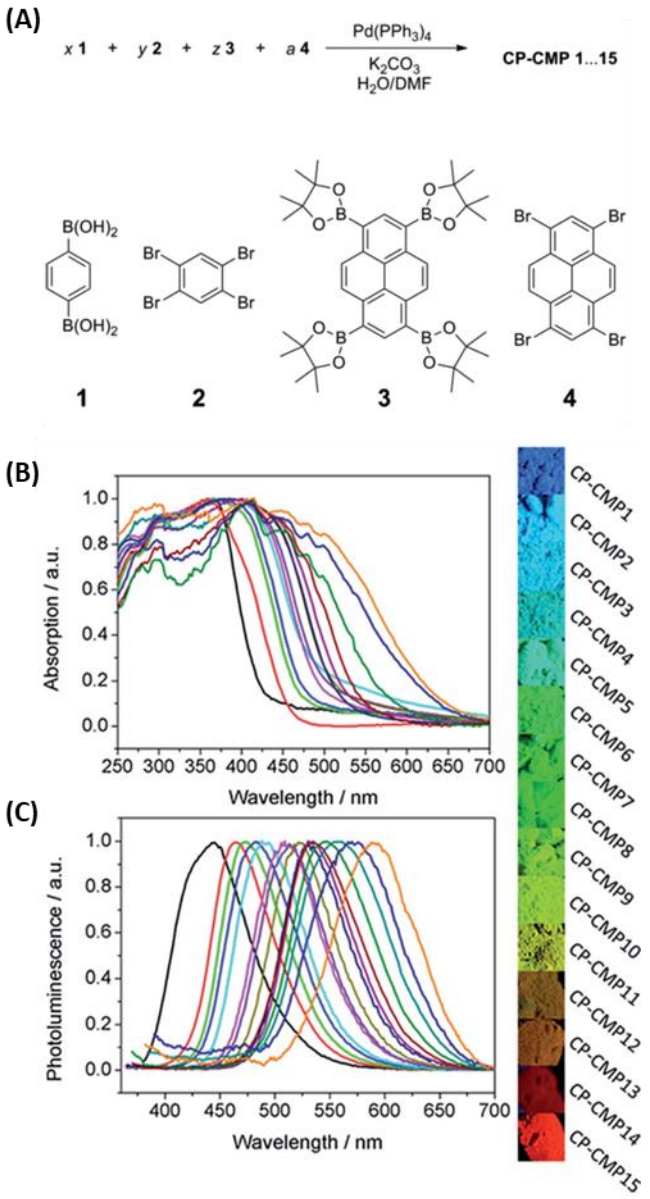

Fig. 41 (A) Scheme for the synthesis of benzene-pyrene based CMPs. (B)Benzene-pyrene copolymers for photochemical hydrogen generation. (A) UV-vis absorption spectra of the polymer series. (B) Photoluminscence spectra of the polymer series. Photographs of the copolymer series under 365 nm light irradiation (right). Adapted with permission from Ref. 89. Copyright (2015) American Chemical Society. Available under CC-BY.

reached a maximum rate of 17.4 µmol h^{-1} with a 2.33 eV band gap CPP. With band gaps above 2.33 eV, a drop in the hydrogen production was observed, which the authors suggest is due to non-radiative relaxation processes.

Subsequent studies by Sprick *et al.* further extended the scope of CPPs, investigating different structural features and the corresponding effects on photocatalytic activity (Fig. 42).[140] While none of the polymers were active under visible light, they could achieve hydrogen evolution under UV irradiation. The yields obtained were greater than had been previously reported by the group and likewise did not require a metal co-catalyst. Their results demonstrated that extended linkers along with planar monomers in general led to increased photoactivity.

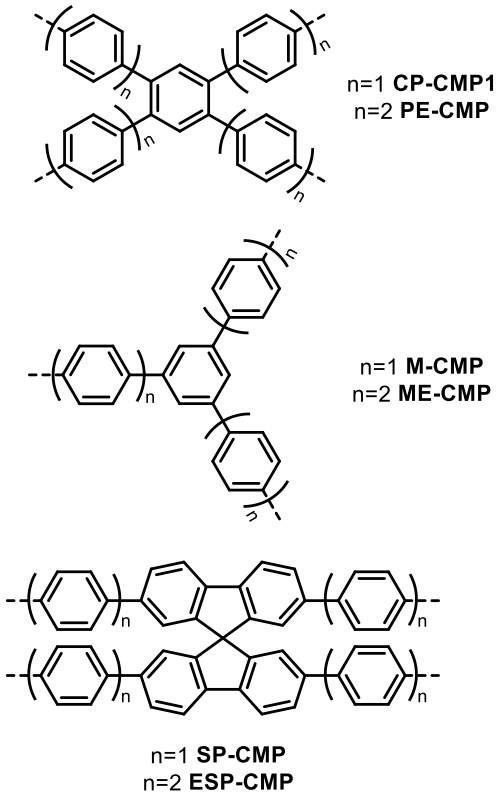

Fig. 42 Structure of a series of CMPs studied for photocatalytic applications.[140]

Hydrogen evolution has also been reported using perylene based CMPs by Xu *et al*.[180] The authors reported that the optical and structural characteristics of these polymers could be tailored by changing the substitution patterns of the benzene-linking group. The observed rate of hydrogen evolution correlated with several structural parameters, namely increasing extent of conjugation, light absorbed and surface area. The lowest hydrogen evolution rate was from 37.1 µmol h^{-1} g^{-1} for **PrCMP-1**; this increased to 93.8 µmol h^{-1} g^{-1} for **PrCMP-2**. The highest evolution rate of (121 µmol h^{-1} g^{-1} was observed for **PrCMP-3**, which possessed benzene linking groups with a 1,2,4,5- substitution pattern (Fig. 43). However, Xu *et al*. also observed that in comparison to other CMP systems, the hydrogen evolution rate is low. The reason the authors suggest for this is the lack of functional groups that favour charge migration through the network, which has been highlighted as a design feature by others. Subsequent work on perylene based CMPs by the same group yielded similar conclusions: that factors such as extent of conjugation, planarity, light absorbed and surface area all influence the HER and that groups to promote charge migration are key.[181] Further work by Xu *et al*. have demonstrated that chemical structure and the ratio of donor to acceptor groups in a series of BTZ based CPPs played important roles in determining the hydrogen evolution.[182]

Jiang and coworkers have reported on photochemical hydrogen evolution using dibenzothiophene-*S,S*-dioxide based CMPs (Fig. 44).[183] The authors demonstrated that the rate of the hydrogen evolution depended upon the length of the cross-

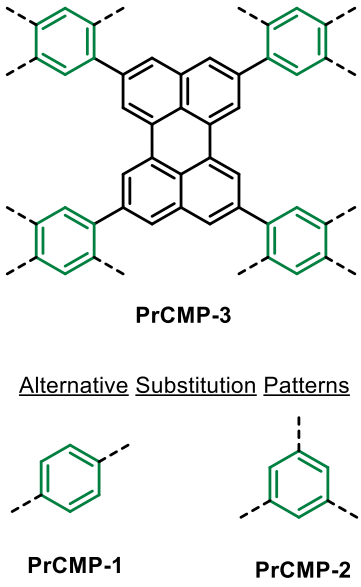

Fig. 43 Structure of perylene based CMPs.[180]

linker, with the highest efficiency obtained with the shortest cross linking unit. Under conditions of visible light illumination, this polymer exhibited a hydrogen evolution rate of 2460 µmol h^{-1} g^{-1}. Upon doping with 3% Pt, the hydrogen evolution rate increased to 4600 µmol h^{-1} g^{-1} under visible light and 9200 µmol h^{-1} g^{-1} under UV-Vis illumination.

Jiang and coworkers later demonstrated that the linking pattern of the dibenzothiophene-*S,S*-dioxide unit also influences the rate of hydrogen evolution.[184] They prepared two CMPs, **PyDOBT-1** and **PyDOBT-2**, by Suzuki-Miyuara coupling between pyrene and dibenzothiophene-*S,S*-dioxide units. The dibenzothiophene-*S,S*-dioxide groups in the former were linked through the 3- and 7- positions while the latter was connected through the 2- and 8- positions (Fig. 45). Using visible light

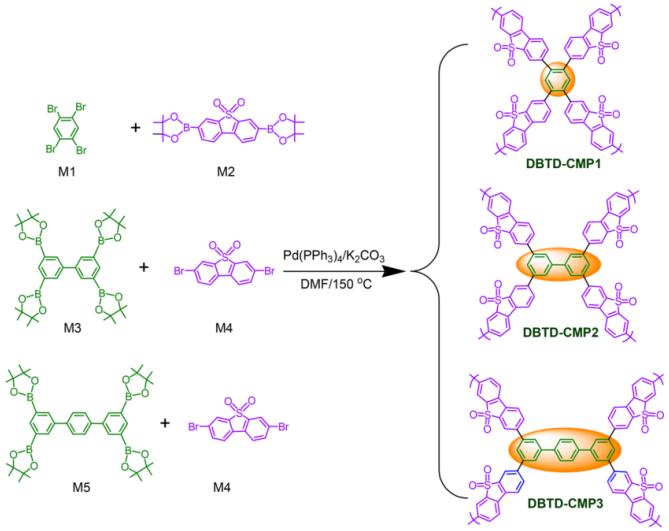

Fig. 44 Synthetic scheme for a series of dibenzothiophene-*S,S*-dioxide based CMPs. Adapted with permission from Ref. 183 Copyright (2018) American Chemical Society.

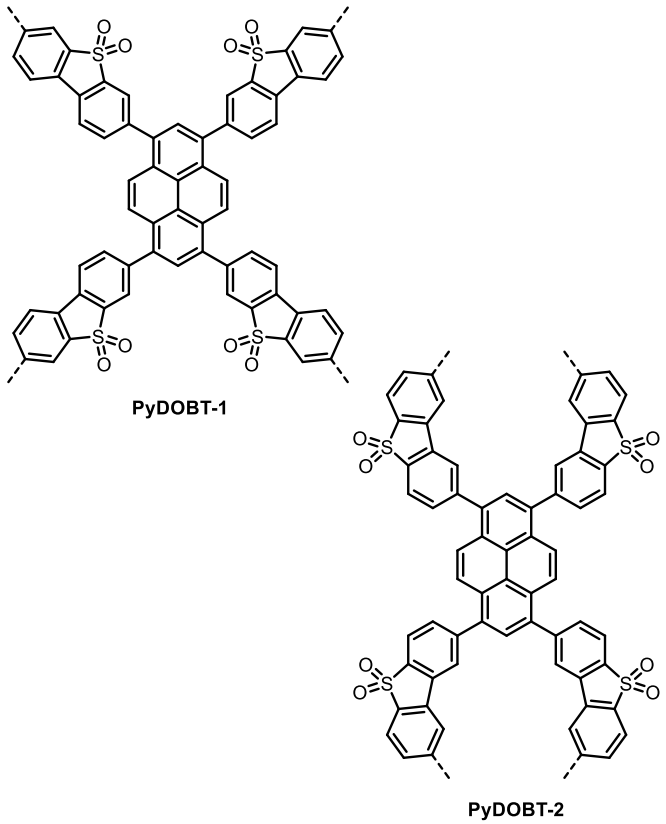

Fig. 45 Structures of dibenzothiophene-*S,S*-dioxide and pyrene copolymers with differing connectivity (3,7- and 2,8- for PyDOBT-1 and PyDOBT-2 respectively).[184]

without a Pt co-catalyst, **PyDOBT-1** demonstrated a hydrogen evolution rate of 5697 μmol h^{-1} g^{-1}. This rose to 8523 μmol h^{-1} g^{-1} upon the addition of 3 wt% Pt, and to 12986 μmol h^{-1} g^{-1} upon the use of UV-Vis light. In comparison, the **PyDOBT-2** evolved hydrogen at a rate of 2113 μmol h^{-1} g^{-1}, rising to 3190 μmol h^{-1} g^{-1} using UV-vis light and a Pt co-catalyst. The superior hydrogen evolution rate of **PyDOBT-1** was attributed to the 3,7- linking pattern which increased the conjugated chain length and coplanarity of the CMP, which in turn facilitated charge migration.

Sprick *et al*. have also studied dibenzothiophene-*S,S*-dioxide based CMPs as catalysts for hydrogen evolution and compared their performance to linear, non-porous analogues.[185] One of the CMPs studied, **S-CMP3**, demonstrated the maximum hydrogen evolution of 6076 μmol h^{-1} g^{-1} using UV-Vis light which is vastly superior to its linear analogue (1177 μmol h^{-1} g^{-1} under the same conditions). However, the other CMPs investigated performed poorer in comparison to non-porous linear analogues. The authors suggest that the reason for this is that microporosity can benefit hydrogen evolution provided that the building blocks do not distort the planarity of CMP, thus limiting charge migration. In addition, Sprick *et al*. demonstrated that the wettability of the material was also a factor.

2.2 CPPs as Heterogeneous Catalysts

2.2.1 CPP Supported Catalysis One of the most useful applications of CPPs is to provide a solid platform for

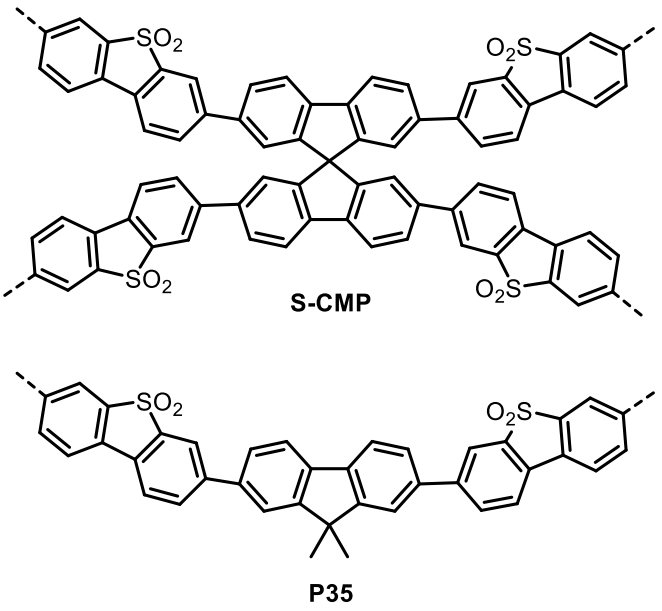

Fig. 46 Structures of a spirobifluorene- dibenzothiophene-*S,S*-dioxide CMP **S-CMP** and a linear analogue **P35**.[185]

immobilising catalytically active entities. There are two strategies which can be adopted for this. The first strategy is to incorporate catalytically active moieties into the design of CPPs. As such the catalytic site is part of the polymer network itself. This is effectively demonstrated by the incorporation of the 4-dimethylaminopyridine (DMAP) group into a CPP by utilising a dibrominated building block (Fig. 47).[186] The resultant CPP was used as an efficient heterogeneous catalyst for the acylation of alcohols using acetic anhydride. The catalyst demonstrated a diverse scope, with excellent yields (>99%) obtained under both batch and continuous flow conditions (even after 536 h of continuous use).

The alternative approach to incorporating catalytically active moieties into the CPP is to use the polymer network as a structural support upon which catalytic sites, such as metal ions, atoms or clusters are immobilised. This approach is demonstrated by the silver-catalysed heterocyclisation of 4-pentynoic acid using monolithic CMPs featuring Ag(I) ions immobilised via sulfur groups on the polymer network.[85] **CMP_1** first prepared by Sonogashira-Hagihara cross coupling

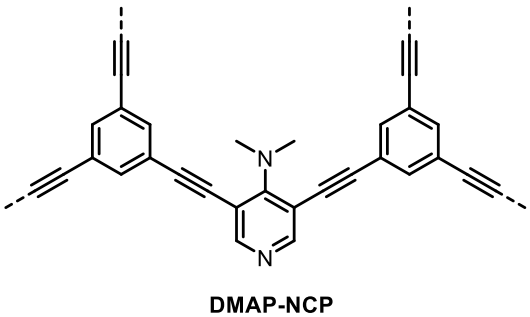

Fig. 47 Structure of DMAP based CMP via for use in acylation of alcohols.[186]

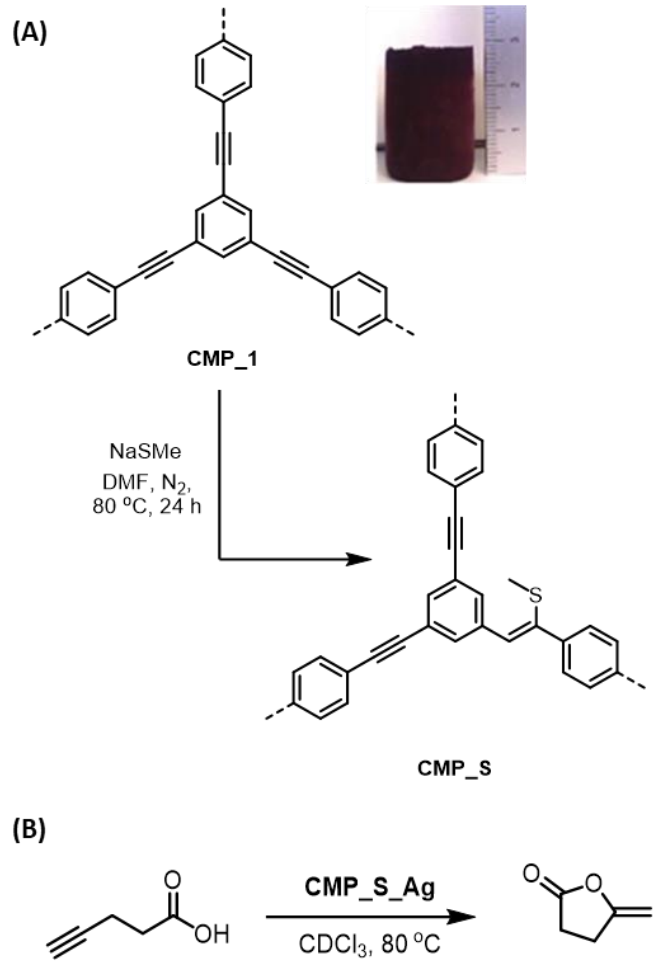

Fig. 48 (A) Post-synthetic modification of **CMP_1** via thiol-yne chemistry to **CMP_S**. Picture shows monolith of **CMP_1**. (B) Reaction scheme for the cyclisation of 4-pentynoic acid. Adapted from Ref. 85 with permission from the Royal Society of Chemistry, copyright 2015.

before being subjected to a thiol-yne modification to install sulfur containing groups (see **CMP_S,** Fig. 48A). The silver was then loaded onto the polymer using $AgNO_3$ solution. Within 5 hours, quantitative yields of 5-methyldihydrofuran-2(3*H*)-one were obtained from 4-pentynoic acid (Fig. 48B), with the CMP demonstrating no loss in efficiency or Ag content after 5 cycles. In comparison, the $AgNO_3$ salt was tested under similar reaction conditions but only resulted in low conversions even when used for 24 hours.

Liu *et al*. have also demonstrated an alternative strategy to load silver nanoparticles onto aldehyde bearing CPP, **PHTT_CHO**, using Tollen's reagent (Fig. 49).[144] This process oxidised aldehyde groups present on the CPP to carboxylic acid groups with concordant reduction of Ag(I) ions to Ag(0), forming **PHTT_Ag**. The material was subsequently applied to the reduction of various nitroaromatics using sodium borohydride. At room temperature, high conversions (90 – 99%) were obtained within 6 – 12 hours.

Lee *et al*. have also reported on the catalytic reduction of 4-nitrophenol, utilising a free standing CMP membrane containing immobilised Ag nanoparticles.[115] The CPP membrane was fabricated using a polyvinylpyrrolidone (PVP) electrospun

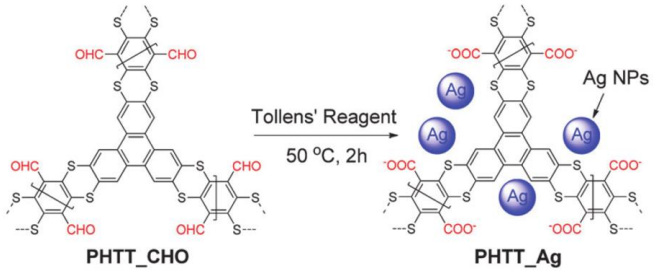

Fig. 49 Loading of silver nanoparticles onto a CPP. Adapted from Ref. 127 with permission of the Royal Society of Chemistry, copyright 2015.

template around which a thin layer of CMP was grown via Sonogashira-Hagihara coupling between 1,3,5-triethynylbenzene and 1,4-diiodobenzene. The PVP template was then removed by solvent extraction to yield the CMP membrane with a hollow tubular morphology exhibiting macroporosity from the template as well as meso- and microporosity associated with the CPP. By utilising PVP doped with Ag nanoparticles that were reduced by the dimethylformamide that was also used to dissolve the template, Ag doped CMP membranes, **CMP@Ag**, were obtained. Using a simple setup involving an inverted glass vial covered with membrane, **CMP@Ag** could be used for the Ag catalysed reduction of 4-nitrophenol to 4-aminophenol using sodium borohydride (Fig. 50). Operating under gravity at a flow rate of 0.2 mL min^{-1} full conversion of 4-nitrophenol was obtained using **CMP@Ag** membrane (Fig. 50B) while no change was observed using the CMP membrane in the absence of Ag nanoparticles (Fig. 50A). In addition to Ag nanoparticles, similar chemistry has also been explored using a CMP based on the 1,2,3-triazolyl unit with immobilised Au nanoparticles.[187] Wei *et al*. determined that their CMP-Au nanoparticle composite exhibited a rate coefficient for nitrophenol of 13.5 x 10^{-3} s^{-1}. By comparison, using chloroauric acid ($HAuCl_4$) in place of the nanocomposite as the reduction catalyst resulted in a significant decrease in the rate coefficient to 3.82 x 10^{-3} s^{-1} min^{-1}. The authors postulate that the high surface area and a homogeneous dispersion of the gold nanoparticles provides good accessibility of the nitrophenol to the catalytic sites.

Kim *et al*. have also reported on the reduction of nitroaromatic compounds using a compressible monolithic CPP prepared by Sonogashira-Hagihara coupling reaction as a gel

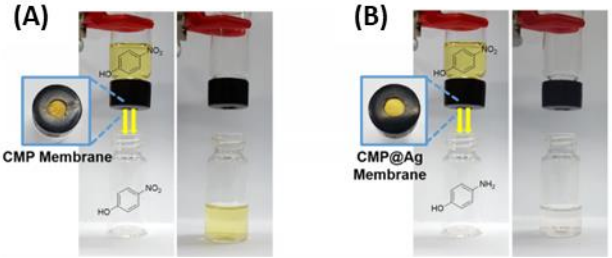

Fig. 50 Photographs of the experimental set up for reduction of 4-nitrophenol using CMP membranes without (A) and with (B) immobilised Ag nanoparticles. The pale-yellow colour disappears (indicating reduction of 4-nitrophenol) after passing the solution through the **CMP@Ag** membrane but not the **CMP** membrane. Adapted from Ref. 115 with permission of Springer Nature, copyright 2017. Available under CC-BY-4.0.

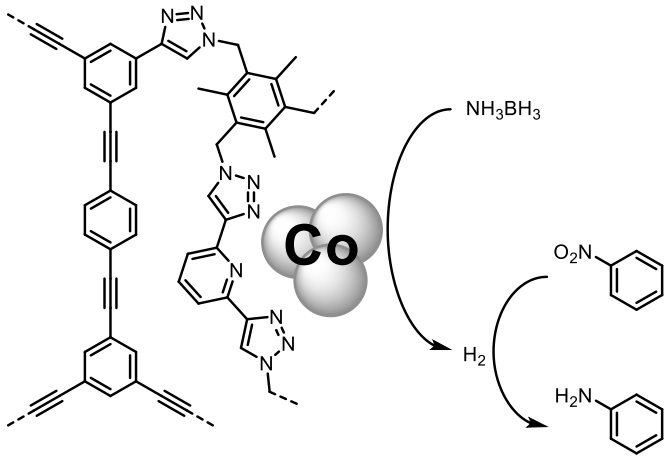

Fig. 51 Schematic representation of the tandem dehydrogenation of ammonia borane, generating hydrogen for the reduction of nitroarenes using cobalt loaded CMPs.[188]

without stirring the mixture.[188] The hydrophobic monolith was then functionalised by alkyne-azide click chemistry, introducing triazole groups that presented bonding sites for Co(II) ions to bind. Reduction of the Co(II) ions led to cobalt nanoparticles incorporated into the monolithic structure. This material was then applied to the tandem dehydrogenation of ammonia borane followed by the hydrogenation of nitro compounds (Fig. 51). By manually compressing and releasing the monolith in the reaction mixture (2 seconds per cycle), the rate of 4-nitrophenol reduction was enhanced relative to stirring or static conditions (5.5 and 7.5-fold increase respectively). Overall using the compression and release method, the CMP could attain high conversions on the minute timescale. Kim *et al*. have also investigated the use of compressible monolithic CMP sponges with immobilised silver nanoparticles for the reduction of nitrophenol.[189] Thiol-yne chemistry was used to modify the polymer and introduce sulfur groups. *In situ* reduction of Ag(I) ions led to the growth of silver nanoparticles. The resulting nanocomposite (with 5.39 wt% Ag) was able to reduce nitrophenol with a rate constant of 7.61 x 10^{-3} s^{-1}, which the authors identify as being larger than other metal-monolithic catalysts such as carbon-Ag (0.88 x 10^{-3} s^{-1} at similar Ag loading).[190] The reason they attribute improved rate to is the enhanced fluid exchange, via compression and release of the sponge.

Iridium bipyridine based CMPs have been reported for the catalytic dehydrogenation of formic acid into H_2 and CO_2.[191] The bipyridine units were first introduced during the synthesis via Sonogashira-Hagihara coupling, then the iridium metal introduced post-synthetically (Fig. 52A). The dehydrogenation of formic acid took place in aqueous media at elevated temperatures and pressures, with conversions reaching as high 99.9% (based on formic acid) and turnover frequencies as over 120 000 h^{-1} (Fig. 52B). In addition, the material exhibited good stability with little iridium leaching observed over more than 6 runs. Iridium bipyridine based CMPs have also be used as catalysts for the reductive amination of ketones.[192] Bipyridine based CMPs with a similar framework have also been used to

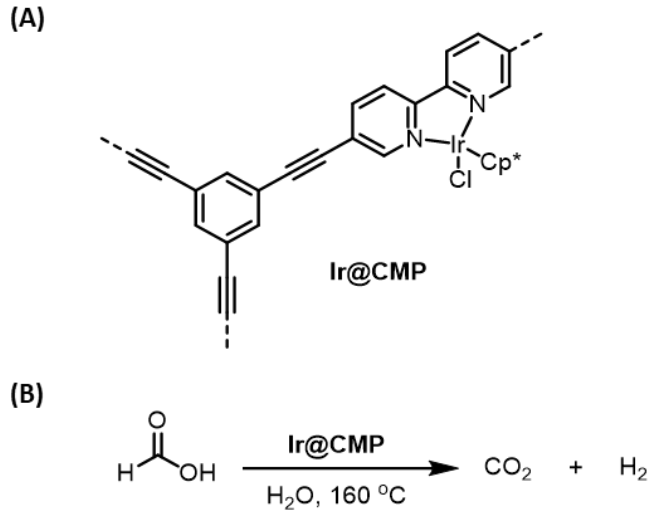

Fig. 52 (A) Structure of **Ir@CMP**. (B) Reaction scheme for the dehydrogenation of formic acid using **Ir@CMP**.[191]

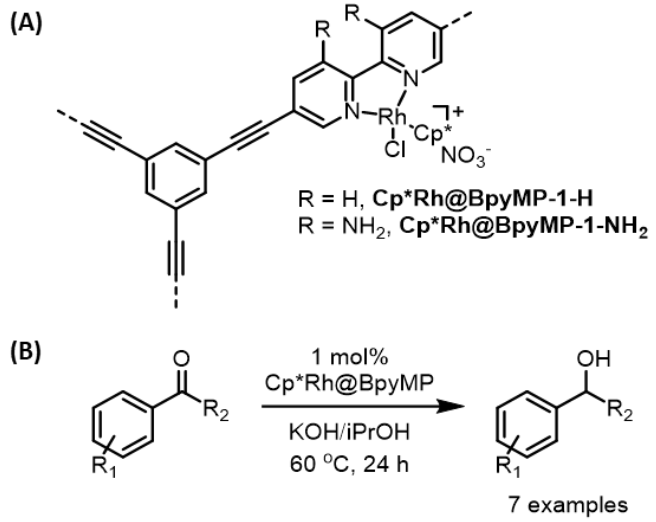

Fig. 53 (A) Structure of **Cp*Rh@BpyMP**. (B) Reaction scheme for the transfer hydrogenation of α-aryl ketones.[193]

form complexes with the pentamethylcyclopentadienylrhodium species (Fig. 53A).[193] These were then used as transfer hydrogenation catalysts for α-aryl ketones into α-aryl alcohols (Fig. 53B).

A CMP incorporating a *N*-heterocyclic carbene copper (I) complex has been reported by Zhou *et al*. (Fig. 54A). **CMP-iPr(CuCl)** was demonstrated to be an efficient catalyst for the hydrosilylation of terminal alkynes using boryldisiloxane (Fig. 54B).[78] Good yields were obtained and although a wide variety of functional groups were tolerated, electron withdrawing groups slowed down the rate of the reaction. **CMP-iPr(CuCl)** was also applied to the hydrosilylation of CO_2 in the presence of sodium *tert*-butoxide, which converted the chlorine atoms into a tert-butoxide group (Fig. 54C). While the initial reported yield was only 26.3%, increasing the quantity of carbene CMP from 1.67 to 10 mol% increased the yield to 91.7%.

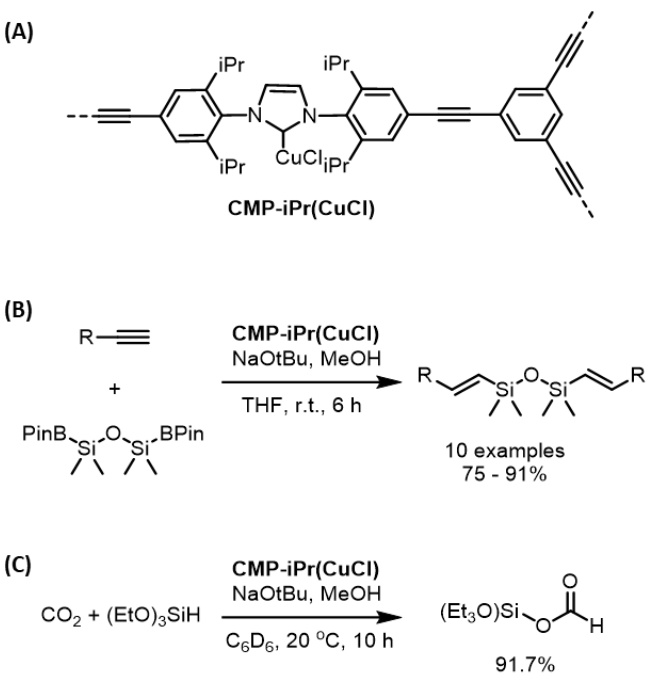

Fig. 54 (A) Structure of **CMP-IPr(CuCl)**. (B) Scheme for hydrosilylation of terminal alkynes. (C) Scheme for hydrosilylation of CO_2.[78] BPin = pinacol ester.

The oxidation of various substrates has been realised using various CMPs featuring metal-ligand complexes (Fig. 55A). For example, iron-porphyrin based CMPs have demonstrated conversions of up to 98%, with high selectivity for the sulfide over the corresponding sulfoxide (Fig. 55B).[194] This efficiency was maintained even when using air as the source of oxygen. This same CPP was later also applied to the epoxidation of various olefins, including cyclic and acyclic alkyl and aromatic alkenes (Fig. 55C).[195] Similarly, epoxidation of alkenes has been demonstrated using a manganese-salen based CMP.[196] The epoxidation of alkenes has also been reported by Nguyen and coworkers, who utilised manganese porphyrin based CMPs to achieve the epoxidation of styrenes and divinylbenzene.[197]

The conversion of fructose into hydroxymethylfurfural (HMF), which is a step during the synthesis of lactic acid, has been reported using CMPs bearing aliphatic sulfonic acid groups by Cho *et al*.[198] The material was prepared by Sonogashira-Hagihara coupling, to give **TA-CMP** (Fig. 56A), followed by thiol-yne modification at defect sites to yield **H-TA-CMP-ASO$_3$H** (Fig. 56B). This reaction with terminal alkyne sites led to the incorporation of the aliphatic sulfonic acid groups that allows the material to act as a Brønsted acid (Fig. 56C). Conversions in the region of 85 – 92% were obtained when using temperatures between 100 – 140 °C. At 120 °C, **H-TA-CMP-ASO$_3$H** exhibits a turnover number of 45.5, which the authors compared with another CMP previously reported by Mondal *et al.*, that attained a TON of 6.11 at the same temperature.[199] The authors propose that a reason for high TONs of **H-TA-CMP-ASO$_3$H** could be due to its thin shell architecture in combination with its microporosity, which Cho *et al*. have previously reported as important factors in the application of POPs to organocatalytic

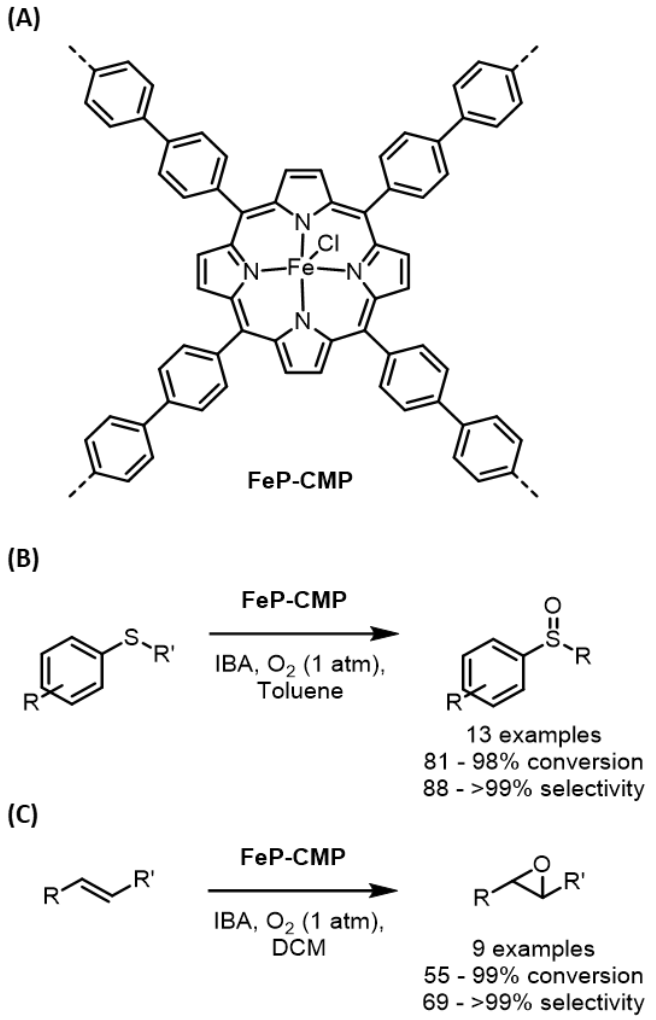

Fig. 55 (A) Structure of **FeP-CMP**. (B) Oxidation of thioanisoles using **Fe-CMP**. (C) Epoxidation of alkenes using **Fe-CMP** as the catalyst.[194]

reactions.[200] Nguyen and coworkers have also studied the conversion of fructose to HMF using a sulfonic acid functionalised CMP.[201] It was noted that the large surface area provided by the CMP afforded catalytic performances comparable to homogeneous sulfonic acid catalysts and greater than Amberlyst 15 (a polystyrene resin containing sulfonic acid groups).

2.2.2 Coupling Reactions In addition to facilitating photochemical coupling reactions, CPPs can also act as catalysts in coupling reactions not driven by light. For example, CMPs based on the bipyridyl group can act as heterogeneous ligands for oxidative Heck reactions.[202] The CMP acted as a bifunctional ligand, coordinating palladium to both the alkyne and pyridine-N sites. This in combination with the confinement of reagents within the CMP's porous structure led to oxidative Heck reactions with high selectivity for the linear olefin over the branched isomer (Fig. 57). Moreover, the selectivity of the reaction was approximately 30 times greater when using the heterogeneous ligand in comparison to a bipyridine based monomer equivalent. More recently, a bipyridine based CMP

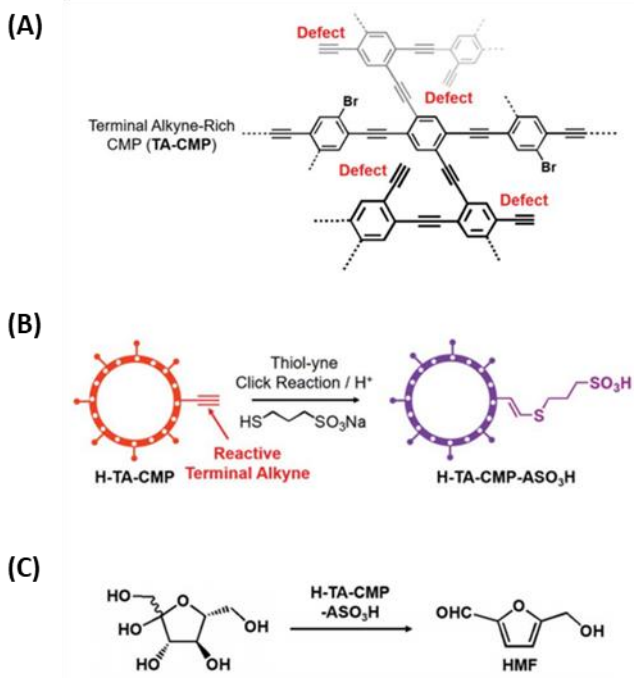

Fig. 56 (A) Representative structure of **TA-CMP** with defect sites. (B) Post synthetic modification of **TA-CMP** to **H-TA-CMP-ASO$_3$H** via thiol-yne chemistry. (C) Reaction scheme for the conversion of fructose into hydroxymethylfurfural (HMF) using **H-TA-CMP-ASO$_3$H**. Reproduced from Ref. 198 with permission of the Royal Society of Chemistry, copyright 2018.

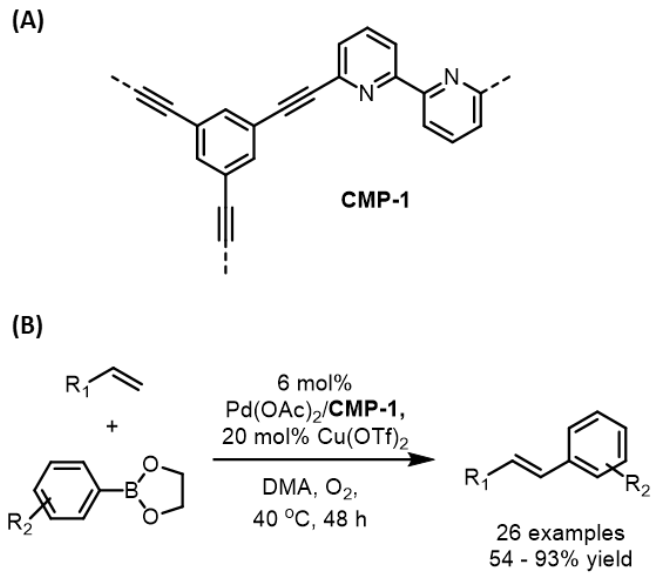

Fig. 57 (A) Synthesis of bipyridine based CMPs. (B) Reaction scheme for selective oxidative Heck reaction.[202]

was also applied to both the Suzuki-Miyuara and Heck couplings.[203] Oxidative Heck coupling has also been demonstrated using thiophene based CMPs prepared by Sonogashira-Hagihara coupling.[204] Analogous to the bipyridine based CMP discussed above, the porous structure and neighbouring thiophene heterocycle and C-C triple bond led to high linear selectivity.

CPPs with entrapped palladium have been applied as heterogeneous catalysts for the Suzuki-Miyuara cross coupling reaction.[205] The CPP support was were prepared by Sonogashira-Hagihara cross coupling utilising the toluene-in-water miniemulsion technique. The resultant micro- and mesoporous polymer were loaded with palladium nanocrystals. These materials demonstrated high yields (>85%) for the Suzuki-Miyuara coupling of phenylboronic acids with various aryl bromides/iodides, including simple phenyl derivatives, 2-bromonapthlene and 4-bromobenzophenone. The CPPs were highly efficient, with turnover frequencies as high as 44100 h^{-1} obtained. Minimal leaching of the palladium was observed, allowing the CPPs to be reused at least five times without significant loss in activity. Incorporation of palladium nanoparticles has also been achieved with a porphyrin-salen based CMP and successfully utilised as a catalyst in the Suzuki-Miyuara and Heck coupling reactions.[77] The porphyrin and salen building blocks present in the CMP provided a site for post synthetic attachment of Pd(II) ions that were then subsequently reduced using sodium borohydride to form the Pd-CMP composite. These Pd nanoparticles could then act as catalytic sites for both types of cross-coupling reactions using aryl iodides, bromides and even chlorides.

A porphyrin based CMP, **HP$_E$-CMP**, prepared by Sonogashira-Hagihara coupling have been applied as organophotocatalysts to the Knoevenagel condensation of malonitrile with a variety of aldehydes (Fig. 58).[206] The reactions proceeded with high yields (up to 99%) under ambient

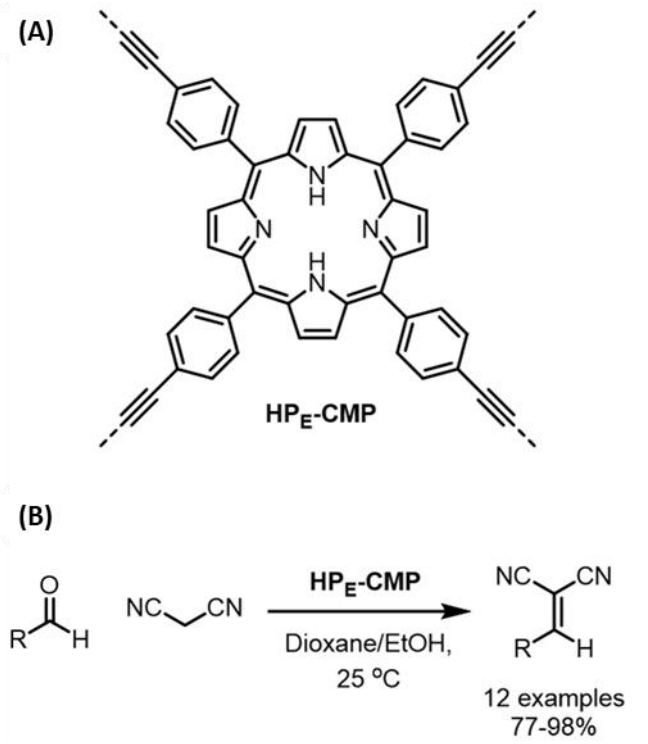

Fig. 58 (A) Structure of a porphyrin based CMP (**HP$_E$-CMP**). (B) The Knoevenagel condensation between malonitrile and various aldehydes catalysed by **HP$_E$-CMP**.[206]

conditions with the polymer capable of being used for 10 cycles without significant loss in activity.

2.2.3 Carbon Fixation As CO_2 represents the most environmentally abundant source of a C1 building block, developing methods for the chemical conversion of captured CO_2 into valued chemicals is a highly attractive. Several CMPs have also demonstrated similar application to capture and then convert stored CO_2 into cyclic carbonates. CMPs containing both salen-ligands and coordinated metals (including H, Cr, Zn, Al and Co) (Fig. 59A) have demonstrated both efficient uptake of CO_2 and subsequent coupling of CO_2 to epoxides to generate cyclic carbonates under mild conditions (Fig. 59B).[44,207,208] Depending upon the conditions used these polymers could obtain conversions as high as 99.1% with the polymers being usable more than ten times without significant loss in catalytic activity. In the case of the zinc-salen based CMP, turnover frequencies as high as 11 600 h^{-1} were obtained. Aluminium-porphyrin based CMPs have also demonstrated similar application to capture and convert CO_2 into cyclic carbonates (Fig. 60).[209] The polymer had a surface area of 839 m^2 g^{-1} and displayed a CO_2 uptake of 0.98 mmol g^{-1} at 273 K and 1 bar. A variety of reaction conditions were tested including temperature, pressure and cocatalyst. When using bis(triphenylphosphoranylidene)ammonium chloride as a co-catalyst, the CMP was able to achieve turnover frequencies of 364 h^{-1} and conversions as high as 91%.

2.2.4 Asymmetric Catalysis Kundu *et al*. have reported on the synthesis of CMPs that featured the (*R*)-BINOL group (Fig. 61A).[210] This polymer network was capable of catalysing various reactions (Fig. 61B-D) including the asymmetric hydrogenation of 3-phenyl-2*H*-1,4-benoxazine and various 2-arylquinolines at room temperature, with high conversions and enantiometric excess obtained (of the *S*- enantiomer). The CMP further demonstrated application as a chiral Brønsted acid for an aza-ene type reaction as well as Friedel-Crafts alkylation of pyrrole (Fig. 61B).

A series of cross-linked polymers based on the chiral binapthyl group have been prepared by $Co_2(CO)_8$ catalysed cyclotrimerisation of (*R*)-1,1'-bi-2-naphthol ((*R*)-BINOL) building blocks.[211] Following synthesis the material was treated with $Ti(^iOPr)_4$ to form titanium complexes (Fig. 62A). These materials acted as chiral Lewis acids for the asymmetric addition of diethylzinc to aldehydes with high conversion (94- >99%) and moderate to good (58 - 81%) enantioselectivity for the (*R*)-configuration obtained (Fig. 62B). Moreover, the material could be used for the same reaction up to 10 times without loss of conversion or selectivity.

3 CPPs as Sorbent Materials

The high surface areas and porous structures of CPPs make them ideal candidates for the adsorption of various species. This includes, for example, metal ions, organic molecules and even gaseous species such as carbon dioxide. Many factors influence the adsorptive properties of CPPs and these are highlighted within this section.

3.1 Adsorption of Metals

Metals present in the environment can pose a serious risk of damage to both human life and the wider ecosystem. Porous materials have demonstrated applications for removal of metals. With CPPs the ability to incorporate functional groups which can interact with the metals can lead to enhanced adsorption capacity. For example, a nitrogen-containing CMP,

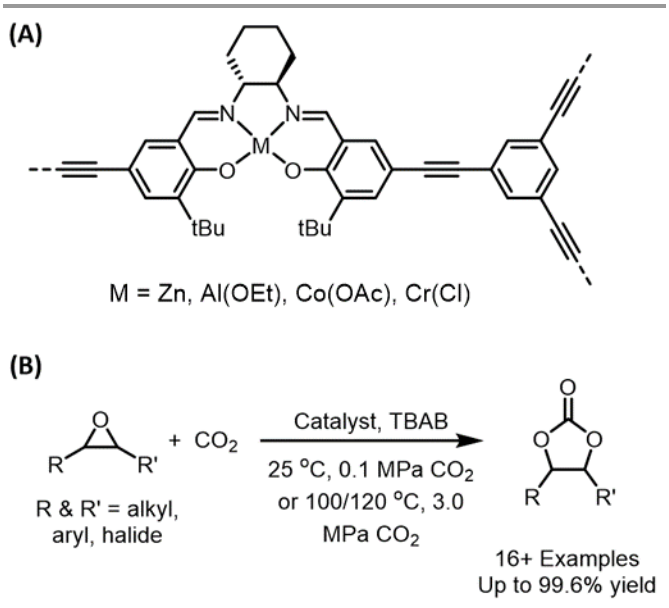

Fig. 59 (A) Structure of a generic salen containing CMPs. TBAB =Tetrabutylammonium bromide [44,207,208] Note catalyst refers to several metal-salen CMP catalysts.

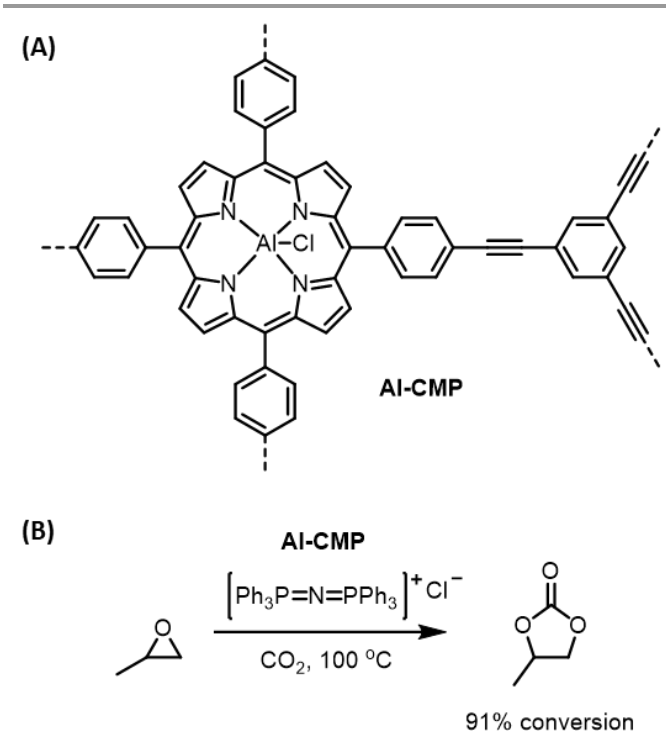

Fig. 60 (A) Structure of an aluminium-porphyrin based CMP, **Al-CMP**. (B) Reaction scheme for the conversion of epoxides into cyclic carbonates using CO_2. [209]

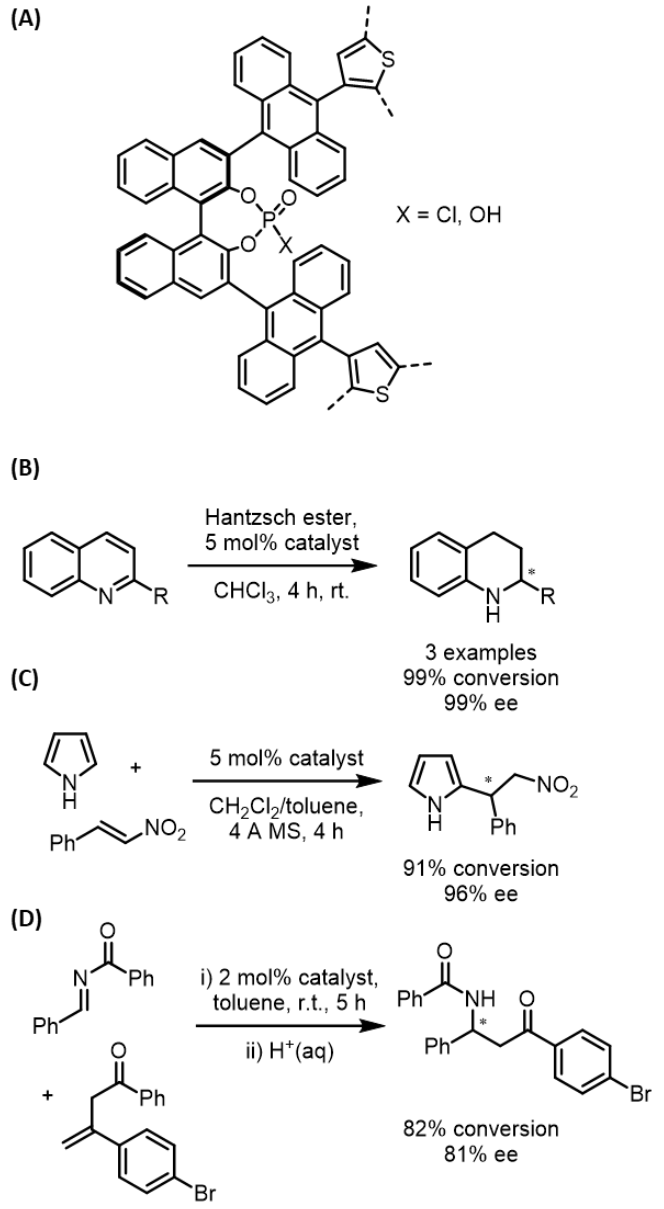

Fig. 61 (A) Structure of a (R)-BINOL derived polymer supported phosphoric acid with select examples of enantioselective chemical reactions including (B) asymmetric hydrogenation of 2-aryl quinolines, (C) asymmetric Friedel-Crafts alkylation of pyrrole and (D) an asymmetric aza-ene type reaction.[210]

NCMP, prepared from *bis*(4-bromophenyl)amine and 1,3,5-triethynylbenzene *via* Sonogashira-Hagihara coupling have demonstrated high adsorption capacities for metal ions (Fig. 63).[212] The resultant CPPs featuring amino- functional groups were able to adsorb Cr(VI), Zn(II) and Ni(II) from solution. The highest uptake was observed for Ni(II), at 384 mg g^{-1}, far greater than the 60 and 147 mg g^{-1} obtained for Cr(VI) and Zn(II) respectively. In addition, it was also demonstrated that the polymerisation solvent played a role in determining the pore morphology, which had a subsequent impact on ion uptake. For example, switching from toluene to 1,4-dioxane led to a decrease in the specific surface area from 945 to 593 m^2 g^{-1} and a subsequent decrease in the uptake of all ions.

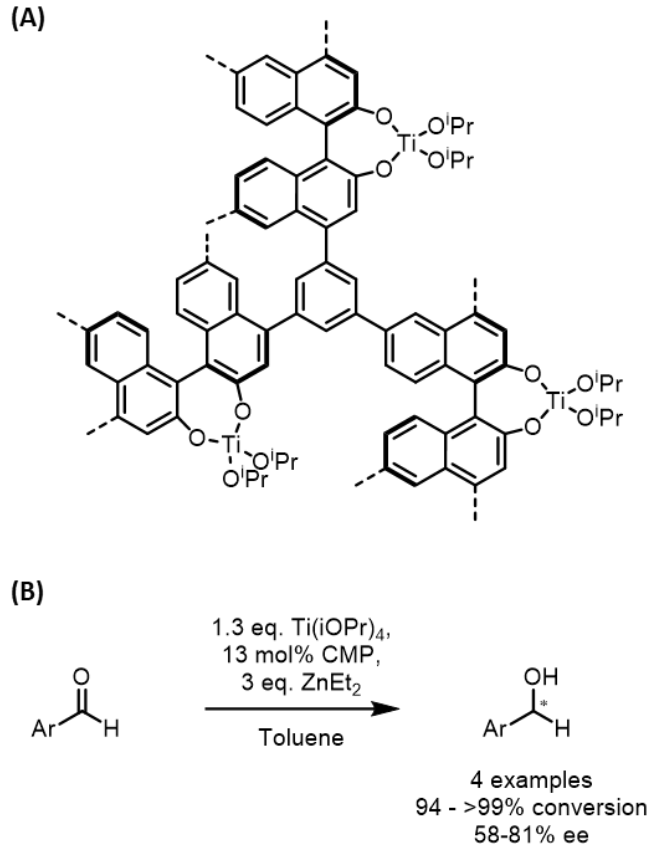

Fig. 62 (A) Example of a (R)-BINOL based CMP supporting $Ti(O^iPr)_4$ groups as chiral Lewis acids for the asymmetric addition of diethylzinc to aldehydes. (B) Scheme for the asymmetric reduction of ketones.[211]

Nitrogen containing CPPs have also been prepared from pyrazine and pyridazine derivatives (**BQCMP-1** and **DQCMP-1** respectively)(Fig. 64).[213] These materials also displayed uptake of Zn(II), Cr(VI) and Ni(II), with the latter again being superior.

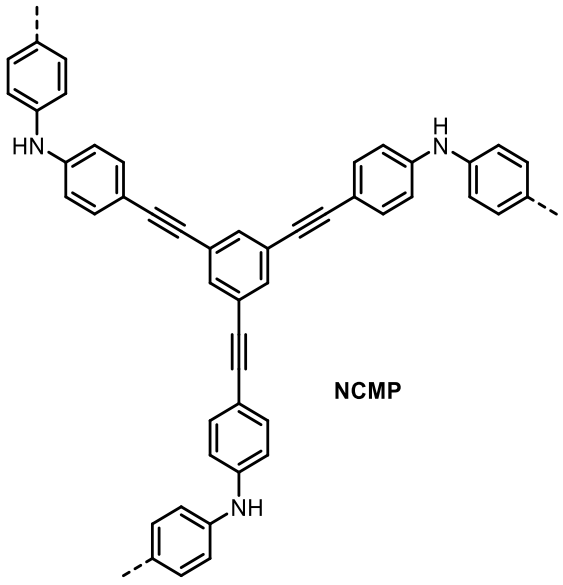

Fig. 63 Structure of the nitrogen containing **NCMP** for metal abstraction.[212]

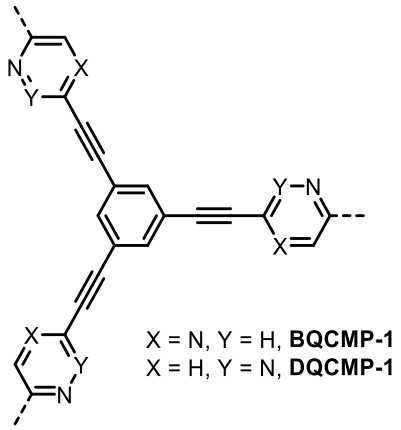

Fig. 64 Structures of pyrazine and pyridazine based CMPs **BQCMP-1** and **DQCMP-1**.[213]

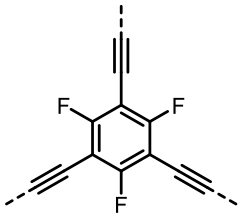

Fig. 65 Structure of a perfluorous CMP, **PFCMP-0**.[214]

Maximum uptake was observed for **DQCMP-1** at 559 mg g^{-1} of Ni(II) in comparison to 272 mg g^{-1} for the isomeric **BQCMP-1**.

High adsorption capacities for Pb(II) and As(V) ions present in water has been demonstrated by superhydrophobic perfluorous CMPs (Fig. 65).[214] The material demonstrated excellent uptake of Pb(II) and As(V) from aqueous solutions, with maximum capacities of 826.1 mg g^{-1} and 303.2 mg g^{-1}, respectively (measured by ICP emission spectroscopy). This was attributed to the porous nature of the material and non-covalent interactions between the extended π-system of **PFCMP-0** and the metal cations. In addition, the fluorine atoms present in **PFCMP-0** can serve as donor groups and due to their high electronegativity are capable of attracting the metal ions.[215,216] **PFCMP-0** displayed preferential adsorption of Pb(II) and As(V) ions over Ca(II), which had a maximum uptake of 110 mg g^{-1}. This is reflected in the relative binding energies of PFCMP-1 with Pb(II) and Ca(II): the authors calculated these as 45.02 and 1.97 kJ mol^{-1} respectively.

Abstraction of Pb(II) from water has been observed in nanoporous polymer frameworks that resembles graphene in design.[217] The polymer, **HOTT-HATN**, was assembled by the solvothermal metal-free reaction between building blocks **HATN-Cl$_6$** and **HOTT** (Fig. 66). It was demonstrated that the material was capable of rapidly removing Pb(II) ions from solution, with the Pb(II) content reduced to below the detection limit (15 – 20 ppb) within 5 minutes. This fast and efficient removal was attributed to the porous features and to the hydrophilicity of the oxygen and nitrogen heteroatoms that assisted permeation of water into the material. Pb(II) removal

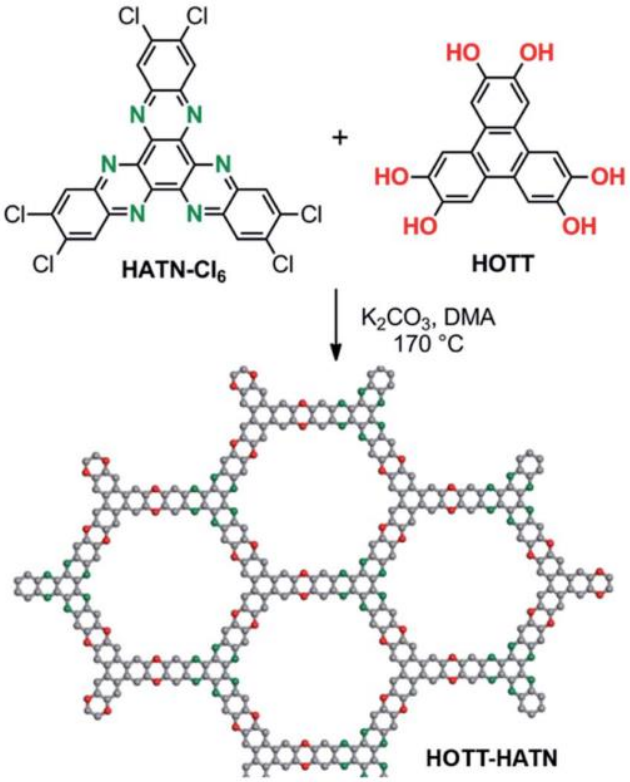

Fig. 66 Solvothermal synthesis of **HOTT-HATN** (shown in a ball in stick representation). Colour scheme: oxygen (red), carbon (grey), nitrogen (green), hydrogen omitted. Reproduced from Ref. 217 with permission from the Royal Society of Chemistry, copyright 2017.

using CPPs has been investigated by Zhu and coworkers, who were able to successfully prepare a CPP/PMMA composite that was used to coat the interior of a pipe.[218] By passing an aqueous solution of Pb(II) and other ions through this pipe, the authors were able to successfully reduce the concentration of Pb(II) to 15 ppm.

Selective uptake of Ag(I) ions has been observed in a monolithic CMP featuring thiomethyl groups introduced by post-synthetic thiol-yne chemistry (see **CMP_S**, Fig. 48A).[85] When a mixture of metal ions were stirred with the modified CMP, the concentration of most metals remained largely unchanged. However, the concentration of Ag(I), Cu(II) and Pb(II) decreased significantly. Among these, the largest decrease in concentration was observed for Ag(I) ions, with 95% removed after a period of 20 hours. This indicates selectivity over other metals, which would be useful for extracting precious silver from ores with other metals. In comparison, more than 50% of Ag(I) ions remained following the same time period when using the unmodified polymer, indicating that the sulfur groups significantly enhance Ag(I) uptake. This is further demonstrated by the maximum uptakes, which for the sulfur modified CMP was found to be 8.75% Ag content, in comparison to ca. 5.8% for the unmodified CMP.

Ko *et al*. have reported on a method to post-synthetically modify a CMP using OsO_4 chemistry (Fig. 67).[219] In the presence of OsO_4 and $NaClO_3$, alkyne groups present in **H-CMP** could be converted into dicarbonyl groups (**H-CMP-DC**). This conversion

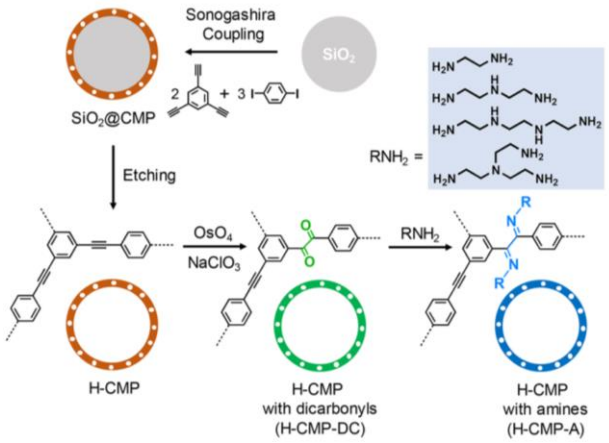

Fig. 67 Scheme for the conversion of **H-CMP** into **H-CMP-DC** using $NaClO_3$ and OsO_4 followed by conversion into **H-CMP-A** by reaction with amines. Reprinted with permission from Ref. 219. Copyright (2018) American Chemical Society.

from alkyne to dicarbonyl groups was accompanied by a slight increase in the Cr(VI) adsorbing ability of the CMP although much larger increase was observed upon attaching, various amines to the CMP framework by Schiff base chemistry (**H-CMP-As**). These tethered amino- groups led to up to 98% removal of Cr(VI) from solution with no appreciable drop in uptake observed over 5 uses.

The extraction of uranium under acidic and radioactive conditions has been reported by Hua and coworkers using an acetylcysteine functionalised CMP, **MCP** (Fig. 68).[72] The CMP was prepared by Sonogashira-Hagihara cross coupling followed by post synthetic modification via thiol-yne chemistry to install the acetylcysteine groups. The material exhibited rapid and selective adsorption of uranyl ions (UO_2^{2+}) with a capacity of 165 mg g^{-1} achieved within 40 s under acidic conditions. Furthermore, the CMP structure and UO_2^{2+} uptake were maintained even after irradiation doses of up to 200 kGy of γ-ray radiation in air or water. The sorption capacity was observed to be dependent on the pH levels: at low pH (1-3) the Coulombic repulsion between the UO_2^{2+} cation and the protonated framework reduced sorption while at higher pH (5-6) the UO_2^{2+} ions experienced Coulombic attraction to the deprotonated CMP that favoured adsorption.

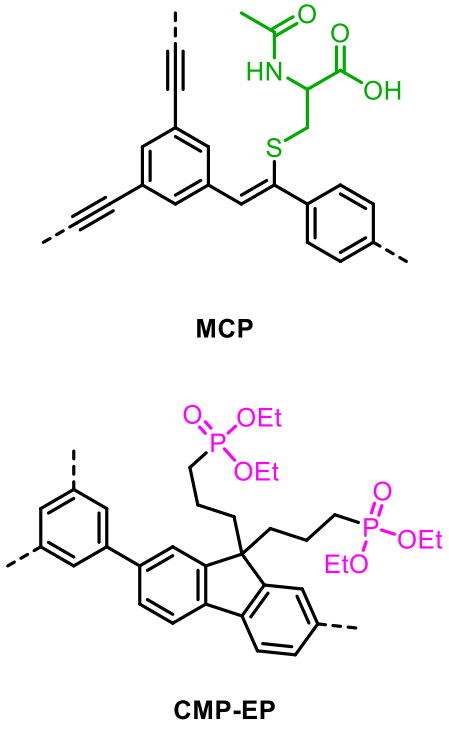

Fig. 68 Structures of CMPs for adsorption of the uranyl ion. The acetylcysteine group is highlighted in green and the phosphonate groups in pink. [71,72]

Hua and coworkers have also investigated extraction of uranium using CMPs bearing phosphonate groups (Fig. 68).[71] **CMP-EP** was prepared by Suzuki-Miyuara cross coupling, exhibited an adsorption capacity of UO_2^{2+} of 73 mg g^{-1} in 6 M nitric acid solutions, with good selectivity for the UO_2^{2+} from a mixture of metal ions simulating nuclear waste. The authors propose that the mechanism for removal involves uranyl ions forming $UO_2(NO_3)_2$ complexes which then bind to the phosphonate ligands. Impressively, the CMP was able to withstand a 1000 kGy dose of γ-ray radiation in a highly acidic environment with no change in structure or the efficiency of uranium uptake. In comparison, the authors remark upon how other materials studied for uranium extraction suffer from radiolysis and a decrease in adsorption capacity at high acid concentrations. Furthermore, the phosphonate groups, which are susceptible to radiolysis, are protected by the conjugated π-system, which provided a means to diffuse the energy.

Uptake of uranium has also been investigated by Zhu and coworkers, who utilised a molecular imprinting strategy to achieve selective uptake of UO_2^{2+}.[220] This involved synthesising a uranium complex with salicylaldoxime, methacrylic acid and 4-vinylpyridine ligands, the latter of which allowed the complex to be incorporated into a CMP via Heck coupling. Removing the UO_2^{2+} ion left vacant sites in the polymer network for binding of UO_2^{2+} ions. When the CMPs were applied to a simulated seawater mixture with 7.05 ppm UO_2^{2+} along with interfering ions (mainly Na^+ and K^+), an absorption of 35.44 mg g^{-1} and a selectivity constant for UO_2^{2+} over other ions of 171 was attained. The authors also demonstrated that the CMP could be use to fabricate composite PMMA coatings that also exhibited selective uptake of UO_2^{2+}.

3.2 Iodine Adsorption

While the generation of electricity from nuclear power is a viable alternative to fossil fuel combustion, the formation of volatile radioisotopes is a major issue that must be addressed. For example, ^{129}I has a very long half-life of 15.7 million years thus any environmental contamination would be persistent.[221] Although the ^{131}I isotope has a much shorter lifetime of just over 8 days, it is highly volatile, mutagenic and cytotoxic. The human body requires iodine for the production of hormones in the thyroid gland thus developing means to remove radioiodine from the environment in the event of contamination is highly important to safeguard people's health.[221–223] As a prospective material for iodine capture, CPPs have a number of advantages

over other materials. This includes control over factors such as pore volume and surface area, which have been demonstrated with other materials. Moreover, it has been reported that the π-system could result in a weak interaction between adsorbent and iodine, thus enhancing adsorption. Thus, CPPs and the diversity of π-building blocks available can lead to unique and often efficient iodine adsorbing materials.

CPPs containing based on the BODIPY moiety have demonstrated a high affinity for iodine molecules.[224] On the basis that the iodine adsorption was much lower in the BODIPY free **NBDP-CPP** (1500 mg g^{-1}) than for the BODIPY based **BDP-CPP-1** and **BDP-CPP-2** (2830 mg g^{-1} and 2230 mg g^{-1} respectively), the authors propose that the iodine experiences a higher affinity for BODIPY groups rather than benzene rings (Fig. 69). In particular, the availability of the 2 and 6- positions of the BODIPY core, which are known to be highly reactive with iodine, provide a chemical method for iodine removal from vapour and solution. The authors demonstrate that this is predominately a surface reaction but note that the large surface area of porous materials would expose a large quantity of the BODIPY groups. The authors also demonstrate that the active sites for iodination are mostly eliminated during the Sonogashira-Hagihara coupling via an oxidation reaction that further increased the degree of cross-linking.

Highly efficient iodine uptake has also been observed in a series of CMPs based on the hexaphenylbenzene unit and aryl diamine linkers (Fig. 70), with the amine groups on the CPP leading to uptakes as high as 336 wt%.[225] The authors attribute the high uptake values to the charge transfer interaction between the amino group of the CMP and the stored iodine, which existed in the form of polyiodide ions. This interaction is an example of a σ-hole bond, which is the noncovalent interaction between a volume of positive electrostatic potential on a covalently bonded electronegative atom (such as halogens) and a region of negative charge (e.g. the lone pair of Lewis bases

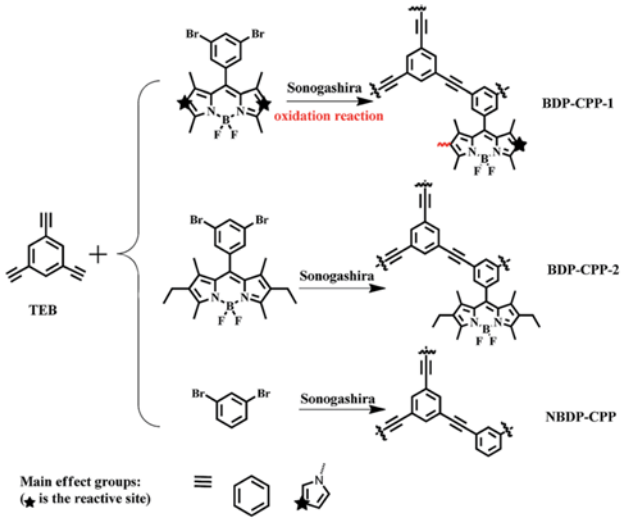

Fig. 69 Synthetic routes to prepare CPPs for iodine adsorption. Reaction conditions: $Pd(PPh_3)_4$, CuI, NEt_3, DMF, 100 °C. Reproduced from Ref. 224 with permission of the Royal Society of Chemistry, copyright 2017.

or an anion).[226] Calculations performed by Lommerse *et al*. have demonstrated that this interaction is mainly due to electrostatic effects but additional contributions from polarization, dispersion interactions and charge-transfer between the HOMO of the electronegative atom (e.g. nitrogen, oxygen, sulfur) and the LUMO of the C-X bond (where X is a halogen).[227] In the case of the CMPs, the σ-hole originates from the iodine being adsorbed while the nitrogen atoms of the polymer network act as the Lewis bases. Reducing the CPPs using anhydrous hydrazine led to an increase in the iodine uptake values, most likely due to additional amine groups that are able to participate in charge transfer interactions with the stored iodine. Further evidence of this charge transfer interaction has been observed in nitrogen-rich CMPs based on triazine and triphenylamine

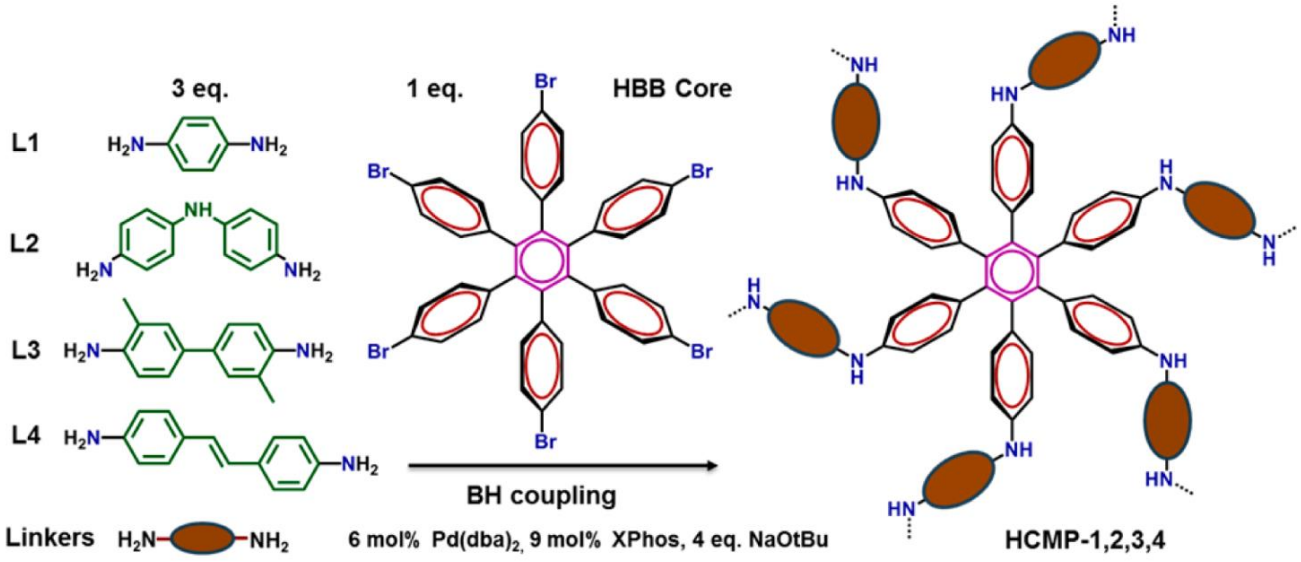

Fig. 70 Synthetic routes to iodine adsorbing CMPs via Buchwald-Hartwig coupling. Reprinted with permission from Ref. 225. Copyright (2016) American Chemical Society. Available under CC-BY.

units.[228] A maximum uptake value of iodine vapour of 4.43 g g^{-1} was achieved, which was attributed to the strong interactions between iodine and CMPs arising from the π-conjugated system and the nitrogen heteroatoms.

Efficient capture of iodine has been achieved using CPPs containing thiophene groups. Ren *et al*. have reported on CMPs that were able to attain equilibrium uptake of iodine vapour of 345 wt%.[229] The materials were also capable of sequestering iodine in cyclohexane solutions of around 60%. Similarly high iodine uptake in thiophene based CMPs has also been reported by Qian et al.[230] These materials were capable of vapour uptakes as high as 222 wt% and solution adsorption as high as 73.6% were obtained. In both cases, the high uptakes were attributed to the π-system of the CMP and the electron-rich thiophene building blocks, analogous behaviour to the nitrogen based heterocycles discussed above.

Xie *et al*. have reported on a nickel porphyrin based CMP that displays good uptake of iodine from both vapour and solution up to values of 202 wt% and 326 mg g^{-1} respectively.[231] Application of photoelectron spectroscopy to the CMP elucidated that the adsorbed iodine existed as I_2 and not as other chemical species. It was proposed that the reason for the high uptake was due to weak interactions between the π-electron framework and iodine.

3.3 Organic Molecule Adsorption

Many different organic compounds can be found as environmental contaminants, commonly in water. This includes solvents, pesticides, fertilisers, oils, pharmaceuticals, aromatic hydrocarbons and dyes, either dissolved in water or remaining as colloids or suspensions.[232] These pollutants originate from multiple sources, with, for example, dyes originating from the textile industry, and solvents from chemical production and research.

One common contaminant found in water are phenolic compounds. These are toxic even when found in low concentrations and developing materials that are able to remove them is therefore important. For example, CMPs based on phenylene units have been used as a coating for stainless steel fibres (Fig. 71).[233] This process involved etching the stainless steel wire in hydrofluoric acid followed by washing and drying. The wire was then dipped in epoxy resin and coated with **PPc-CMP**. These **PPc-CMP** coated fibres displayed efficient and rapid removal of phenolic compounds. A similar concept has also been explored by Jiao *et al*., who have coated plain paper, stainless steel mesh and cotton thread with pyridine based CMPs.[234] Coating these objects with CMPs rendered them superhydrobic and oleophilic, with the CMPs exhibiting uptakes of various oils as high as 3280 wt%. The authors also demonstrated that coating the CMP coated cotton threads had potential application in a fabricated continuous oil/water separator.

Li *et al*. have demonstrated CPPs with superhydrophobic surfaces with good adsorption of both oils and organic solvents in the region of 600 – 2300 wt% (Fig. 72A).[235] This included adsorption of toxic solvents such as *o*-dichlorobenzene, nitrobenzene and phenol. The superhydrophobicity was attributed to two effects: the aromatic chemical composition and the microporous morphology adopted by the CPP. The contact angles on surfaces coated with the CPPs were measured to be above 157° (Fig. 72B) for water and almost 0° for diesel oil (Fig. 72C). It was also demonstrated that these CPPs could be immobilised onto the surface of porous sponge materials, changing the sponge from hydrophilic to both hydrophobic and

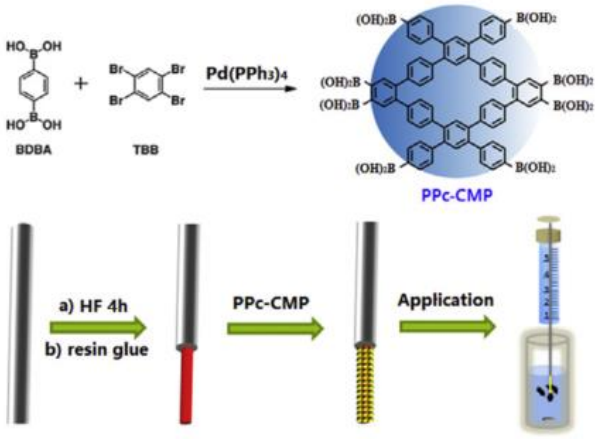

Fig. 71 Summary of the route to preparing CPP coating stainless steel fibres. Reproduced from Ref. 233 with permission of Elsevier, copyright 2018.

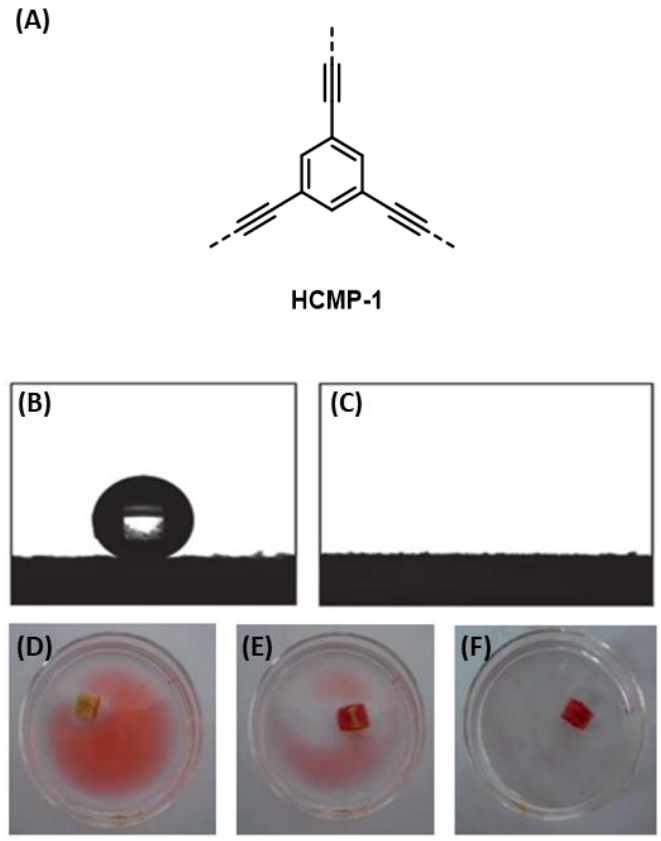

Fig. 72 (A) Structure of **HCMP-1**. Contact angle measuring experiments with water (B) and diesel oil (C) for a **HCMP-1**. Removal of octane film (coloured with red oil o) on water by a piece of sponge treated with hydrophobic CMP (D-F). Reproduced from Ref. 235 with permission of the Royal Society of Chemistry, copyright 2011.

oleophilic. These CPP treated sponges displayed high absorption of solvents such as 2300 wt% for octane and 3300 wt% for nitrobenzene (Fig. 72D-F). Subsequent studies by Tan *et al*. demonstrated that the CPP morphology had an impact on the solvent adsorption ability and was controlled by factors such as monomer structure,[236] pore volume[237] and polymerisation solvent.[238] Computational measurements have also been employed to probe the effect of varying the length of linker and introducing substituent groups on the physisorption of organic molecules.[239]

In addition to coating sponges, as well as other objects, with CPPs as discussed above, the synthesis of monolithic sponges made from CPP has also been reported (Fig. 73A).[240] The fabricated sponges were exhibited reversible compressibility with little change in the compressive stress-strain curves after 10 cycles, indicating high mechanical stability (Fig. 73B). In addition, these sponges exhibit high adsorption capacities for various solvents including straight chain alkanes, oils and chlorinated solvents. The adsorption capacity was observed to correlate linearly with the adsorbate density, with the maximum uptake in excess of 1600 wt% observed for chloroform.

Exceptionally high adsorption of solvents has been reported in CMP gels.[241] The CMP was prepared by utilising Glaser coupling and then gels obtained by either freeze-drying with water as the solvent or vacuum drying. The different methods used in preparing the gels led to organogels with different properties (Fig. 74). Vacuum drying led to the formation of xerogels with a collapsed pore structure and a specific surface area of 1085 $m^2 g^{-1}$. Utilising freeze-drying led to the formation of meso- and macropores following sublimation of the solvent. The hierarchically porous aerogel obtained has an open 3D structure and a surface area of 1701 $m^2 g^{-1}$. This CMP aerogel demonstrated adsorption capacities towards various solvents and oils with uptakes ranging from 2000 wt%, up to a maximum of 5300 wt% for nitrobenzene. The same group later investigated the use of fluorosurfactants during the preparation of CMP based aerogels by Glaser coupling. The fluorosurfactant (*N*-ethanol perfluorooctyl sulfonamide) played many roles including influencing the pore structure, increasing the hydrophobicity of the material and controlling the gelation process (by ensuring a homogeneous dissolved oxygen concentration), resulting in materials with oil adsorption properies.[242]

Organic solvent adsorption has also been observed in superhydrophobic CPPs based on ferric porphyrin complexes.[243] These displayed highly efficient separation of water/oil mixtures and adsorption of benzene, toluene and chlorobenzene, which are common toxic water pollutants. The CPPs were used to coat both a stainless-steel mesh and a porous sponge. Hydrophobic porphyrin based CPPs have also demonstrated excellent uptake of saturated hydrocarbons and gasoline in both the vapour (up to 1030 mg g^{-1}) and in the liquid phase (up to 25.9 g g^{-1}).[244]

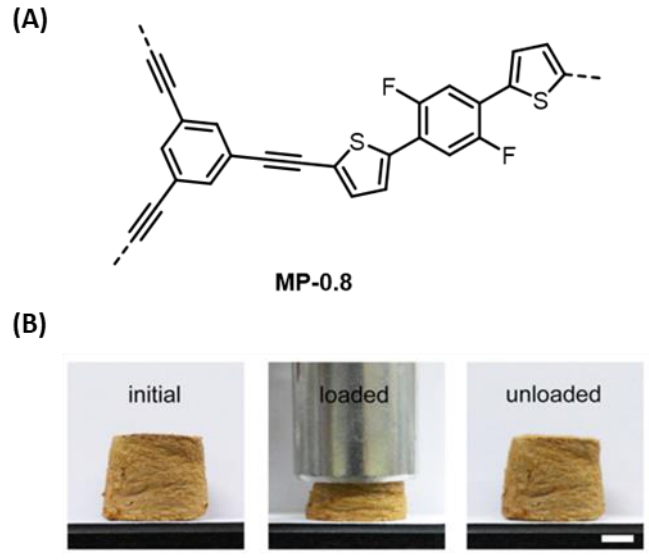

Fig. 73 (A) Structure of **MP-0.8**. (B) Images of **MP-0.8** sponge before (left), during (center) and after (right) compression (scale bar = 5 mm). Adapted from 240 with permission from Springer Nature, copyright 2015. Available under CC-BY-4.0.

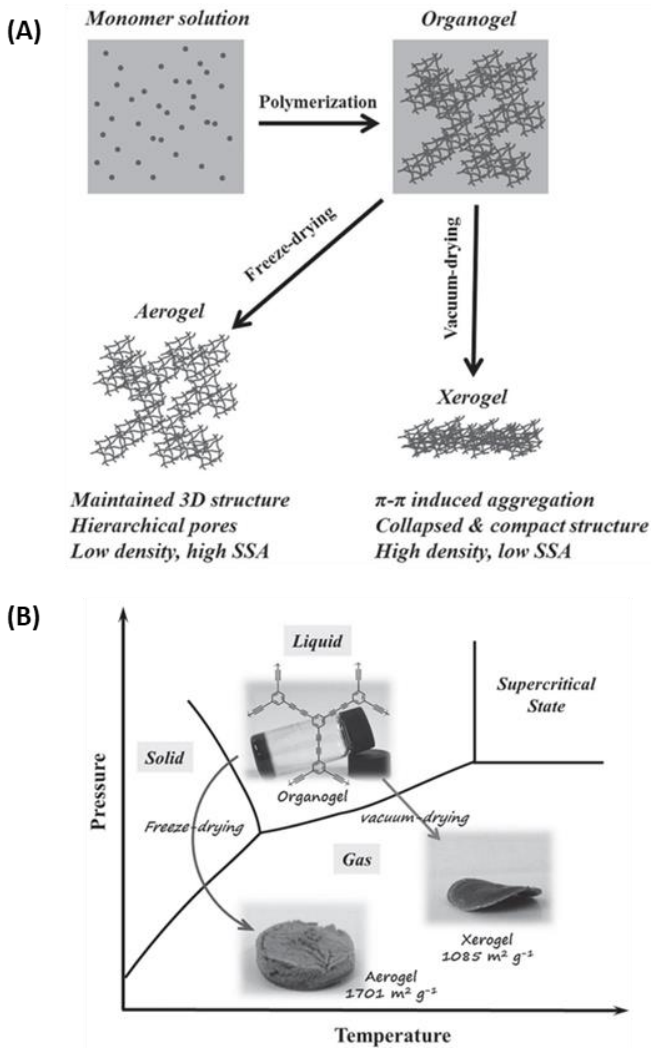

Fig. 74 (A) Illustration of the preparation of PTEB aerogel and xerogel. (B) Summary of the routes across phase diagram boundaries to obtain aerogels and xerogels from organogel. Reproduced from Ref. 241 with permission of Wiley-VCH, copyright 2014.

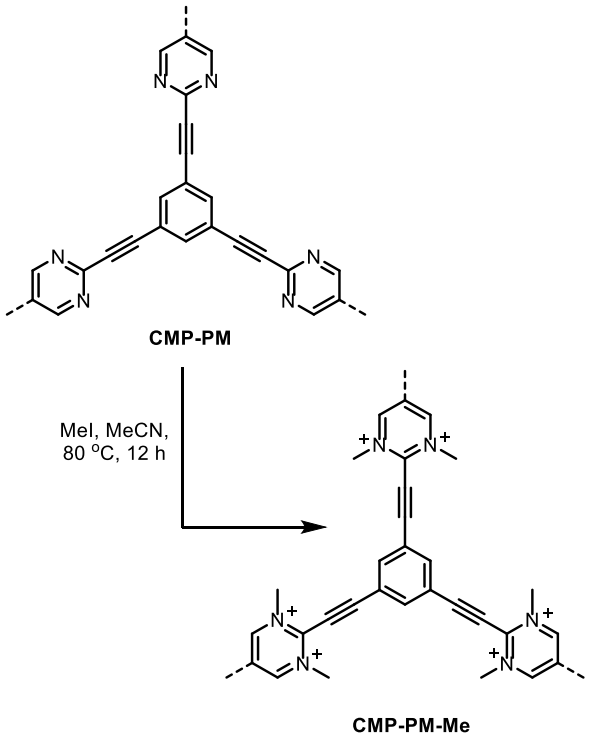

Fig. 75 Structure of **CMP-PM** and post-synthetic *N*-methylation to yield the cationic polymer **CMP-PM-Me**.[245]

CPPs bearing cationic charges have displayed excellent ability to remove anionic dyes from solution.[245] The neutral CPPs were first prepared via Sonogashira-Hagihara coupling of 1,3,5-triethynylbenzene with dibromopyrimidine, with a subsequent post-synthetic reaction using methyl iodide leading to *N*-methylated CPPs (Fig. 75). The presence of charges on the CPP skeleton increased the efficiency of adsorption of the monoanionic dye methyl orange and the dianionic dye Congo red. For example, post synthetic methylation of **CMP-PM** increased the adsorption of Congo red from 344.8 mg g^{-1} to 400 mg g^{-1}. These charges also resulted in the CPP being able to preferentially adsorb these anionic dyes from binary mixtures with neutral dyes due to the Coulombic interactions. Similarly Wang *et al*. have reported that sulfonation of CPP led to enhanced interactions with cationic or neutral dyes (rhodamine B and methylene blue) but reduced interaction with the anionic dye acid orange.[246]

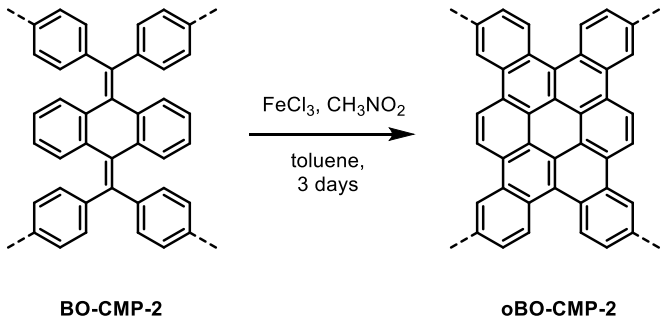

Fig. 76 Extending π-conjugation by $FeCl_3$ catalysed oxidation, exemplified by transforming **BO-CMP-2** into **oBO-CMP-2**.[247]

Yang *et al*. have reported on CMPs with extended π-systems for the adsorption of organic vapours.[247] The CMPs formed via Suzuki-Miyuara cross coupling featured benzoquinone moieties, which were transformed into tetrabenzocoronene groups as part of a post synthesis oxidation process using ferric chloride (Fig. 76), which extended the π-structure of the CMPs. These materials displayed high uptake of benzene and toluene, which the authors suggest is due to the affinity of the aromatic molecules for the π-system. In comparison, the CMPs exhibited lower adsorption of cyclohexane due to the lack of π-electrons.

Zhou *et al*. have demonstrated that CMPs with built-in Fe_3O_4 nanoparticles can be used to extract hydroxylated polycyclic aromatic hydrocarbons (PAHs) from human urine.[248] These Fe_3O_4 nanoparticles were incorporated during the synthesis of the CMP by copolymerising the building blocks with phenylboronic acid modified Fe_3O_4 nanoparticles, leading the CMPs to exhibit rapid magnetic response. By adsorbing hydroxylated PAH using the CMPs followed by magnetic recovery and washing with solvent, Zhou *et al.* were able to extract trace analytes present in human urine with recoveries greater than 76.0%. This was then coupled with high performance liquid chromatography to analyse the hydroxylated PAH content of samples from smokers and non-smokers. Similar strategies involving the extraction of analytes using CMPs have also been utilised to analyse samples of antibiotics,[249] volatile organic acids in tobacco,[250] herbicides and bactericides for analysis.[251,252]

Wang *et al*. have reported on the application of BTZ containing CMPs to the adsorption of the antibiotic tetracycline (see CMP in Fig. 8).[253] Adsorption isotherms indicates a maximum adsorption of 26.67 mg g^{-1}, which was noted to be comparable to other tetracycline adsorption values. The authors suggest that π-π stacking between tetracycline and the CMP π-system is mainly responsible for adsorption. Liu *et al*. have reported that metalloporphyrin based CMPs exhibited efficient uptake of a variety of amines (up to a maximum value of 6.9 g g^{-1}), as both vapour and liquid.[254]

Adsorption of antibiotics has also been studied by Zhu and coworkers using a series of CMPs with structurally similar skeletons decorated with different functional groups (Fig. 77A).[255] This allowed the polarity of the pores to be tuned to maximise adsorption of the antibiotics tetracycline (TC) and doxycycline hydrochloride (DOX) (Fig. 77B and C). Both of these have polar groups but the latter is a hydrochloride salt. **PAF-79** has no polar groups and thus exhibited low uptake of TC and DOX (25 mg g^{-1} and 62.54 mg g^{-1}) respectively, despite possessing the highest surface area of the CMP series (1964 m^2 g^{-1}). The introduction of hydroxyl- and sulfonate groups into the structures of **PAF-80** and **PAF-80-SO_3H** increased the polarity of pores and increased the adsorption of both TC and DOX. Due to electrostatic interactions, more of the ionic DOX was adsorbed by **PAF-80-SO_3H** (142.86 mg g^{-1}) compared to **PAF-80** (125 mg g^{-1}). However, higher uptake of TC was observed in **PAF-80** (111.11 mg g^{-1}) over **PAF-80-SO_3H** (90.91 mg g^{-1}): this was attributed to the neutral TC molecules preferring moderately

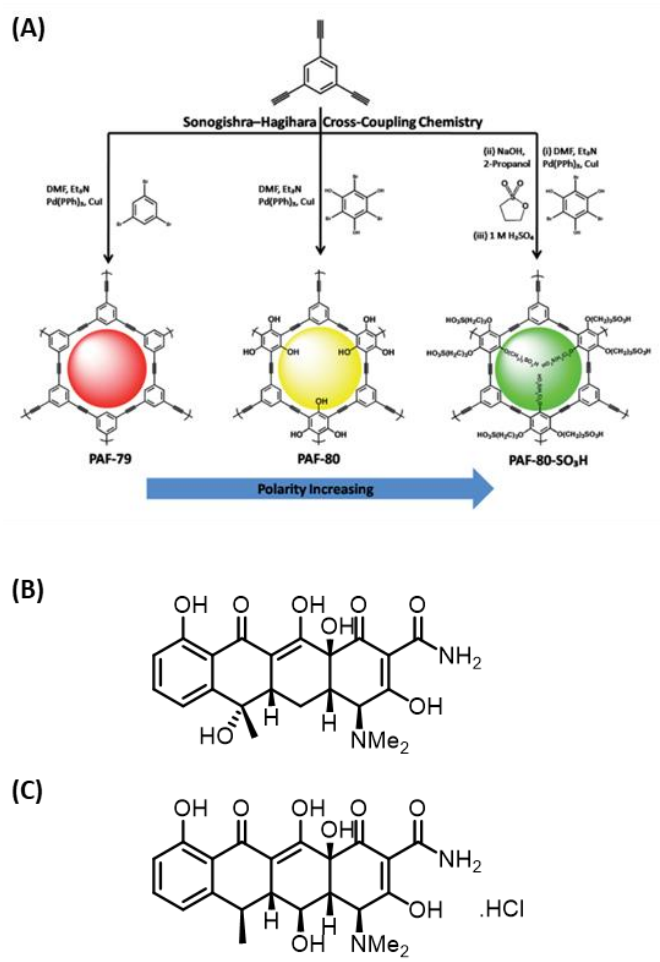

Fig. 77 (A) Synthesis and structure of CPPs bearing different surface functional groups (**PAF-79**, **PAF-80** and **PAF-80-SO_3H**). (B) Structure of tetracycline (TC). (C) Structure of doxycycline hydrochloride (DOX). Adapted from Ref. 255 with permission from the Royal Society of Chemistry, copyright 2019.

polar channels with a higher surface area (768 $m^2 g^{-1}$ for **PAF-80** over 200 $m^2 g^{-1}$ for **PAF-80-SO_3H**). The change in the polarity also influenced the water adsorption capacity, indicating the increase in the surface wettability as the polarity of the pores increased. Other work by Zhu and coworkers have further demonstrated the utility of CMP towards the removal of pharmaceuticals from water.[256] Using CMPs grown onto poly(acrylonitrile)/poly(aniline) fibres, the authors were able to adsorb ibuprofen, chloroxylenol and *N*,*N*-diethyl-*meta*-toluamide with capacities of 116.27 – 117.49 mg g^{-1} respectively.

3.4 Adsorption of Gases

3.4.1 Carbon Dioxide Widespread fossil fuel usage has seen global atmospheric CO_2 levels increase exponentially in recent years, a trend considered to be one of the primary driving forces behind global climate change.[257] Therefore, developing methods for the capture of CO_2 that are both economic and energetically feasible is highly important. Current methods for post combustion CO_2 separation mainly rely on liquid amine scrubbing, where aqueous solutions of amines are used to capture CO_2.[258] However, these can be corrosive and energy is required to regenerate the amines for reuse. An alternative to this method is gas sorption using porous materials including porous carbons, zeolites, MOFs and porous organic polymers.[259–264]

Given their porous nature, high surface areas and innate physicochemical stability CPPs are promising candidates for adsorption of CO_2.[265] CPPs capture CO_2 by physisorbing CO_2 molecules onto the surface of the material via van der Waals interactions. These weak forces are easy to break, making regeneration of the material much simpler in comparison to amine scrubbing. However, it has been noted that the lack of crystallinity in amorphous POPs could hinder access of CO_2 to binding sites.[266]As the literature on CO_2 capture using CPPs is extensive, we have chosen to summarise the information in table 1 and instead use this section to focus on some examples of how the structure of CPPs can be adapted to improve CO_2 adsorption capacity. The structures associated with all CPP listed in table 1 (as well as table 2 and 3 below) have been provided in the ESI. Various units can be used to express CO_2 adsorption potential, in terms of amount of CO_2 adsorbed relative to the mass of adsorbent. These include mmol g^{-1}, cm^3 g^{-1}, mg g^{-1} or wt%. However, in order to simplify comparison between different reports we have converted all of the values from their reported units into mmol g^{-1}.

While porosity engineering can influence the CO_2 capturing ability of a CPP, making materials with very high surface areas is not the only structural parameter that can be manipulated. As CO_2 possesses a high quadrupole moment and polarisability, the presence of polar groups or heteroatoms on a porous material enhances interaction with CO_2 molecules and promotes adsorption.[267] This is an advantage of using CPPs for CO_2 capture as the array of building blocks available allows for facile integration of these moieties into the design process.

For example, a series of functionalised CPPs prepared via Sonogashira-Hagihara coupling demonstrated isoteric heats of CO_2 adsorption that were dependent on the functional groups attached to the polymer framework (Fig. 78).[268] Dawson *et al.* demonstrated that the incorporation of polar groups such as carboxylic acids, hydroxy- or amino-groups led to an increase in the CO_2 adsorption over the unmodified **CMP-1**. On the contrary, the introduction of non-polar methyl groups in **CMP-1-$(CH_3)_2$** decreased the isoteric heat of adsorption, despite **CMP-1-$(CH_3)_2$** having a higher BET surface area than both **CMP-**

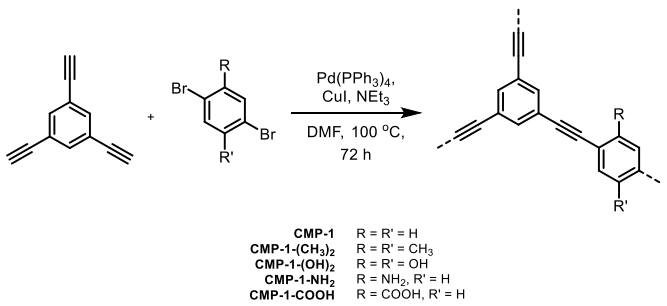

Fig. 78 Synthetic scheme for CMPs featuring different functional groups.[268]

Table 1 Summary of the CO_2 adsorption capacity data of various CPPs. To simplify comparison, these data have been converted into units of mmol g^{-1}.

Entry	Material	$SA_{BET}/m^2\ g^{-1}$	Temperature/K	Pressure/bar	Adsorption Capacity/mmol g^{-1}	Reference
1	Py-azo-COP	700	273	1	1.93	34
				15.5	4.14	
2	Zn-CMP	791	298	1.01	1.33	44
3	CMP1	258	298	1	0.46	53
	CMP2	567			0.67	
4	NWPTPE	508	298	1	0.68	54
	NWPPYR	824			0.93	
5	HCTPP	582	273	1	2.79	57
	HCTPA	921			2.27	
	HCTPM	670			2.14	
6	TCMP-0	963	273	1	2.38	79
			298		1.34	
	CMP-0	1018	273		2.10	
			298		1.21	
	TNCMP-2	995	273		2.62	
			298		1.45	
	TCMP-3	691	273		2.25	
			298		1.26	
	TCMP-5	494	273		1.22	
			298		0.68	
7	TPB-BD-CMP	657	273	1	2.51	81
	TPA-BD-CMP	543			2.94	
	TPM-BD-CMP	1008			3.78	
	SPF-BD-CMP	833			3.25	
8	P1	914	273	1	3.01	86
	P2	834			2.53	
	P3	873			2.12	
9	ACMP-C	629	195	1.06	11.4	87
			273		1.56	
			298		1.08	
	ACMP-C6	380	195		9.97	
			273		0.79	
			298		0.54	
	ACMP-N	46	195		11.5	
			273		1.16	
			298		0.79	
10	CMP1	767	273	1	2.94	96
	CMP2	624			2.67	
	CMP3	780			2.37	
11	CMP-1-NH2	656	273	1	1.65	104
			298		0.96	
	CMP-1-AMD1	316	273		1.51	
			298		0.96	
	CMP-1-AMD2	264	273		1.46	
			298		0.92	
	CMP-1-AMD3	119	273		1.31	
			298		0.83	
	CMP-1-AMD4	59	273		1.13	
			298		0.71	
	CMP-1-AMD5	37	273		1.10	
			298		0.64	
	CMP-1-AMD9	68	273		0.87	
			298		0.54	
12	PP_CMP@mmm	1928	273	1	2.52	110
			298		1.36	
	PP_CMP@omp	43	273		0.82	
			298		0.43	

Table 1 (continued)

Entry	Material	$SA_{BET}/m^2 g^{-1}$	Temperature/K	Pressure/bar	Adsorption Capacity/mmol g^{-1}	Reference
12 (continued)	PP_CMP@omom	81	273	1	1.05	110
			298		0.66	
13	Py-BF-CMP	1306	273	1	3.21	154
	TPE-BF-CMP	777	273		2.10	
	TPA-BF-CMP	590	273		1.83	
14	HP_E-CMP	662	273	1	3.58	206
			298		1.70	
15	CMP	772	298	1.01	1.61	207
	Co-CMP	965			1.80	
	Al-CMP	798			1.74	
16	Cr-CMP	738	298	1.01	1.63	208
17	Al-CMP	839	273	1.01	0.98	209
			298		0.62	
18	NCMP-I	945	273	1	1.93	212
			298		1.43	
	NCMP-III	593	273		0.95	
			298		0.50	
19	BQCMP-1	422	273	1	1.55	213
			298		1.06	
	DQCMP-1	123	273		1.09	
			298		0.86	
20	HCMP-1	308	273	1	1.70	225
	HCMP-2	58	273		1.23	
	HCMP-3	50	273		1.16	
	HCMP-4	28	273		0.98	
21	PTEB Aerogel	1701	273	1	3.47	241
22	CMP-PM	416	273	1.01	1.99	245
	CMP-PM-Me	241			1.42	
23	BO-CMP-1	440	273	1	1.80	247
	BO-CMP-2	1030			2.41	
	oBO-CMP-1	390			1.16	
	oBO-CMP-2	540			1.70	
24	CMP-1	837	298	1	1.18	268
	CMP-1-$(CH_3)_2$	899			0.94	
	CMP-1-$(OH)_2$	1043			1.07	
25	BFCMP-1	1316	273	1.13	2.45	269
			298		1.39	
	BFCMP-2	1470	273		2.77	
			298		1.64	
26	PPTBC	917	273	1.13	2.93	270
			298		1.71	
	PMTBC	704	273		2.86	
			298		1.79	
	PPETBC	702	273		2.23	
			298		1.25	
	PMETBC	540	273		1.96	
			298		1.09	
27	MFCMP-1	840	273	1	3.69	271
28	CMP-YA	1410	273	1	1.25	272
			298		1.90	
	CMP-SO-1B2	1085	273		1.19	
			298		1.92	
	CMP-SO-1B3	1080	273		1.22	
			298		1.89	
29	CK-COP-1	54	273	1	0.65	273
	CK-COP-2	615			2.21	
30	ThPOP-1	1050	273	1	3.41	274
	ThPOP-2	160			0.91	
31	Porp-TPE	547	273	1.05	2.09	275

Table 1 (continued)

Entry	Material	$SA_{BET}/m^2 g^{-1}$	Temperature/K	Pressure/bar	Adsorption Capacity/mmol g^{-1}	Reference
31 (continued)	Porp-Py-CMP	31	273	1.05	1.29	275
32	Por-Py-CMP	1014	273	1	3.00	276
			298		1.86	
33	DA-CMP1	662	273	1.13	2.28	277
			298		1.35	
	DA-CMP2	603	273		1.64	
			298		0.95	
	Azo-CMP1	1146	273		3.72	
			298		2.15	
	Azo-CMP2	898	273		3.17	
			298		1.96	
34	SCMP-COOH@1	911	298	1	1.39	278
	SCMP-COOH@2	622			1.07	
	SCMP-COOH@3	820			1.25	
35	ZnP-5N3-CMPs	711	273	1	1.00	279
			298		0.59	
	ZnP-25N3-CMPs	685	273		1.23	
			298		0.70	
	ZnP-50N3-CMPs	654	273		1.98	
			298		1.11	
	ZnP-75N3-CMPs	565	273		1.64	
			298		0.98	
	ZnP-100N3-CMPs	477	273		1.57	
			298		0.91	
	ZnP-5F-CMPs	430	273		1.32	
			298		0.77	
	ZnP-25F-CMPs	352	273		1.91	
			298		1.18	
	ZnP-50F-CMPs	240	273		2.95	
			298		2.04	
36	PCZN-1	1003	273	1	2.57	280
	PCZN-2	607			2.36	
	PCZN-3	714			2.54	
	PCZN-4	374			2.02	
	PCZN-5	707			2.29	
	PCZN-6	718			2.82	
	PCZN-7	1058			2.91	
	PCZN-8	1126			3.18	
	PCZN-9	690			2.93	
	PCZN-10	391			1.70	
37	PCTF-8	625	273	1	2.47	281
			293		1.41	
38	BCMP3	950	273	1	2.41	282
			298		1.61	
39	LKK-CMP-1	467	273	1	2.22	283
			298		1.38	
40	PCTF-1	2235	273	1	3.22	284
			293		1.84	
	PCTF-2	784	273		1.82	
			293		0.99	
41	CPOP-8	1610	273	1	3.75	285
	CPOP-9	2440			4.13	
	CPOP-10	1110			3.36	
42	PTA-1	52	273	1	0.84	286
	PTA-2	62	273		1.25	
			303		0.59	
	PTA-3	450	273		1.48	
			303		0.77	
43	BILP-101	536	298	1	2.43	287

Table 1 (continued)

Entry	Material	$SA_{BET}/m^2 g^{-1}$	Temperature/K	Pressure/bar	Adsorption Capacity/mmol g^{-1}	Reference
44	PAF-33	821	273	1	2.16	288
			298		1.25	
	PAF-33-NH_2	370	273		1.19	
			298		0.75	
	PAF-33-COOH	445	273		1.94	
			298		1.21	
	PAF-34	953	273		2.50	
			298		1.39	
	PAF-34-OH	771	273		2.21	
			298		1.25	
	PAF-35	567	273		1.77	
			298		1.01	
45	Cu/BF_4/BIPLPL-1	380	273	1	2.57	289
46	BILP-15	448	273	1	2.68	290
			298		1.82	
	BILP-16	435	273		2.70	
			298		1.83	
	BILP-15(AC)	862	273		3.43	
			298		2.29	
	BILP-16(AC)	843	273		3.46	
			298		2.32	
47	TBILP-1	117	273	1	2.91	291
			298		1.98	
48	BILP-10	787	273	1	4.02	292
			298		2.52	
	BILP-11	658	273		3.09	
			298		2.00	
	BILP-13	677	273		2.57	
			298		1.80	
49	NPOF-1	2062	298	1	1.52	293
	NPOF-1-NO_2	1295			2.52	
	NPOF-1- NO_2(xs)	749			2.00	
	NPOF-1- NH_2	1535			3.77	
	NPOF-1-NH_2(xs)	1074			2.93	
50	ALP-5	801	273	1	4.46	294
			298		2.94	
	ALP-6	698	273		3.42	
			298		2.17	
	ALP-7	412	273		2.50	
			298		1.55	
	ALP-8	517	273		3.05	
			298		1.97	

1-NH_2 and **CMP-1-COOH**.

An alternative method to introducing substituent groups onto the framework is to incorporate heteroatoms into the makeup of the material itself. Nitrogen, sulfur and oxygen atoms either in heterocycles or as part of linking groups between groups possess lone pairs of electrons that can lead to dipole-quadrupole interactions between CO_2 molecules and the pore walls. For example, Ren *et al*. have demonstrated that these effects could be attained by substituting benzene groups for triazine groups.[79] Although the triazine based CMPs possessed BET surfaces areas similar to the corresponding benzene CMPs, they demonstrated better uptake of CO_2. High uptake of CO_2 has been observed in a series of nitrogen containing CPPs based on carbazole,[270] carbazole/triazine,[271] *N*,*N*'-bicarbazole,[272] and benzimidazole.[287]

Efficient uptake of CO_2 has also been observed in thiophene based CPPs. Microporous covalent organic polymers with a pyrene core have been prepared utilising a $FeCl_3$ catalysed oxidative polymerisation of thiophene groups.[273] Differences in the uptake of nitrogen at low temperatures indicated that structural isomerism in the building blocks led to differences in the packing of the polymer (Fig. 79). With the polymer CK-POP-1, the degree of cross-linking between building blocks was much lower than in **CK-POP-2**, which can cross-link through both the 2- and 5- thiophene positions. This is reflected in the apparent surface areas (54 vs 615 $m^2 g^{-1}$). Subsequently, CO_2 uptakes at 273 K and 1 bar were measured to be 0.648 and 2.21 mmol g^{-1} for **CK-POP-1** and **CK-POP-2** respectively.

Sun *et al*. have demonstrated that the geometric structure of the monomer can drastically influence a CPPs CO_2 uptake.[274]

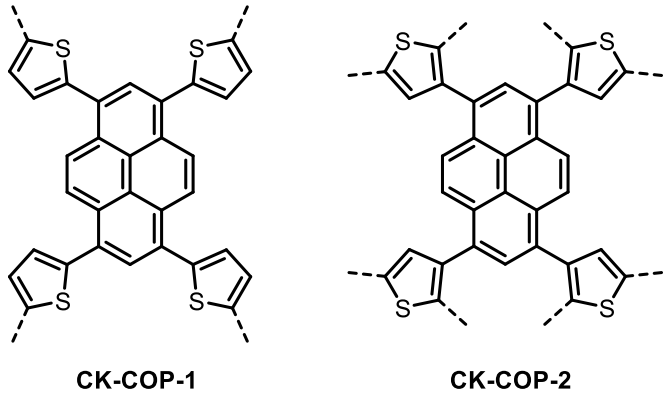

Fig. 79 Structure of isomeric **CK-COP-1** and **CK-POP-2**.[273]

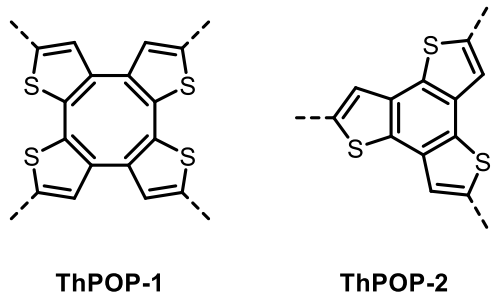

Fig. 80 Structures of **ThPOP-1** and **ThPOP-2.** [274]

Two CPPs were prepared using cyclic thiophene oligomers **COTh** and **BTTh**, which when polymerised via oxidative coupling gave polymers **ThPOP-1** and **ThPOP-2** respectively (Fig. 80). In the first case, the build block is a rigid, saddle-shaped molecule that results in inefficient packing of **ThPOP-1**, generating a high surface area network (1050 m^2 g^{-1}). By comparison, **BTTh** is a planar monomer that allows stacking to occur in **ThPOP-2**, generating a lower surface area material (160 m^2 g^{-1}). The discrepancy in surface area between **ThPOP-1** and **ThPOP-2** is reflected in their CO_2 capture capacity that were 3.41 and 0.91 mmol g^{-1} respectively at 273 K and 1.0 bar. Additionally, **ThPOP-1** was also observed to have high hydrogen uptake capacity (2.23 wt%), suggesting that the lone pairs of electrons on the thiophene may also enhance hydrogen-framework interactions.

An alternative method to modify CO_2 sorption by changing the building blocks employed is to utilise post-synthetic modification. For example, Ratvijitvech *et al.* have utilised post-synthetic amidation of an amine-bearing CMPs as a means of altering their porous properties (Fig. 7).[104] However, they noted that the modification led to partial pore occupation by the alkyl chains. Subsequently, the CO_2 and isosteric heat of adsorption decreased for the amide CMPs.

El-Kaderi and coworkers have explored post-synthetic installation of nitro- and amino- groups as a method to enhance CO_2 capture.[293] The parent polymer **NPOF-1**, prepared by Yamamoto coupling of 1,3,5-tris(4-bromophenyl)benzene, had a high surface area (2062 m^2 g^{-1}) but lacked any polar groups and thus possessed a modest CO_2 adsorption of 1.52 mmol g^{-1} (at 298 K and 1 bar). Mild nitration of this CMP using a slight excess of HNO_3/H_2SO_4 produced **NPOF-1-NO_2** and led to an increase in the CO_2 adsorption capacity to 2.52 mmol g^{-1}. However, the use of excess HNO_3 and long reaction times yielded a nitrated CMP **NPOF-1-NO_2(xs)** with reduced surface area (749 m^2 g^{-1} compared to 1295 m^2 g^{-1} for **NPOF-1-NO_2**). This was subsequently reflected by the lower CO_2 uptake of 2.00 mmol g^{-1}. The reduction of these nitro- decorated CMPs to **NPOF-1-NH_2** and **NPOF-1-NH_2 (xs)** was accompanied by an increase in the CO_2 adsorption to 3.77 and 2.93 mmol g^{-1} respectively. El-Kaderi and coworkers have also investigated enhancing the CO_2 adsorption capacity of bis(imino)pyridine based CPPs by post-synthetic formation of copper complexes.[289]

CMPs featuring an azide functional group have permitted post-synthetic functionalisation using azide-alkyne "click" chemistry to include pentafluoroaryl groups (Fig. 81).[279] The BET surface area of the azide bearing CMPs ranged from 477 m^2 g^{-1} for **ZnP-100%N_3-CMP** to 711 m^2 g^{-1} **ZnP-5%N_3-CMP**. Upon post-synthetic functionalisation, the CO_2 uptakes increased by 1.31 – 1.84 times at room temperature depending on fluorine content, despite a decrease in the surface area for all CMPs.

Another strategy which has been demonstrated to enhance the CO_2 adsorption capacity of CMPs is by potassium hydroxide assisted carbonisation at elevated temperatures.[295] Mane *et al*. have reported that upon carbonisation of tetraphenylethylene based CMPs at 600 – 800 °C, the BET surface area and volume of the micropores both increased with a concordant increase in the CO_2 uptake. The uptake of CO_2 increases with the temperature of carbonisation, which can be attributed to large surface areas generated by large pores collapsing into smaller micropores.

It should be mentioned that careful building block selection allows CPPs to act as dual functional materials, not only being able to adsorb CO_2 but also using it as a source of the C1 building block. The latter function has already been discussed in section 2.2.3.

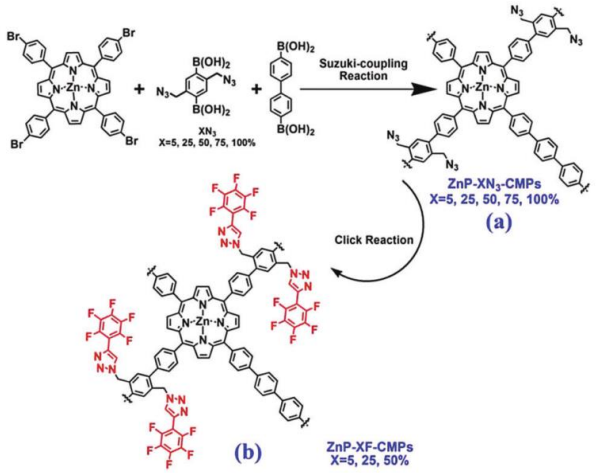

Fig. 81 Synthesis of ZnP-XN_3-CMPs by Suzuki-Miyuara coupling followed by post synthetic click chemistry to introduce the pentafluoroaryl groups. Reproduced from Ref. 279 with permission from the Royal Society of Chemistry, copyright 2017.

3.4.2 Dihydrogen Hydrogen gas is an environmentally clean and efficient fuel because of its high energy density and lack of greenhouse gases produced upon combustion.[296] Several strategies have been researched for storing hydrogen fuel such as chemisorption onto metal surfaces, storage in the form of clathrate hydrates or physisorption onto porous materials.[297–300]

There have been several notable examples of CPPs applied to the photochemical generation of hydrogen via water splitting and these are discussed in section 2.1.7. However, CPPs could also be used as a storage medium for the hydrogen fuel. In terms of high hydrogen uptake, CPPs benefits from large BET surface areas and the combination of small pore sizes and large volumes as these factors facilitate sorption of hydrogen gas. Various studies have demonstrated that the hydrogen adsorption ability of CPPs could be improved by increasing the volume of micropores and ultramicropores.[82,237,301,302] This is because pores within this regime, and not mesopores, mostly contribute towards hydrogen adsorption. The hydrogen adsorption capacity of various CPPs is summarised in table 2, with select representative examples discussed in this section.

Moderate H_2 storage capacity has been observed in conjugated microporous polycarbazoles prepared by Yamamoto coupling (Fig. 82). Through modifying the chemical structure and concentration of nitrogen atoms, the hydrogen adsorption could be varied between 0.75 – 1.35 wt%.[280] Overall, high surface area CMPs were conducive to higher hydrogen uptakes.

Doping of CMPs with Li^+ ions has been proven to be an effective strategy for enhancing hydrogen storage capacity. For example, the doping of 1,3,5-triethynylbenzene based CMPs with Li^+ ions resulted in marked improvements in storage capacity.[303] Lithium doping was achieved by dissolving lithium wire in a solution of naphthalene in THF and mixing this solution with the CMP. Following filtration, residual naphthalene was removed by heating under vacuum. The undoped CMPs exhibited a relatively small hydrogen uptake of 1.6 wt% at 1 bar which increased to 6.1 wt% on doping with 0.5 wt% of lithium. On increasing the lithium content beyond 0.5 wt%, the hydrogen uptake fell, which the authors attribute to agglomerisation of the lithium. Evidence for the effect of Li-doping was provided by analysis of the H_2 adsorption/desorption isotherms of the undoped CMP and the Li-doped CMP. With the intrinsic CMP, the initial uptake has a small slope that quickly attains saturation as the pressure is increased, suggesting a weak interaction between H_2 and the adsorbent network. In contrast, the adsorption/desorption isotherms for the Li-doped CMPs exhibited a large initial slope that then proceed to increase linearly, suggesting that strong interactions were involved in adsorption.

Computational studies on Li-doped CMPs for H_2 storage by Srinivasu and Ghosh demonstrated that the lithium atoms are held above and below the benzene rings, with a binding energy of approximately -187.9 kJ mol^{-1}.[304] The lithium sites were found to each possess a partial positive charge, arising from charge transfer from the metal atoms to the benzene ring, that could bind H_2 via ion-quadrupole and ion-induced dipole interactions.[305] This followed on from earlier work by Ghosh and coworkers, who demonstrated computationally that the van der Waals surfaces of C_nH_n aromatic systems (n=4,5,6,8) are not conducive to H_2 adsorption due to the weakness of the interaction. However, doping the organic systems with sodium (not lithium in this case) increased hydrogen adsorption, mainly due to electron transfer between the metal and the carbon ring.[306]

Lithium doping of CPPs to improve hydrogen uptake has also been demonstrated with organolithium compounds.[307] Naphthalene based CMPs loaded with methyllithium (3 wt% lithium) exhibited a 6.5 wt% uptake of H_2 at 77 K and 80 bar, which was a 150% increase compared to the intrinsic naphthalene CPP. This was larger than the 80% increase observed upon doping the same CPP with lithium atoms instead of methyllithium, even at higher lithium loading (9 wt%). This was attributed to several factors including agglomeration of lithium species at high loading and a greater number of H_2 molecules binding per methyllithium cluster compared to lithium ions. Computational calculations predicted that the naphthyl groups provided a binding site for methyllithium molecules, with a binding energy of 48.62 kJ mol^{-1} (Fig. 83). Other organolithium dopants were tested but these were not as effective at enhancing H_2 adsorption. For example, *n*-butyllithium is more sterically bulky than methyllithium, which

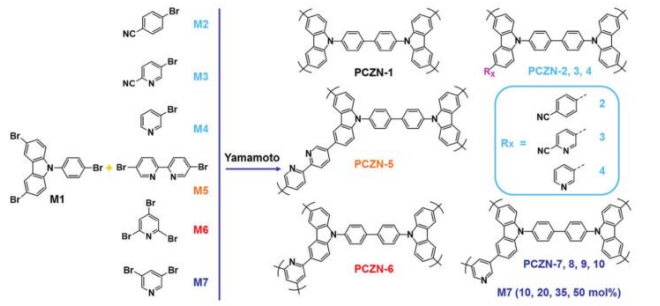

Fig. 82 Route to polycarbazole networks via Yamamoto coupling. Reproduced from Ref. 280 with permission from the Royal Society of Chemistry, copyright 2017.

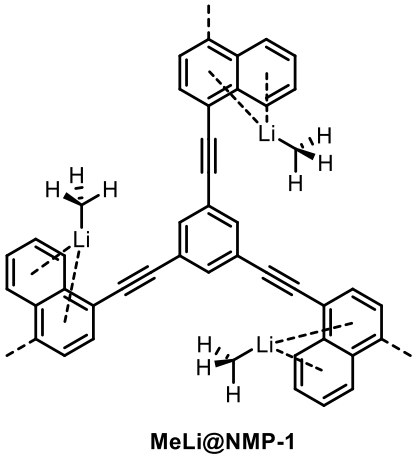

Fig. 83 Structure of **NMP-1** showing the proposed binding sites for molecules of methyl lithium.[307]

Table 2 Selection of the H_2 adsorption capacity data of various CPPs. To simplify comparison, all data has been converted into units of wt%.

Entry	Material	$SA_{BET}/m^2\ g^{-1}$	Temperature/ K	P/bar	Adsorption Capacity/wt%	Reference
1	Py-azo-COP	700	77	1	1.02	34
2	SPT-CMP1	1631	77	1.13	1.72	48
	SPT-CMP2	1601			1.57	
	SPT-CMP3	1334			1.34	
3	POP-1	1031	77	60	2.78	82
	POP-2	1013			2.71	
	POP-3	1246			3.07	
	POP-4	1033			2.35	
4	DCBP	2475	77	1	1.55	83
5	P1	397	77	1	1.32	86
	P2	834			1.36	
	P3	634			1.00	
6	SCMP1	505	77	1	0.77	100
7	CPN-1	856	77	1.13	1.14	108
	CPN-2	775			1.09	
	CPN-3	757			1.07	
	CPN-4	749			1.04	
	CPN-5	722			0.95	
	CPN-6	643			0.92	
8	PrPy	1219	77	1.13	1.69	181
	PrTPE	770			1.07	
9	BFCMP-1	1316	77	1.13	4.59	269
	BFCMP-2	1470			5.55	
10	PPTBC	917	77	1.13	1.69	270
	PMTBC	704			1.28	
	PPETBC	702			1.05	
	PMETBC	540			0.96	
11	ThPOP-1	1050	77	1	2.23	274
	ThPOP-2	160			1.03	
12	DA-CMP1	662	77	1.13	1.01	277
	DA-CMP2	603			0.82	
	Azo-CMP1	1146			1.60	
	Azo-CMP2	898			1.49	
13	PCZN-1	1003	77	1	1.11	280
	PCZN-2	607			0.98	
	PCZN-3	714			1.02	
	PCZN-4	374			0.84	
	PCZN-5	707			1.00	
	PCZN-6	718			1.12	
	PCZN-7	1058			1.28	
	PCZN-8	1126			1.35	
	PCZN-9	690			1.21	
	PCZN-10	391			0.75	
14	PCTF-1	2235	77	1	1.86	284
	PCTF-2	784			0.9	
15	HCMP-1	842	77	1.13	3.81	301
	HCMP-2	827			4.66	
16	COP-1	827	77	1.13	0.98	308
	Li@COP-1	573			1.67	
17	HPOP-1	1148	77	1.13	1.50	309
	HPOP-2	742			1.08	
18	Li-CMP	795	77	1	6.1	303
19	BILP-10	787	77	1	1.6	310
20	TPOP-1	472	77	1.13	0.83	311
	TPOP-3	765			1.00	
	TPOP-4	681			0.96	
	TPOP-5	810			1.07	

reduces the accessibility of the lithium site for H_2.

Xiang *et al*. reported on the synthesis of a CMP via Ni(0) catalysed Yamamoto coupling followed by post synthetic reaction with lithium naphthalenide in dry CO_2.[308] This led to partial conversion of alkynyl groups into lithium carboxylate groups that lead to an enhancement in CO_2, H_2 and CH_4 adsorption capacity despite a decrease in the surface area upon modification. In particular, the increase in H_2 capacity at 77 K and 1.13 bar was enhanced by 70.4% upon modification (from 0.98 to 1.67 wt%).

3.4.3 Methane As the primary component of natural gas, methane is an important energy resource and various porous materials have been investigated as storage media.301 In comparison to CO_2 and H_2, there has been much less focus on the development of CPPs for the adsorption and storage of methane gas. A summary of different CPPs and the amount of methane they can adsorb is provided in table 3.

3.4.4 Other Gases In addition to the adsorption of CO_2 for environmental remediation and H_2 and CH_4 for energy storage, there have been a few examples of CPPs being applied to the adsorption of other gases.

For example, Zhu and coworkers have reported on the adsorption of the Noble gases xenon and krypton by a CPP possessing sulfonic acid groups.[312] Adsorption measurements demonstrated a Xe uptake of 41.5 $cm^3\ g^{-1}$ and a Kr uptake of 12.2 $cm^3\ g^{-1}$ at 1 bar and 298 K. The selectivity for Xe over Kr reflects the higher heat of adsorption for the former (31 kJ mol^{-1} compared to 19 kJ mol^{-1} for Kr). The authors attribute this to the combination of small micropores which presented optimal van der Waal interactions for Xe and sulfonic acid groups that exerted an attractive force on Xe.

Other work by Zhu and coworkers have studied porphyrin based CMPs (including iron and manganese complexes) and their capacity to adsorbed small hydrocarbons (methane, ethylene, ethane and propane).[60] The authors generalise that the adsorption capacity followed the trend C3 > C2 > C1 (C referring to the number of carbons in the hydrocarbon). For example, at 273 K and 1 bar, the adsorption of propane was in the range of 51.2 – 63.0 $cm^3\ g^{-1}$. This was significantly higher than the methane adsorption which had values of 18.8 – 27.0 $cm^3\ g^{-1}$ under the same conditions. While this demonstrates the utility of CMPs to separate methane from longer chains hydrocarbons, separation of individual long chain hydrocarbons would remain difficult. due to the similarity in adsorption.

4 CPPs as Molecular Sensors

The combination of a conjugated π-system and photoluminescent properties makes CPPs promising materials for chemosensing applications. Furthermore, the porous conjugated framework provides a large surface area for sensor-analyte interactions, leading to improved sensing capabilities.[313]

The first example of a CMP-based chemosensor was reported by Liu *et al*. A CMP prepared by Yamamoto coupling of a carbazole derivative, **TCB-CMP**, exhibited increased fluorescence in the presence of electron-rich arene vapours and quenching in the presence of electron-poor analogues (Fig. 84).[36] This enhancement or quenching of the fluorescence was maintained even during cycle tests (3 times). Measuring the Stern-Volmer constant (K_{SV}) for various electron-deficient arenes demonstrated that the fluorescence quenching was greater for **TCB-CMP** (K_{SV} of 1.9 – 5.9 x 10^3 M^{-1}) in comparison to the linear analogue **CB-LP** (2.3 – 8.8 x 10^2 M^{-1}). The precise trend observed for the tested arenes differs from the K_{SV} since the sensing depends on the arene reduction potential and vapour pressure. With electron-rich arenes, the fluorescence intensity was enhanced by the presence of the CMP. The enhancement in fluorescence was dependent on the strength of the electron-donating groups present in the arene and their vapour pressure. The largest increase was observed with toluene, where the CMP exhibited 135% increase in fluorescence after only 20 s of exposure to the vapour. It was suggested that the extended π-structure of CMPs allowed for the migration of excitons while the porous features confined the analyte and presented a high surface area for interaction. In conjunction, these factors contributed to the enhanced detection performance over the linear polymer analogue.

One common application of CPPs in sensing is to detect nitroaromatic compounds which are commonly utilised as explosives. For example, CPPs prepared via Sonogashira-Hagihara cross coupling (Fig. 85) have demonstrated fluorescence quenching on exposure to trinitrotoluene (TNT).[35] The authors demonstrated the sensitivity of the various CPP to TNT vapour by utilising vapour adsorbed onto sand. Within an hour, lower fluorescence emission of the CPPs were observed.

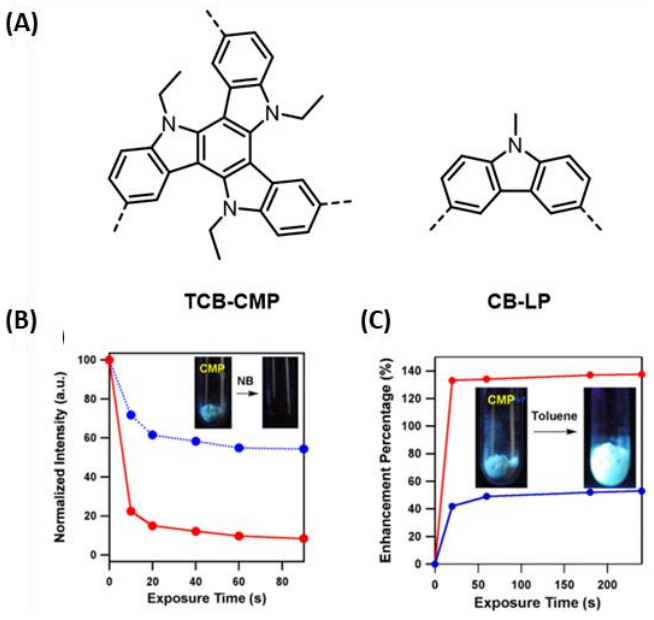

Fig. 84 (A) Structure of carbazole based **TCB-CMP** and linear analogue **CB-LB.** (B) Fluorescence quenching of **TCB-CMP** and **CB-LB** on exposure to nitrobenzene and (C) fluorescence enhancement of **TCB-CMP** and **CB-LB** on exposure to toluene. Red dots represent **TCB-LB** while blue dots represent **CB-LB**. Adapted with permission from Ref. 36. Copyright (2012) American Chemical Society.

Table 3 Selection of the CH_4 adsorption capacity data of various CPPs. To simplify comparison, all data has been converted into units of mmol g^{-1}.

Entry	Material	$SA_{BET}/m^2\ g^{-1}$	Temperature/ K	P/bar	Adsorption Capacity/mmol g^{-1}	Reference
1	PAF-40	601	273	1.1	0.91	60
			298		0.53	
	PAF-40-Fe	628	273		1.17	
			298		0.61	
	PAF-40-Mn	827	273		1.31	
			298		0.49	
2	TPB-BD-CMP	657	273	1.13	0.51	81
	TPA-BD-CMP	543			0.59	
	TPM-BD-CMP	1008			0.95	
	SPF-BD-CMP	833			0.85	
3	PrPy	1219	273	1.13	2.37	181
	PrTPE	770			1.28	
4	HP_E-CMP	662	273	1	0.45	206
5	BFCMP-1	1316	273	1.13	0.78	269
	BFCMP-2	1470			0.90	
6	PPTBC	917	273	1.13	0.76	270
	PMTBC	704			1.01	
	PPETBC	702			0.77	
	PMETBC	540			0.65	
7	CK-COP-1	54	273	1	0.22	273
	CK-COP-2	615			0.78	
8	Porp-TPE-CMP	547	273	1.05	0.38	275
	Porp-Py-CMP	31			0.26	
9	DA-CMP1	662	273	1.13	0.73	277
	DA-CMP2	603			0.53	
	Azo-CMP1	1146			1.18	
	Azo-CMP2	898			0.97	
10	PCTF-8	827	273	1	0.75	281
		573	298		0.40	
11	PCTF-1	2235	273	1	1.04	284
			293		0.62	
	PCTF-2	784	273		0.665	
			293		0.33	
12	BILP-15	448	273	1	0.84	290
			298		0.49	
	BILP-16	435	273		0.84	
			298		0.50	
	BILP-15(AC)	862	273		1.02	
			298		0.64	
	BILP-16(AC)	843	273		1.08	
			298		0.64	
13	BILP-10	787	273	1	1.00	292
			298		0.69	
	BILP-11	658	273		1.00	
			298		0.62	
	BILP-13	677	273		0.75	
			298		0.56	
14	ALP-5	801	273	1	1.44	294
			298		0.85	
	ALP-6	698	273		1.02	
			298		0.60	
	ALP-7	412	273		0.73	
			298		0.40	
	ALP-8	517	273		0.91	
			298		0.53	
15	COP-1	827	298	1	1.81	308
	Li@COP-1	573			2.43	

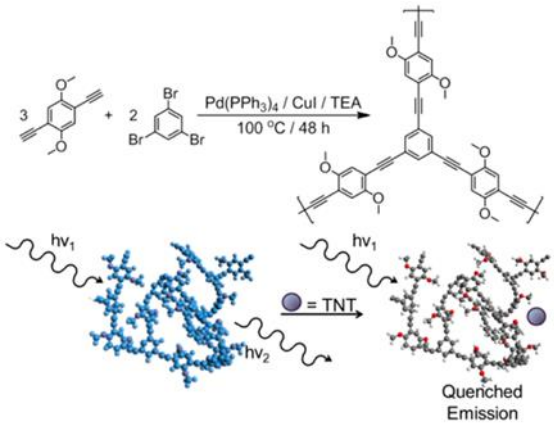

Fig. 85 Synthesis of a CPP for detection of trinitrotoluene and schematic representation of fluorescence quenching of the CPP in the presence of TNT. Modified with permission from Ref. 35. Copyright (2013) American Chemical Society.

The performance of the CPP was found to be dependent on the reaction solvent (DMF or toluene), with higher surface areas, that would present a larger area for interface, obtained with DMF. In addition to the solvent, it was observed that activating the CPPs by evacuation led to the porous structure collapsing, resulting in low-surface-area materials with poor detection properties. In contrast, activation by freezing the CPPs in 1,4-dioxane followed by lyophilisation limited pore collapse, leading to improved detection of TNT.

Chemical sensing of nitroarenes has also been reported in CMPs containing a variety of building blocks. These include fluorene-based CMPs which exhibited quenching of fluorescence in the presence of various arenes in solution (Fig. 86).[314] Among the CMPs synthesised, **FCMP3** exhibited the highest K_{SV} values of 2.541 x 10^3, 4.708 x 10^3 and 5.241 x 10^3 M^{-1} for nitrobenzene, nitrotoluene and dinitrotoluene, respectively. Testing the fluorescence of **FCMP3** using aliphatic nitro compounds and aromatic compounds that lacked nitro groups resulted in little fluorescence quenching, indicating that **FCMP3** could be used for selective sensing of nitroaromatics.

Covalent triazine frameworks prepared by cyclotrimerisation of pyrene building blocks have also been utilised for detecting 2,4,6-nitrophenol over other nitroaromatic compounds via fluorescence quenching.[281] This sensitivity towards the detection of 2,4,6-nitrophenol is reflected in its K_{SV}, which was reported as 1.32 x 10^5 M^{-1} which was higher the other tested analytes (nitrobenzene, p-nitrotoluene and dinitrophenol isomers). The detection of nitroaromatics has also been demonstrated with benzoquinone,[315] perylene tetraanhydridebisimide,[316] fluorene,[317] thiophene,[318] carbazole,[318,319] and tetraphenylethylene based CMPs.[70,320]

Sensing of nitro- compounds has also been observed in thin CMP films containing carbazole and tetraphenylethylene groups, prepared by electrochemical methods.[321] Sensitive quenching of the films fluorescence was observed for TNT vapours in concentrations as low as 5 – 10 ppb. In comparison, non-porous films of the tetracarbazole monomer experienced only minor quenching at TNT concentrations of 0.2 ppm indicating that microporosity and extended conjugation are

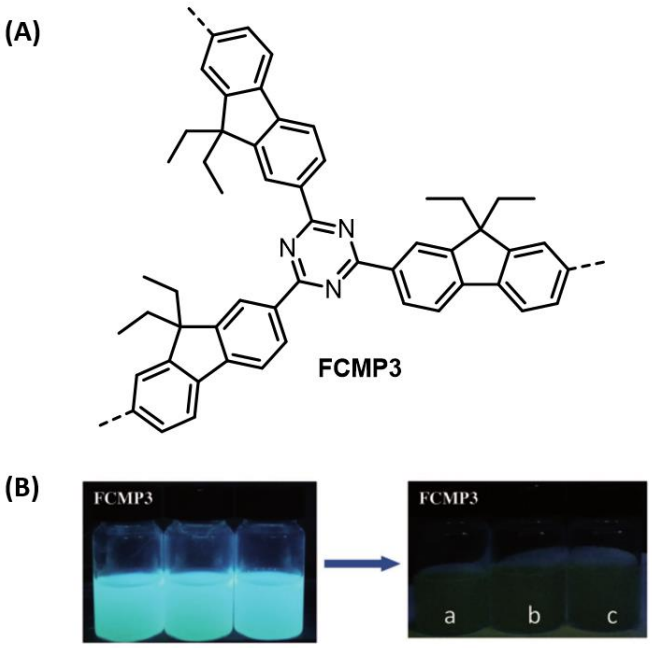

Fig. 86 (A) Structure of **FCMP3** and (B) quenching of fluorescence of **FCMP3** suspensions upon addition of nitrobenzene, nitrotoluene and dinitrotoluene (a, b and c respectively). Adapted from Ref. 314 with permission from Wiley-VCH, copyright 2017.

required for sensitive detection. Furthermore, substituting the tetraphenylethylene unit for a fluorenone group led to no response to TNT indicating that the tetraphenylethylene groups are necessary for the efficient photoinduced electron transfer from the CMP to the analyte.

Hollow microporous organic networks prepared via templating around silica nanoparticles along with tandem cyclisation to form isocoumarin groups have been applied to the detection of nitrophenols (Fig. 87).[322] The reported K_{SV} for various nitroaromatics were in the range of 6.3 – 15 x 10^3 M^{-1} while no quenching was observed with 4-chlorophenol, phenol and 4-methylphenol. This was explained in terms of the energy of the frontier molecular orbitals of the CPP, with electron transfer from the excited LUMO to the analyte LUMO being unfavourable.

While detection of explosives is by far the most prominent application of CPP chemosensors, detection of numerous other analytes has also been reported. Triarylboron-based CPPs (Fig. 88A) possess a vacant p_π-orbitals that can act as a luminescent chemosensors for detecting, and subsequent removal, of the fluoride anion.[282] Upon addition of the F^- anion to suspensions of the triarylboron CPP, the F^- binds strongly to the boron centre, inhibiting charge transfer from the nitrogen to the boron centre. This is reflected by decreasing intensity in the nitrogen to boron charge transfer band at 409 nm and an increase in the absorption band at 278 nm. Moreover, the addition of other anions such as chloride or hexafluorophosphate did not alter the colour of the solutions, indicating that triarylboron-based CPP chemosensors are selective for fluorine (Fig. 88B).

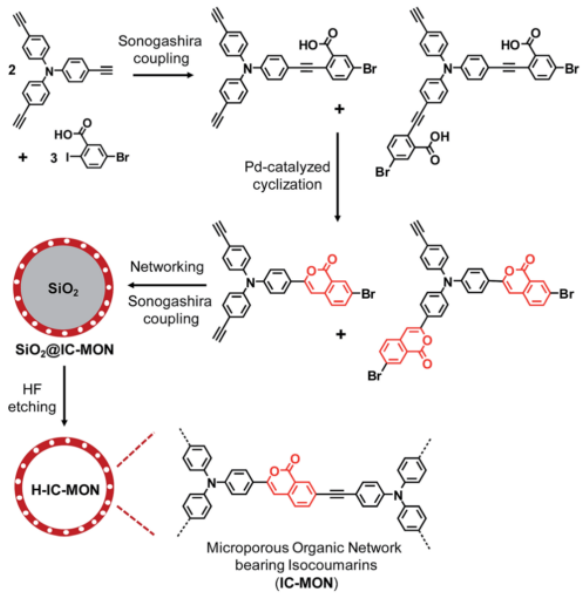

Fig. 87 Synthetic scheme to hollow microporous organic polymer. Reproduced from Ref. 322 with permission from the Royal Society of Chemistry, copyright 2016.

Detection of the antibiotic neomycin in water has been demonstrated using CMPs based on nickel-porphyrin and perylene moieties (Fig. 89).[323] The ligation of amino glycoside to the nickel(II) centre restricts the flexibility of the CMP, making it luminescent. This "turn on" biosensing was shown to be specific to neomycin, while other aminoglycosides and non-aminoglycoside antibiotics effected much weaker changes in emission intensity.

CMPs based on the chiral (*R*)-BINOL group have demonstrated enantioselective quenching of selected chiral amino acids.[76] The (*S*)-enantiomers of the amino acids displayed a higher K_{SV} value than the (*R*)-enantiomers (up to 1.23 times greater). This enantiomer-dependent quenching was attributed to the cavity confinement effect and the conformation of the rigid (*R*)-(+)-BINOL group.

Zhao *et al*. have reported on the fabrication of cross-linked conjugated polymers based sensing arrays mounted onto disposable paper cards.[324] The 6 x 6 arrays possessed 36 slightly different soluble conjugated polymer nanoparticles that produced different colour patterns under irradiation (365 nm) on exposure to different analytes (Fig. 90). These analytes included carboxylic acids, nitro-aromatics, alcohols, acids, aldehydes and amines.

Detection of heavy metal ions such as Cu(II), Hg(II), Cr(III) and Ni(II) has been demonstrated in an azo-linked CMP loaded with Ag(I) ions (see **Ag@Azo$_{TPE}$-CMP** Fig. 91).[325] In the presence of ethanol/water solutions containing these ions, the fluorescence of the CMP was heavily quenched by 93 – 99% depending on the metal ions present. In particular, fluorescence quenching of 35% was still observed when the concentration of Cu(II) solution was decreased to the 10^{-9} M scale. In comparison, the response of the CMP to the presence of Zn(II), Na(I), Ba(II) and Ca(II) was significantly lower indicating sensitivity towards transition metal ions, particularly Cu(II). Similarly, detection of heavy metal ions has been realised with thiophene based CMPs.[326] These CMPs were particularly sensitive to the detection of Hg(II) ions, which was ascribed to many factors including the affinity between sulfur and mercury. Even when the concentration of Hg(II) was decreased to the 10^{-8} M^{-1} scale, appreciable fluorescence quenching could still be observed.

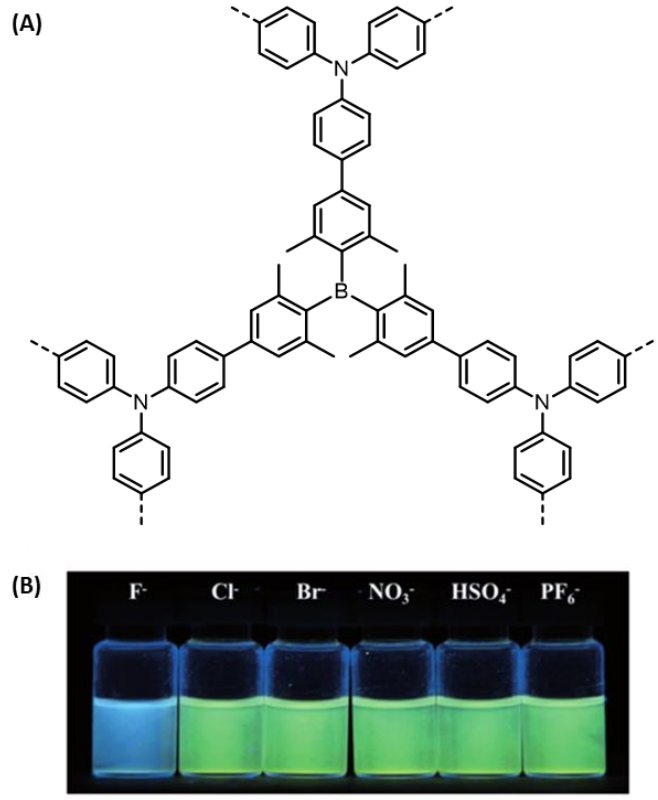

Fig. 88 (A) Structure of boron containing CMP and (B) fluorescence quenching in the presence of different ions in THF suspension (irradiated at 365 nm). Adapted from Ref. 282 with permission from Wiley-VCH, copyright 2015.

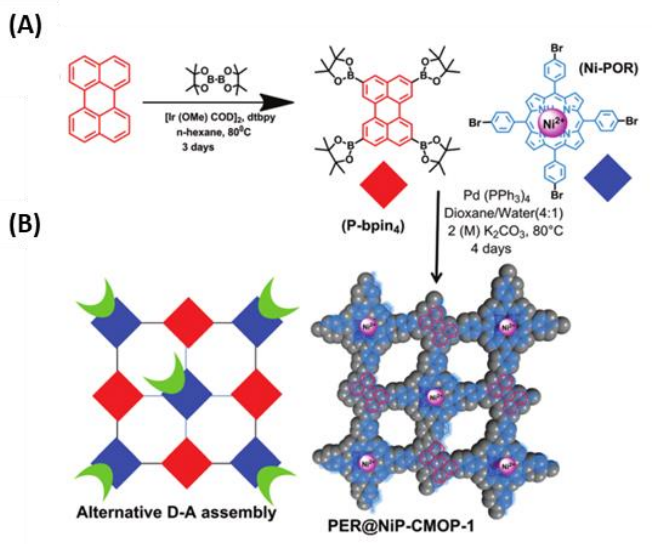

Fig. 89 (A) Representation of the synthetic scheme for a nickel porphyrin-perylene CMP. (B) Representation of the aminoglycoside to the nickel porphyrin complex for turn on sensing. Reproduced from Ref. 322 with permission from the Royal Society of Chemistry, copyright 2018.

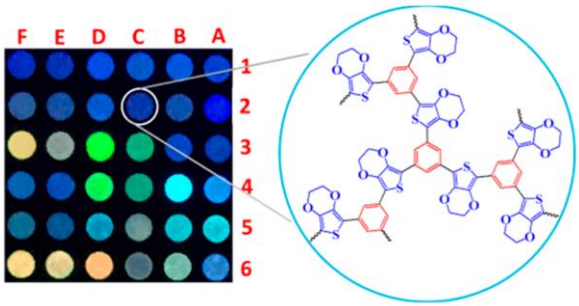

Fig. 90 Example of a fluorescent array sensor with an example of a structure highlighted. On exposure to different chemicals, a distinct array of colours is obtained. Reprinted with permission from Ref. 324. Copyright (2018) American Chemical Society.

Parallel to the conjugated porous polymers (CPPs, including conjugated microporous polymers, CMPs), their crystalline cousins of covalent organic frameworks (COFs) have also been widely examined for sensing applications, with similar emphases on metal ions,[327–332] explosives,[333–335] and other small molecule analytes.[336–339] As the use of COFs as sensors have been covered by recent reviews,[20,22,340] we here select examples in sensing applications for comparing the two systems of COFs and CPPs. In general,[341] the crystallinity of the COFs imparts well-defined structural order for structure-property correlation, and for potentially better selectivity (e.g., with uniform pore openings for size selectivity of the analytes); whereas the amorphous CPPs offer more functionalities and stability (e.g., without being limited by the reversible and labile boroxine and imine links entailed in COFs),[21,342] and are easier to prepare and process (e.g., into thin films/membranes and monoliths).

The structural order of the COF systems, however, has been under-utilised in sensor design, and their potential advantages over the amorphous CPP materials therefore remain to be fully realized. For example, the sensing of metal ions still depends heavily on the local, individual binding motifs (e.g., the soft thioether donors for Hg^{2+} sensing,[327] Fig. 92) built into the COF matrix; in other words, little design is made to configure the spatial arrangements of the donor groups within the ordered COF host, in order to boost concerted and selective binding of metal ions. In this regard, the current approach of COF sensor design resembles that of CPPs in their common focus on the local donor motif, as illustrated in Fig. 92. In Fig. 92A, the amorphous CPP features chelating N donors built in for metal binding and sensing.[343] The amorphous nature of the CPP scaffold makes it difficult to decipher the precise spatial distribution of the N donor groups. The local chelation motifs around the triazine core is nevertheless well-defined, and ensure effective binding of metal centres for sensing applications: e.g., the fluorescence of the CPP scaffold was effectively quenched by Ag(I), Pd(II) and other heavy metal ions.

The individual donor group remains the focus in crafting the COF sensor of Fig. 92B.[327] Namely, the thioether group is attached to the COF backbone to enhance metal binding (cf. sulfur-equipped metal-organic frameworks).[344–346] Indeed, the sulfur donor was found to be effective, with the fluorescence of the **COF-LZU8** host (dispersed in acetonitrile) selectively quenched by Hg^{2+} against various competitive cations (detection limit for Hg^{2+}: 25.0 ppb); while ethoxy side chains on a similar COF led to much weaker response to Hg^{2+}. The floppy side chains in the large pores of **COF-LZU8** are likely fluid, with variable and ill-defined spatial configurations of the S donors. Further tuning the spatial arrangement of the sulfur groups is therefore helpful not only for improving sensor performance (e.g., regarding detection limits), but also for unveiling the interactions between COF hosts and metal guests, as is increasingly being pursued in the MOF systems.[347–349]

In the challenging area of enantioselective sensing, progresses have also been made in both COF and CPP systems.[76,350] The BINOL-based chiral COF (**CCOF-7**; Fig. 93),[350] for example, can be exfoliated into nanosheets (**CCOF-7-NS**) by solvent-assisted liquid sonication. CCOF-7-NS dispersed in acetonitrile was found to be more sensitively quenched (e.g., regarding the emission at 380 nm) by (−)-(α)-pinene than by (+)-(α)-pinene, implying enantioselectivity in the fluorescent recognition. The slopes of the linear Stern–Volmer plots (i.e., the K_{sv} constant) were calculated to be 1348 and 395 M^{-1} with the (−) -and (+) enantiomers, respectively, affording the quenching ratio [QR = $K_{sv}(-)/K_{sv}(+)$] of 3.41 (Fig. 93). For processing, the **CCOF-7-NS** suspension in a DMF/acetone solution of PVDF (polyvinylidene fluoride) was electrospun onto aluminum foil substrates to produce free-standing nanofiber membranes of **CCOF-7-NS @PVDF**, which also exhibited significant enantioselective fluorescence quenching when exposed to the vapors of (α)-pinene and other terpenes. The enantioselective vapor recognition by the convenient optical

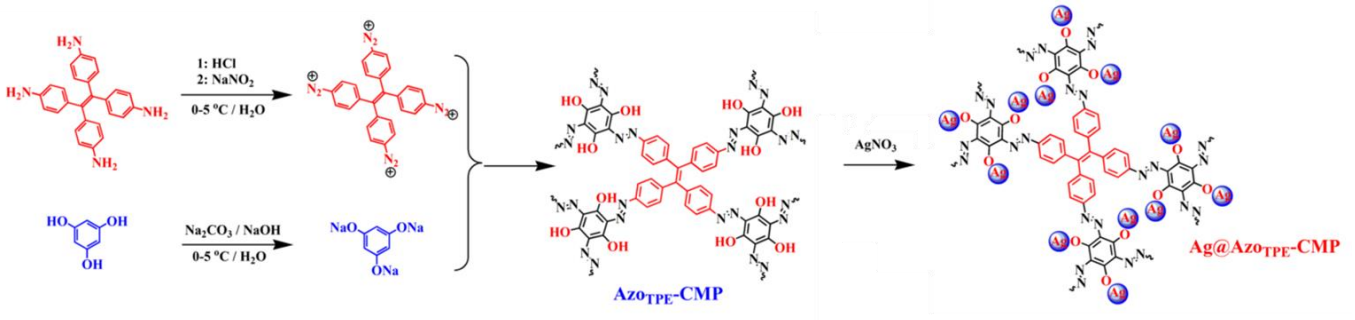

Fig. 91 Synthetic scheme for the synthesis of an azo-linked CMP **Azo$_{TPE}$-CMP** and subsequent modification to **Ag@Azo$_{TPE}$-CMP**. Adapted from 325 with permission from Springer Nature, copyright 2017. Available under CC-BY-4.0.

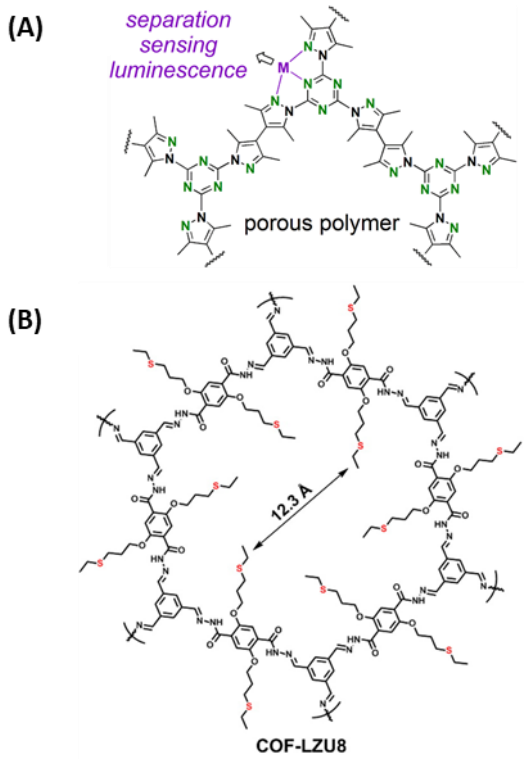

Fig. 92 An amorphous CPP with chelating N donors (A) built in for metal binding and sensing, and an imine-linked COF with thioether side groups (B) for metal binding and sensing. Adapted with permission from Ref. 343 and 327. Copyright (2014 and 2016 respectively) American Chemical Society.

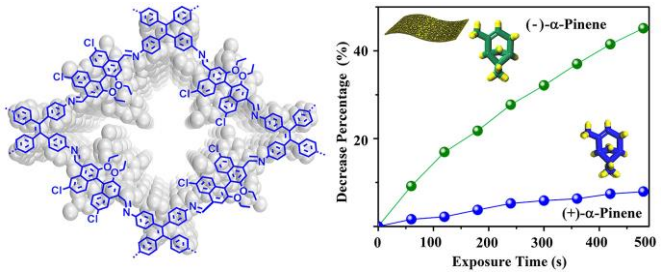

Fig. 93 An imine-based COF (**CCOF-7**) containing the tetraphenylethene and homochiral 1,1'-bi-2-naphthol (BINOL) building units for enantioselective fluorescent sensing of terpenes (e.g., α-pinene). Reprinted with permission from Ref. 350. Copyright (2019) American Chemical Society.

method here thus represent a major advance, even though higher sensitivity and enantioselectivity ought to be accessible by further leveraging the well-defined spatial confinement of the crystalline COF structure (e.g., to eventually emulate the binding specificity in proteins and other bio-scaffolds). The tuning and deciphering of the spatial configurations remain admittedly a tall order in the COF systems: for some time to come, both CPPs and COFs will represent equally worthwhile objects for materials science and technology research.

5 CPPs as Energy Materials

5.1 Capacitors

Supercapacitors are high-capacity energy storage devices that store potential energy in the form of an electric field. The characteristic features of supercapacitors are their high energy density and rapid charge and discharge cycles. Supercapacitive energy storage has been reported by Kou *et al.* in aza-fused CMPs.[91] This series of CMPs was constructed via phenazine ring fusion between 1,2,4,5-tetraminobenzene and triquinoyl hydrate at different temperatures in the region of 300 – 500 °C (Fig. 2). The temperature at which synthesis was observed to markedly influence the porous features of the aza-CMPs, with the pore size decreasing and the specific surface area increasing under higher-temperature conditions. However, it has been noted by others that these materials do not display rectangular cyclic voltammograms that are characteristic of a supercapacitor but instead display behaviour associated with high electrical resistance.[351]

There have been many reports of excellent capacitance properties observed in nitrogen containing CMPs. For example, Li *et al*. have demonstrated high specific capacitance in a series of triazatruxene based CMPs (Fig. 94).[352] The nitrogen atoms present in the triazatruxene moiety play an important role by enhancing the mobility of charge within the CMP and introducing anionic charges on the polymer surface. Electrodes prepared from CMPs exhibited a specific capacitance as high as 183 F g^{-1} at a current density of 1 A g^{-1} and a capacitance per unit of surface area greater than 160 µF cm^{-2}. High capacitance properties have also been observed in β-ketoenamine linked CMPs prepared by microwave promoted Schiff-base chemistry.[353] Electrodes manufactured from the CMP exhibited a high capacitance of 252 F g^{-1} at a current density of 1 A g^{-1} and can work well even at current densities in excess of 200 A g^{-1}. Supercapacitance has also been observed in conjugated microporous poly(zinc porphyrin) films prepared by electropolymerisation techniques on indium tin oxide substrates. The growth of this CMP was also demonstrated on flexible substrates such as indium tin oxide coated poly(ethylene terephthalate) films indicating that it had some mechanical strength.[354]

CPPs can also be used as precursor materials for supercapacitive porous carbon materials, formed by heating the CPP samples to high temperatures (Fig. 95). For example, Feng *et al*. have used Sonogashira-Hagihara cross-coupling to synthesise a series of CMPs which exhibited fibrous and tubular morphologies.[355] Pyrolysis of these materials yielded carbonaceous materials and was accompanied by a dramatic increase in surface areas from the untreated precursors. The resultant material demonstrated capacitive properties, with specific capacitances measured in the region of 103 – 115 F g^{-1} for sweep rates between 1 – 10 mV s^{-1}. Further examples of porous carbons prepared by pyrolysis of CMPs have involved the use of pyrene-based CMPs.[356] The temperature at which pyrolysis was carried out was demonstrated to influence the specific surface area and porous properties of the material, both of which in turn influenced the capacitive properties. Pyrolysis was carried out at 600, 700, 800 and 900 °C and this

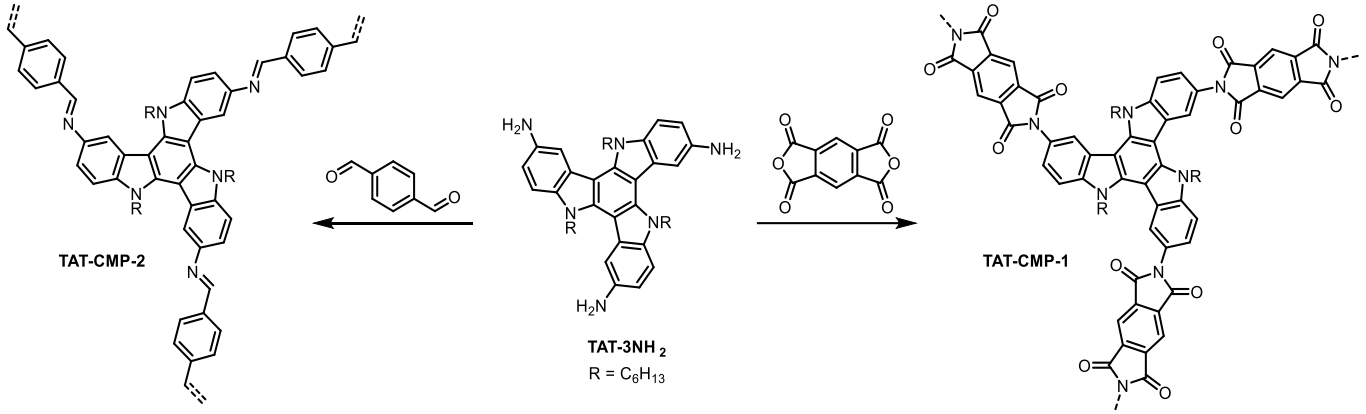

Fig. 94 Synthesis of **TAT-CMP-1** and **TAT-CMP-2** via Schiff base chemistry.[352]

led to surface areas of 605, 2098, 1520 and 2766 m^2 g^{-1}, respectively. Each of these values is larger than the specific surface area observed in the untreated CMP. The highest capacitance (301 F g^{-1} at a current density of 1 A g^{-1}) was observed when pyrolysis was carried out at 800 °C. The material prepared at 600 °C demonstrated significantly lower specific capacitance (195 F g^{-1}) which could be attributed to its lower surface area. While the material prepared at 700 °C exhibited a larger specific surface area, it demonstrated a lower specific capacitance (242 F g^{-1}). The higher capacitance obtained with pyrolysis at 800 °C was attributed to smaller and more numerous micropores with narrower size distributions. Elevating the pyrolysis temperature to 900 °C resulted in a decrease in capacitance (257 F g^{-1}).

Lee *et al.* have also reported on the preparation of supercapacitive porous carbons from CMPs.[351] Upon carbonisation, the capacitance of the materials were observed to increase, with the specific capacitance depending upon the pH during carbonisation: under acidic conditions a specific capacitance of 175.3 F g^{-1} was obtained (current density of 0.1 A g^{-1}) while a larger value of 260 F g^{-1} was attained under basic conditions.

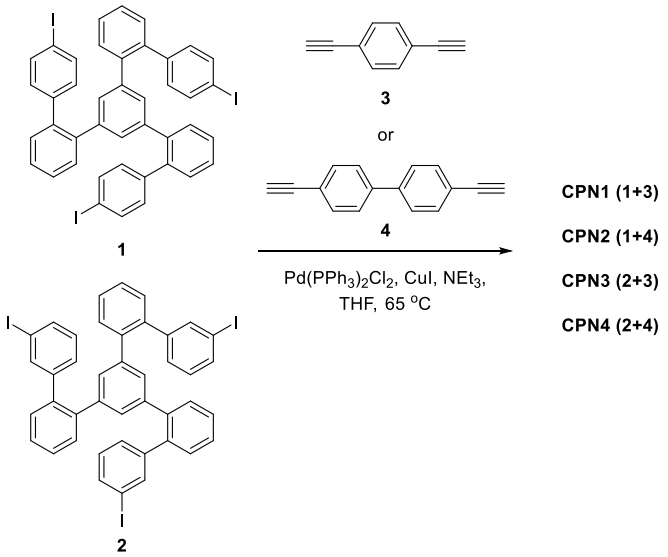

Fig. 95 Synthetic scheme for preparing CMPs **CPN1-4** for the generation of carbonised conductive materials.[355]

Xu *et al*. have described nitrogen doping as a means to improve the supercapactive properties of porous carbons materials prepared from CMPs.[357] One of the precursors utilised was prepared by Sonogashira-Hagihara cross coupling of 1,3,5-triethynylbenzene with 1,3,5-tribromobenzene. To introduce nitrogen into the material, the latter building block was substituted for a triazine unit. This was accompanied by an increase in the specific capacitance of the pyrolysed materials from 90 F g^{-1} to 264 F g^{-1} at a current density of 0.1 A g^{-1}. This increase was attributed to a greater ion diffusion rate and improved electron transportation that accompanied doping with nitrogen. Nitrogen-doped porous carbons have also been prepared from CPP systems based on carbazole,[358] porphyrin,[359] and triazine.[360,361]

Choi *et al*. have described the synthesis of CMPs containing carbonyl groups via Sonogashira-Hagihara coupling in the presence of carbon monoxide (CO) (Fig. 96).[362] The use of CO lead to the formation of redox active carbonyl groups in **H-CMP-BPPB**, not present in **H-CMP**, that could be utilised to store energy as a pseudocapacitor. The specific capacitance of this material was demonstrated to be in the range of 220 – 108 F g^{-1} at current densities of 0.5 – 20 A g^{-1}. For comparison, the CMP obtained in the absence of CO demonstrated capacities of 130 – 53 F g^{-1} within the same current density range.

5.2 Ion Batteries

Another energy storage application of CPPs is as electrodes in lithium ion batteries. These are a type of rechargeable battery in which movement of Li^+ ions from the cathode to the anode during discharge and the reverse process occurs during charging. Typically, one of the electrodes is made of a lithium-intercalated material.[363] As an alternative for these materials, CPPs offer advantageous properties suited to this application. The porous structure of CPPs facilitates transport and storage of ions throughout the material. In addition, the incorporation of heteroatoms such as nitrogen, boron or sulfur, into the material can provide redox sites to store Li^+ ions. For example,

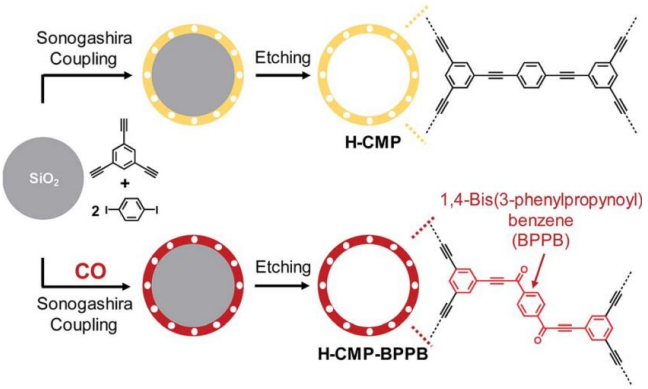

Fig. 96 Synthesis of **H-CMP** and **H-CMP-BPPB** via Sonogashira-Hagihara coupling. Reproduced from Ref. 362 with permission from the Royal Society of Chemistry, copyright 2018.

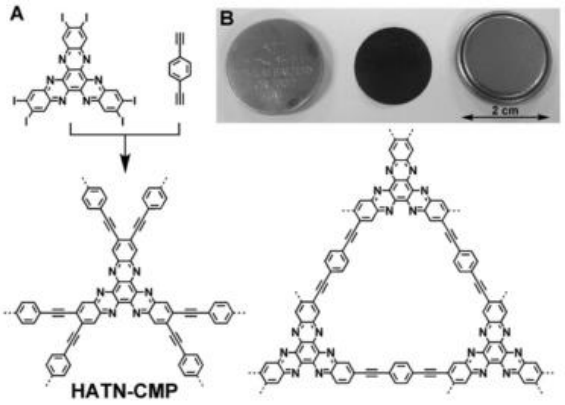

Fig. 97 (A) Representation of the synthesis and structure of **HATN-CMP**. (B) Photographs of the fabricated electrode and battery devices containing **HATN-CMP**. Reproduced from Ref. 366 with permission from the Royal Society of Chemistry, copyright 2014.

electrodes for lithium ion storage have also been prepared from nitrogen containing CMPs based on BODIPY and indole groups.[364,365]

Xu *et al.* have demonstrated lithium-battery energy storage utilising hexaazatrinaphthalene based CMPs (Fig. 97).[366] This material was used to prepare a cathode from a slurry of the CMP, acetylene black and poly(vinylidene difluouride) with subsequent removal of the solvent under vacuum. The capacity of the fabricated electrode was measured to be as high as 147 mA h g^{-1}. It was observed that the porous structure of CMP framework improved access of electrolyte ions to the redox-active site and enhanced cycling performance in comparison to the monomer. Wang *et al.* have also reported on the use of a sulfur-linked hexaazatrinapthylene based CMP in cathodes in coin cells.[367]

Thiophene-containing CMPs have also been used as materials for electrodes in lithium-ion batteries (Fig. 98).[368] In comparison to linear poly(thiophene), **PT**, the thiophene-based CMP, **P33DT**, exhibited a superior specific capacity of 1215 mAh g^{-1} compared to 596 mAh g^{-1} for the linear polymer at a current of 45 mA g^{-1}, This was attributed to the larger interfacial area and decreased ion diffusion distance presented by the cross-linked, porous material. It was also reported that the electrochemical performance of the CMP was dependent on the thiophene content, and replacing a portion of thiophene groups with benzene or pyrene, the specific capacity (at 45 mA g^{-1}) dropped from 1215 mAh g^{-1} to 991 and 684 mAh g^{-1} (for the benzene and pyrene based CMPs respectively).

Sodium ion batteries represent an alternative to the more common lithium ion batteries, with the notable advantage being the greater availability of sodium.[369] Storage materials for lithium ion batteries are typically rigid 3D networks with narrow channels that limits the use of sodium ions. In stark contrast, organic materials are more structurally flexible, potentially allowing insertion of sodium ions without hindrance from the material. To this end, Zhou *et al.* have reported the fabrication of electrodes using BTZ-carbazole based CMPs that could be used as both lithium and sodium ion batteries.[219] They note that the charge-discharge cycles for sodium storage are similar to lithium storage, albeit with lower energy storage capacity and slower kinetics. CMPs have also recently been explored for potassium ion batteries by Zhang *et al*.[370] Polybenzothiadiazole based CMPs resulted in a capacity as high as 428 mAh g^{-1} with excellent stability for 500 cycles.

5.3 Electrocatalysts

Another area of energy storage which CPPs could play an important role is as electrocatalysts for the oxygen reduction reaction, an important process in fuel cells. This reaction occurs at the cathode of a fuel cell, where oxygen is reduced to form water or other species depending upon conditions such as pH.[371] Zhuang *et al*. have reported on the preparation of 2D CMPs sandwiched between two sheets of graphene oxide. The graphene oxide, **GO**, was functionalised by reduction with hydrazine hydrate, forming **RGO**, followed by reaction with the diazonium salt of bromobenzene.[372] This yielded graphene oxide functionalised with bromine groups, **RGBr**, that could react with co-monomers to form the 2-D graphene-like material, **GMP** (Fig. 99). These 2-D CPPs were then carbonised to yield **GMC**, a porous carbon material doped with sulfur and nitrogen. These materials displayed a high efficiency when tested as electrocatalysts for the oxygen reduction reaction under alkaline conditions. Zhuang *et al*. have also demonstrated a similar strategy using carbon nanospheres, carbon nanotubes and graphene materials to synthesise 0-D, 1-D and 2-D CMPs

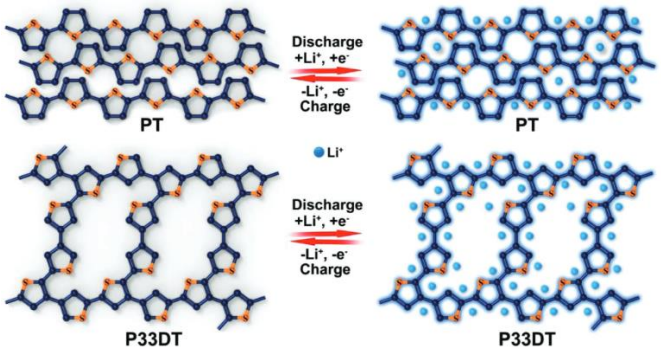

Fig. 98 Electrical Charging and discharging of linear poly(thiophene) **PT** and CMP analogue **P33DT**. Reprinted from Ref. 368 with permission of Wiley-VCH, copyright 2018.

respectively. These were carbonised to give boron and nitrogen doped porous carbons. When these materials were tested for the oxygen reduction reaction, the authors note that a correlation between the dimensionality of the nanocarbon and the electrochemical activity exists such that 2-D > 1-D > 0-D.[373] Electrocatalytic oxygen reduction reactions have also been observed in CMPs based on *tris*-(4-aminophenyl)amine and perylenediimide. These exhibited good activity as a metal-free electrocatalyst for the oxygen reduction reaction. Upon the incorporation of 2.56 wt% of cobalt nanoparticles into the CMP by *in situ* reduction its activity was increased significantly.[374]

5.4 Energy Conversion Devices

Energy conversion devices have also been fabricated from CPP materials. Gu *et al.* have reported that films of thiophene-based CMPs have been prepared on indium tin oxide substrates via electropolymerisation.[67] C_{60} fullerene doped films were then used to fabricate solar cells with power conversion efficiencies of 2.55 or 5.02%.

Mu *et al*. have studied the use of CMP aerogels as photothermal convertors, capable of harvesting light and generating heat, which they utilise to evaporate water by placing the aerogel on top of the water.[375] Under irradiation of 1 kW m^{-2} using a xenon arc lamp with a solar filter, pure water without the CMP aerogel evaporated at a rate of 0.4284 kg m^{-2} h^{-1}. Using the CMPs at the same intensity of light resulted in an increase in the rate of water evaporation (highest rate being 0.987 kg m^{-2} h^{-1}). Through the use of an infrared camera, the authors tracked the temporal increase in temperature upon sustained irradiation. Within 1000 s, the temperature of pure water reached 28 °C under a 1 kW m^{-2} illumination. In comparison, the temperature of the CMPs reached 35 °C within 1000 s, highlighting the light to thermal energy conversion properties of CMPs. Upon coating the CMP with carbon black, the evaporation rate increased to 1.3992 kg m^{-2} h^{-1} at a power density of 1 kW m^{-2}, producing an energy conversion efficiency of 81%. Both evaporation rate of the aerogel/carbon composite is larger than some other solar steam generators, such as carbonised foams (1.27 kg m^{-2} h^{-1}),[376] black silver (1.38 kg m^{-2} h^{-1}),[377] or tungsten oxide (1.28 kg m^{-2} h^{-1}),[378] but is less than other systems including carbon fibers (1.47 kg m^{-2} h^{-1}) at the same power density.[379]

Mu *et al*. have also explored utilising flexible monolithic CMP nanofoams to fabricate composite phase change materials (Fig. 100A).[380] These CMPs were prepared as monoliths by performing the synthesis in test tubes without stirring (Fig. 100B). Composite phase change materials reversibly store heat during solidification and melting processes, triggered by temperature variation. Due to the superoleophilic nature of the CMP nanofoams, the authors selected paraffin as the phase change material since it spontaneously absorbs into the porous structure with high loadings (1300 and 1500 wt%). Using differential scanning calorimetry, the phase change enthalpy could be measured for the paraffin (170 J g^{-1}) and for the paraffin/CMP composite, which varied between 138 and 161.5 J g^{-1} depending upon the identity of the CMP and the loading of paraffin.

5.5 Light Harvesting/Emitting Materials

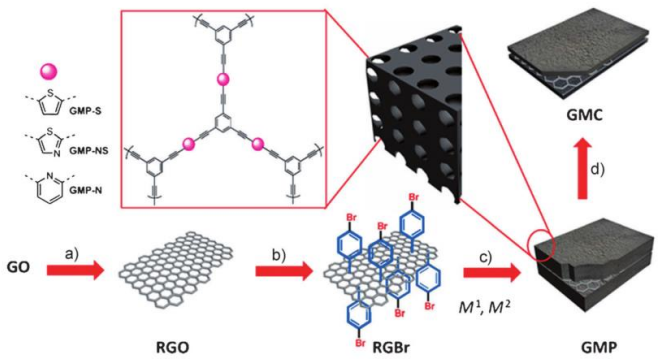

Fig. 99 Preparation of 2D graphene related CMPs from graphene oxide. Reproduced from Ref. 372 with permission from Wiley-VCH, copyright 2013.

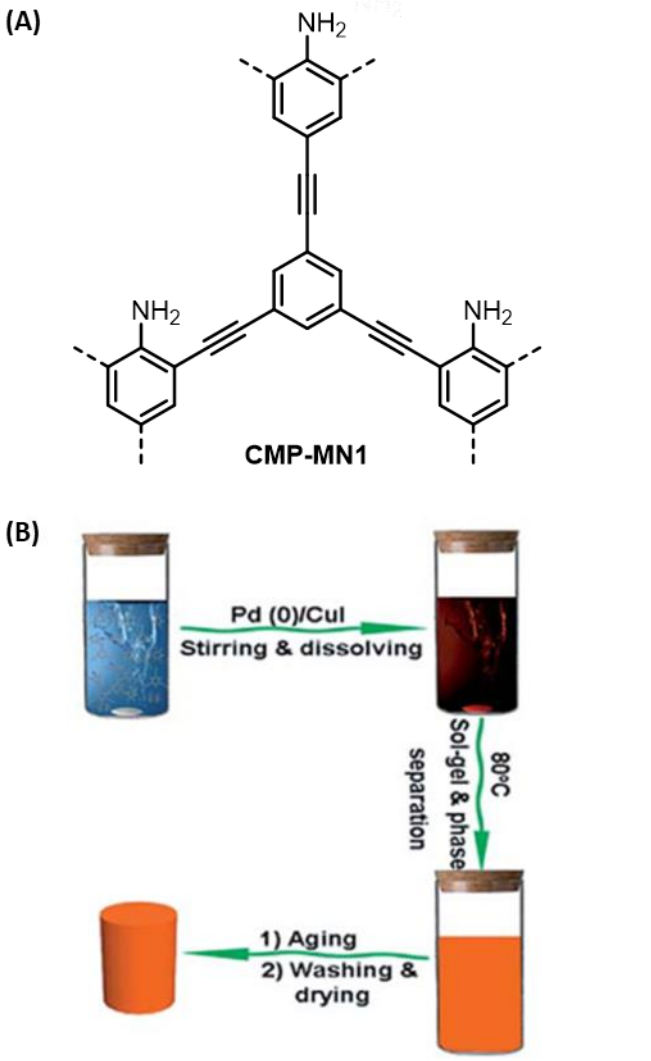

Fig. 100 (A) Structure of superoleophilic CMP **CMP-MN1**. (B) Representation of the method used to prepare the monolithic **CMP-MN1**. Adapted from Ref. 380 with permission from the Royal Society of Chemistry, copyright 2018.

In addition to bestowing materials with photocatalytic properties, the conjugated nature of CPPs also lends them to exhibit some interesting photophysical properties. For example, Xu *et al*. have demonstrated that incorporating tetraphenylethylene groups into CMPs leads to highly luminescence material.[50] The tetraphenylethylene group is a typical aggregation-induced emission chromophore, where rotation of the phenyl rings provides a non-radiative route to dissipate the energy of an excited state, subsequently reducing fluorescence. Upon aggregation of tetraphenylethylene derivates, restriction of these intramolecular rotations supresses the non-radiative dissipation route, leading to the radiative route being favoured.[381] By incorporating the tetraphenylethylene group into the polymer network, Xu *et al*. were also able to restrict rotation of the phenyl groups and thus generate a highly luminescence polymer. The authors note that by enforcing a planar conformation that extends π-conjugation, migration of excitons was facilitated and the luminescent properties of the CMP enhanced. Furthermore, they demonstrated that by varying the reaction time during CMP synthesis, the size of the particles and their absorption band could be altered. Increasing the reaction time led to larger particles with an increasing bathochromic shift as conjugation was extended.

Tuning of the emission wavelengths of CMPs has been achieved by utilising a core-shell strategy where one CMP is used as the core of the material and another is used as a shell around the first (Fig. 101).[382] In the first instance, the authors prepared a phenylene based CMP core, **PP_C-CMP**, by Suzuki-Miyuara coupling, which left boronic acid groups on the surface that could subsequently be used to form a tetraphenylethylene-based shell around the core (**TPE_S-PP_C-CMP**). In comparison to the core material alone, which absorbs at 312 nm, bathochromic shifts of in the absorption band of up to 39 nm were observed. Similarly, switching the order of phenylene and tetraphenylethylene, forming, **PP_S-TPE_C-CMP**, also induced a bathochromic shift in absorption. The extent of the bathochromic shift depended upon the thickness of the shell which could be controlled by varying the ratio of monomers. These materials emitted light of a single colour but as the thickness of the shell was increased the emission was also bathochromically shifted. Other strategies have also been investigated for modulating the emission and band gap properties of CMPs by copolymerisation of building blocks,[51,311,383] or by doping with small quantities of different electron acceptors units.[384]

Recently, Yuan *et al*. have fabricated polymer nanocomposites of CMP nanofillers within a 1,2-dioxetane cross-linked poly(methyl acrylate) (PMA) matrix.[385] When the 1,2-dioxetane polymer was subject to mechanical force, the weak O-O bond breaks leading to rearrangement to form two ketones (Fig. 102A). One of these ketones will be in an excited state and upon relaxation will emit blue light. The CMP nanofillers (prepared by Sonogashira-Hagihara and Knoevenagel chemistry) acted as fluorescent acceptors that improved the intensity of light resulting from mechanical force by up to 400% in comparison to the untreated PMA (Fig. 102B).

6 Conjugated Porous Polymers Utilising Supramolecular Chemistry

Supramolecular chemistry is defined as 'chemistry beyond the molecule', and in part focusses on systems of discrete chemical species held together by intermolecular forces.[386] Host-guest complexes are excellent examples of such behaviour, and involve the inclusion of one or more guest molecules within the cavity of a larger host such as cyclodextrins, calixarenes, cucurbiturils and pillararenes to name but a few. In the last few years there have been examples of CPPs reported that incorporate aspects of supramolecular chemistry or include host molecules as building blocks in system design.

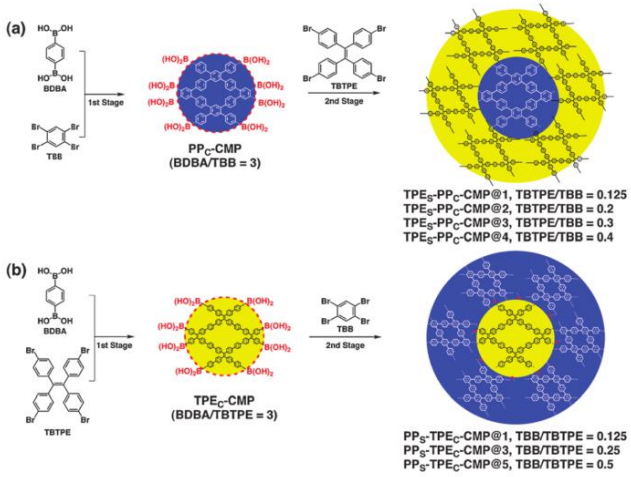

Fig. 101 Illustration of the synthesis of CMPs featuring a core-shell architecture. Reproduced from Ref. 382 with permission from the Royal Society of Chemistry, copyright 2013.

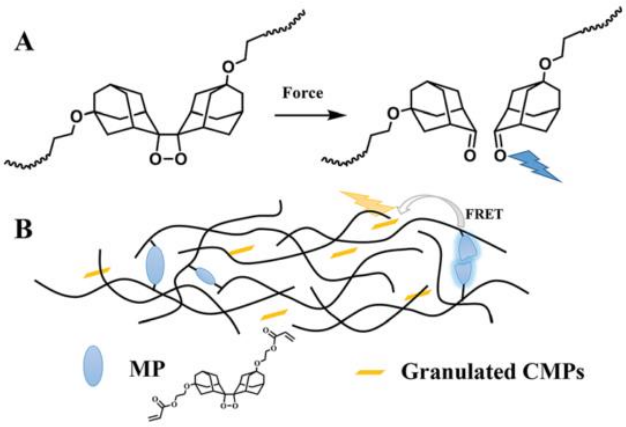

Fig. 102 (A) Mechanism for mechanochemiluminescence of a polymeric bis(adamantyl)-1,2-dioxetane. (B) Illustration of the mechanochemiluminescence in CMP/cross-linked PMA composites. Energy released by breaking apart the oxetane can be absorbed and emitted by the CMP filler. Reproduced from Ref. 385 with permission from the Royal Society of Chemistry, copyright 2019.

CPPs can act as hosts that incorporate guest molecules into the resulting pore structure. Computer simulations performed by Xu and Li have demonstrated that the binding of C_{60} and dye molecules is stronger with conjugated polymers than non-conjugated polymers.[387] Furthermore, the host polymer exhibits dynamic behaviour in order to accommodate the shape and size of its guests.

Zhao *et al*. have reported on the use of CMP films prepared by electrochemical deposition with pores that changed size in response to light stimulus as a means to reversibly store small organic molecules.[388] The CMP contained azo- benzene groups that could undergo reversible *cis-trans* isomerisation when irradiated by a laser with the appropriate wavelength of light (355 nm leads to the *cis*-configuration while 480 nm leads to *trans*-configuration). This isomerisation was accompanied by a change in the pore structure of the film which the authors studied using high resolution transmission electron microscopy. They discovered that the *trans*-configuration CMP had a pore size of 1.47 nm while the *cis*-configuration had a pore size of 0.87 nm. The authors demonstrated that when in the *trans*-configuration, 4,9-dibromonaphtho[2,3-c][1,2,5]thiadiazole could access the pore but then be trapped upon isomerisation to the *cis*-configuration. Irradiation with a 355 nm laser beam led to release of the trapped guest upon restoration of *trans*-configuration (Fig. 103). Such reversible guest encapsulation driven by light induced isomerisation of azo- groups can be compared examples based on discrete supramolecular systems: various cavitands based on resorcin[4]arenes, calix[4]arenes and calix[4]pyrroles exhibit changes in the volume of the container upon isomerisation of azo-groups, analogous to the change in pore size, allowing for reversible uptake and release of guest molecules.[389–391]

One interesting property of CPPs is that they the π-conjugated groups can harvest light energy and funnel the energy of many groups towards guest molecules contained within their pores. Chen *et al*. demonstrated that a polyphenylene based CMP could harvest light and then transfer this energy via fluorescence resonance energy transfer (FRET) from the network to the dye Coumarin 6 contained within the pores (Fig. 104).[392] Coumarin 6 displayed emission at 512 nm upon irradiating the CMP with light with wavelengths in the UV to visible range. Furthermore, the intensity of Coumarin 6 emission was enhanced by a factor of 21 when immobilised inside the pores in comparison to direct excitation. The reason for this is that many phenylene groups were able to harvest photons and then funnel this energy towards the guest species.

Funnelling of light energy to encapsulated small molecules has also been observed in pyrene based CMPs by Rao *et al*.[393] In the presence of hydrophobic solvents, the CMP swelled and experienced a hypsochromic shift in its emission spectra as well as an enhancement in the intensity of its fluorescence.[394] This swelling allowed for the facile encapsulation of the dyes 4-(dicyanomethylene)-2-methyl-6-(4-dimethylaminostyryl)-4*H*-pyran and Nile red. Upon encapsulation of the organic dyes, a hypsochromic shift in the CMPs emission spectra was also observed in addition to concomitant quenching of the CMPs fluorescence and enhanced dye emission. As the amount of encapsulated dyes was varied, the emission colour of the CMPs changed from green to red, demonstrating that the solid-state emission could be tuned via the use of luminescent guest molecules. Harvesting of light by CPPs and transfer of this energy to a single molecule has also been explored with Nile Red by Zhang *et al*., [395] and with rhodamine B by Suresh *et al*.[396]

CMPs incorporating pillar[5]arenes, P5-CMPs, demonstrating selective uptake of propane gas over methane have been studied by Talapaneni *et al*.[397] P5-CMPs exhibited an isosteric heat of adsorption for propane gas of 53 kJ mol^{-1} at zero coverage, which is significantly higher than values observed for other porous materials (ca. 33 – 37 kJ mol^{-1}). This suggests that significant C-H/π interactions, arising from inclusion of the propane gas within the pillar[5]arene cavity, were present. In comparison the isosteric heat of methane adsorption by P5-CMPs were significantly lower (20 kJ mol^{-1}).

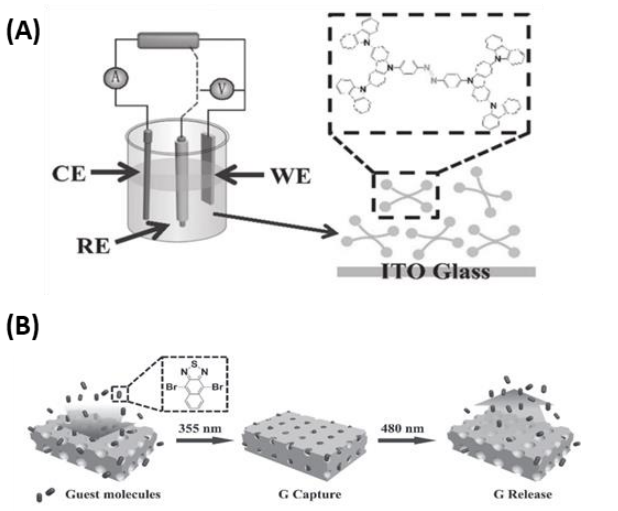

Fig. 103 (A) Electrochemical synthesis of a carbazole based azo-linked CPP on an indium-tin-oxide (ITO) substrate. (B) Photoresponsive capture and release of guest molecules (355 and 480 nm respectively) due to changes in the pore size upon photoisomerisation of the azo- groups. Adapted from Ref. 388 with permission from Wiley-VCH, copyright 2017.

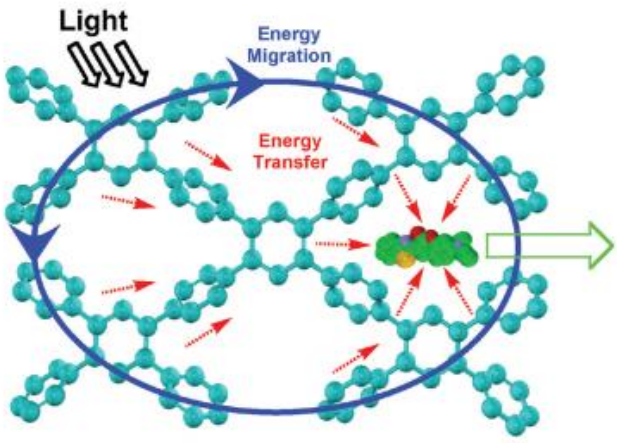

Fig. 104 Representation of the channelling of light energy harvested by a polyphenylene based CMP towards a molecule of Coumarin 6 confined within the micropores. Reprinted with permission from Ref. 392. Copyright (2010) American Chemical Society.

This was attributed to the better match between the diameter of the pillar[5]arene cavity (4.7 Å) and the kinetic diameter of propane rather than methane (4.3 and 3.8 Å respectively) This high affinity of P5-CMPs for propane allowed for the efficient separation from a mixture of methane and propane that was used to simulate natural gas (Fig. 105).

Li *et al*. have reported on a pillar[5]arene and tetraphenylethylene based CMP and its application in sensing of metal ions and 4-aminobenzene.[398] The CPP was first prepared by selectively modifying the rims of pillar[5]arene to include triflate functional groups that allowed Sonogashira-Hagihara coupling to be carried out. In the presence of Fe(III) ions, the fluorescence of CMP was quenched significantly (ca. 93%) while other ions exhibited weak quenching or enhancement of fluorescence. This was in part attributed to the good match in size between the ferric ion and the pillar[5]arene cavity. The authors also report that the fluorescence of the CPP was also efficiently quenched by the organic compound Oil Yellow B (98.5%).

More recent work by Li *et al*. has resulted in the preparation of CPPs consisting of pillar[5]arenes and porphyrin groups.[93] Notably, the synthesis of the CPP was carried out without the use of metals during the polymerisation step. The pillar[5]arene building block was first difunctionalised with aldehyde groups that allowed it to be subsequently condensed with pyrrole under acidic conditions to form porphyrin groups. Palladium nanoparticles were then dispersed throughout the material with narrow distribution in sizes, which the authors suggest that the pillar[5]arene groups could play a role in governing. The palladium nanoparticles were then used as catalysts in the Suzuki-Miyuara cross coupling and hydrogenation of nitroarenes using sodium borohydride.

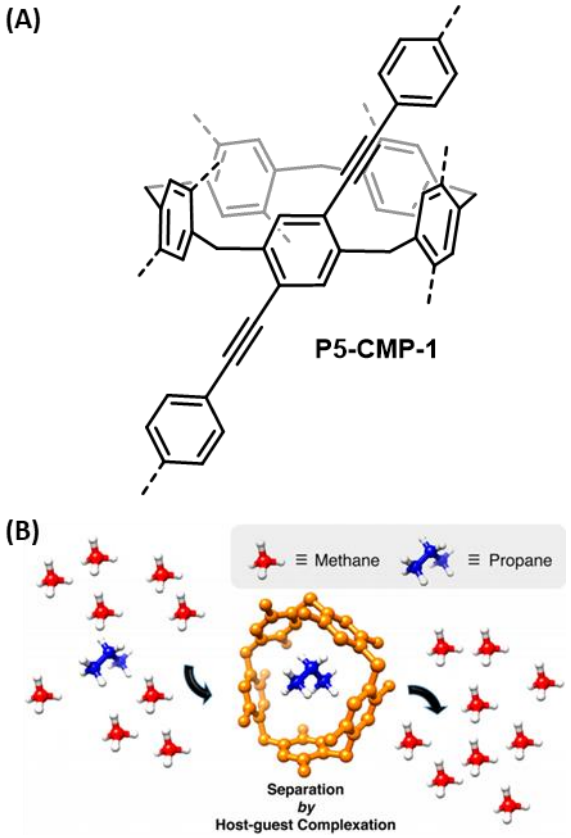

Fig. 105 Illustration of the separation of propane from methane gas by selective inclusion within the pillar[5]arene cavity of pillar[5]arene based CMPs. Reprinted with permission from Ref. 397. Copyright (2016) American Chemical Society.

7 Conclusions and Outlook

Recent times have witnessed the emergence of CPPs as a truly versatile class of porous materials offering clear potential for an equally diverse range of applications. Such potential is underlain by the unique combination of permanent porosity and π-conjugation within the robust polymer network, wherein the diverse array of building blocks available for construction presents plentiful opportunities for functionalisation. The continuous advances in synthetic methodology (e.g., regarding control over porous features), moreover, leads to ever more tailorable systems that could potentially respond to society's constant and dynamic requirement for efficient functional materials.

7.1 Emerging Syntheses Across MOFs and CPPs: improving crystalline order

One such advance is embodied in the two-step approach that is designed to overcome the abovementioned conundrum between bond strength and crystallinity: i.e., the strong covalent links for CPP construction form fast and irreversibly, leading to generally amorphous polymeric solids. It would be especially advantageous to combine the stability of CPP systems and the crystallinity of MOFs and related systems, because ordered structures generally facilitate structure-property correlation and allow one to better optimise properties and performance. For example, uniform pore sizes and features can greatly improve guest selectivity for sensing and separation applications; crystalline networks also offer improved control over defects and traps for enhanced electronic properties.

As illustrated in an early study (Fig. 106A),[399] the conceptual underpinning of the two-step strategy is simple. Therein, an organic ligand (**D7CN-6OH**) was first assembled with metal ions (e.g., Ag^+) into a crystalline porous network based on reversible coordination bonds; a reactive cross-linking agent was then diffused into the coordination solid to covalently link up the organic molecules (e.g., that of Si-O). Such a template method separates the crystallisation process from covalent bond formation, offering a general method for forming robust crystalline organic frameworks.

In a recent development that is more relevant to conjugated systems (Fig. 106B), domino/cascade thermocyclisation of the organic linkers (**SBF-4S2A**) was utilised to install highly conjugated, fused-aromatic bridges throughout the MOF scaffold, while preserving the crystalline order.[400] Incidentally, the choice of building blocks also reflects the profound evolution of framework materials chemistry over the past two decades. First, the highly charged, hard metal ion of Zr(IV) was used to engage the carboxylate donors, forming a robust Zr(IV)-

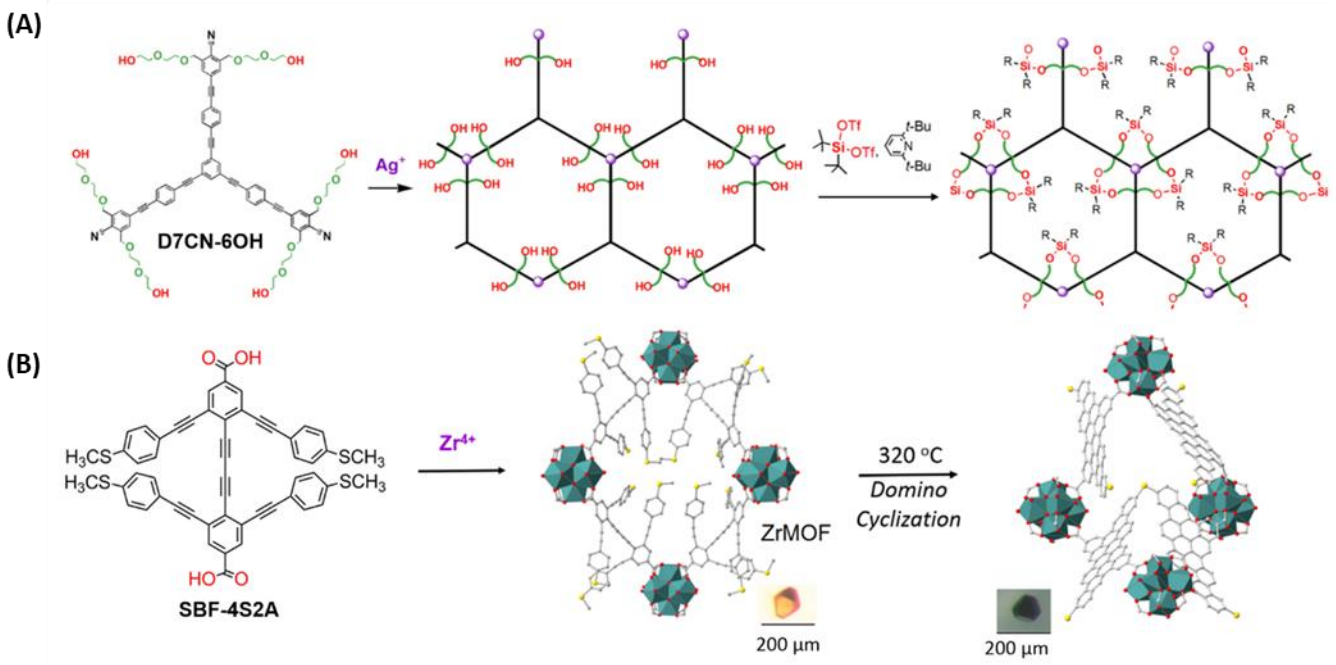

Fig. 106 (A) A two-step synthesis of a covalent network. The first step yields a precursor net based on the weak Ag^{+}-nitrile bond. The silyl agent then cross-links the –OH groups to form the strong covalent Si-O links. (B) Formation of a ZrMOF (shown as an octahedron based on Zr-O clusters and the linkers) from the dicarboxylic acid with backfolded alkyne backbone (**SBF-4S2A**), and subsequent thermocylisation of the crystals of the ZrMOF. The ZrMOF builds on the same topology as the UiO series, but with four equatorial linkers absent in octahedral unit. The thermocyclised network (on the right) contains covalent links (e.g., the Ar-S-Ar unit) across the individual aromatic linkers. (A) Adapted from Ref. [401] with permission from Wiley-VCH, copyright 2019. (B) Adapted from Ref. 400 with permission from the Royal Society of Chemistry, copyright 2018.

carboxylate network that can sustain the thermal treatment at 320 °C; secondly, the sophisticated linker molecule features symmetrically backfolded (e.g., **SBF-4S2A**), highly unsaturated alkyne backbones that are primed for domino cyclisation to merge the linkers into a conjugated network of fused aromatics. As a result, the formation of cyclised carbon links not only greatly strengthens the precursor coordination scaffold, but more importantly, enhance electroactivity and charge transport throughout the polycyclic aromatic grid (e.g., the black, thermocyclised sample, upon doped with Br_2, exhibits a conductivity above 10^{-2} S m^{-1}). Besides cascade cyclisation, many other cross-linking reactions can be deployed to install conjugated/electroactive bridges that effectively integrate the two major classes of frameworks of MOFs and CPPs, as is reviewed recently to highlight the generality of the two-step synthesis.[401]

7.2 Emerging Applications

In addition to the established applications discussed in this review, recent work with CPPs has led to a variety of new and interesting applications. For example, CMPs with sulfonic acid groups have been studied as proton conductive materials.[402]

CMPs bearing benzotriazole groups have been utilised to prepare composites with epoxy resins to yield flame retardant materials.[403] The CMP exhibited a thermal conductivity of 0.03 W m^{-1} K^{-1} in air, which is lower than other flame retarding polymeric materials. On directly exposing the CMP to a butane torch they immediately turned black in colour as a layer of surface char formed that protected the bulk material by preventing heat and oxygen flow (Fig. 107). In addition, the incorporation of the benzotriazole group lead to the production of nitrogen gas at high temperatures, which is a much greener alternative to other flame-retardant gases. Similar work by the same authors tested the fire resistant properties of fluorine rich CMPs which upon exposure to heat also formed a layer of char but released hydrogen fluoride as a suppressing gas.[404] Given the highly corrosive nature of hydrogen fluoride, especially in comparison to nitrogen gas, the use of nitrogen-containing over fluorine-containing CPPs for fire suppression applications would seem like a useful design rule.

Recently, CMPs have been prepared using a mutant of the green fluorescent protein (gfp) chromophore that mimics the photophysics of natural gfp.[405] New examples of CPPs as catalytic materials have also been recently reported for oxygen evolution and oxygen reduction reaction,[406,407] CO_2 photoreduction,[408] and regeneration of the cofactor nicotinamide adenine dinucleotide (NADH).[409] In addition, a CMP with electrochromic properties, changing from yellow to red upon storing energy, has also been recently reported.[410] These recent reports represent just a few ways in which future research into CPPs could progress and evolve as the field continues to grow and expand.

7.3 Perspective Outlook

In closing, we highlight some practical barriers limiting the use of CPP materials outside of the laboratory, many of which relate to their synthesis. For example, the majority of CPP synthetic routes utilise metal-catalysed coupling reactions which rely

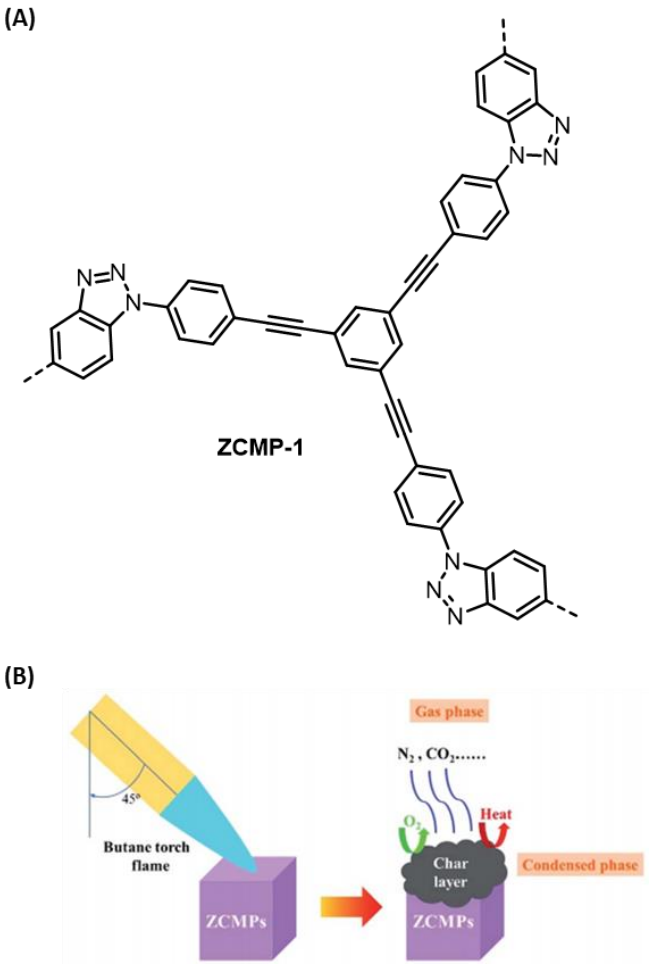

Fig. 107 (A) Structure of **ZCMP**. (B) Illustration of the flame retarding properties of benzotriazole based CMPs. Exposure to a flame results in the formation of a layer of carbon materials that prevent oxygen and heat diffusion. Reproduced from Ref. 403 with permission from the Royal Society of Chemistry, copyright 2018.

heavily on the use of catalysts containing expensive and unabundant metals such as Pd. While there have been a few reports of CPPs whose specific application is not detrimentally effected by the presence of trace residual metals,[52,88] there are several examples of residual Pd affecting the catalytic performance and electrical conductivity of cross-linked and linear conjugated polymers, and is therefore an issue of justifiable concern.[411–413] Furthermore, while Pd-catalysed cross-couplings are a staple of industrial and pharmaceutical synthesis, the tolerances placed on the level of residual metal contaminants are strict and the introduction of what could be ultimately avoidable impurities from CPPs appears counterintuitive. Considering these three reasons, metal-free synthetic routes, which remain relatively underdeveloped, warrant further exploration.

Another sticking point concerns the processing of CPP materials, which is heavily limited by their insolubility; consequently, research performed thus far has mainly focused on powder samples. Various strategies have been explored to influence the forms of the CPP products, including by means of pyrolysis, soluble CMPs, forming films via electropolymerisation, preparing membranes and forming monolithic structures. The latter is particularly interesting since such structures can be formed within fritted glass containers and incorporated into a continuous flow system.[43] This brings together the benefits of heterogeneous polymer-supported catalysis and the technological innovations of flow chemistry, two current topics of research that are both in keeping with the principles of green chemistry.[414–416]

Perhaps the most problematic limitation on the application of CPPs out with a laboratory environment is the cost associated with their construction. Not only does this include the cost of the building blocks, which can be expensive, but also the fact that these are used to assemble the bulk of the material. As an alternative, there have been some notable examples where the photoactive units have been attached to cheap polymer support such as polystyrene or cross-linked polyamide systems. Although the concentration of the photoactive component was far less then in related CPPs systems, these systems displayed comparable photocatalytic activity.[417–420] In these systems, metal-free polymerisation techniques (which could be translated onto an industrial scale) were used to prepare the polymers. Another approach would to be to consider utilising CPPs as fillers, exploiting their remarkable properties to enhance the characteristics of polymers by forming composite materials.[385,421]

Nevertheless, the success of CPPs in research clearly demonstrates that they provide versatile heterogeneous platforms that can be figuratively tailored to introduce specific functionality. Examples of this were provided when discussing CPP catalysis where homogeneous systems were translated into a heterogeneous regime. Moving forward, research into CPPs could draw on the extensive work performed on homogeneous systems, including photoredox and asymmetric catalysis. The challenge in this regard is translating homogeneous systems into a heterogenenous CPP catalysed regime, although research has proven that this is certainly an achievable goal.

As a final point, we envisage that innovative design and synthesis will also for production of ever more sophisticated multifunctional materials, which ultimately may offer to synergise various applications of CPPs within a single porous material.

Conflicts of interest

There are no conflicts to declare.

Acknowledgments

We acknowledge the EPSRC funded (EP/L016419/1) CRITICAT centre for doctoral training for Dominic Taylor's PhD. ZX acknowledges a GRF grant from the Research Grants Council of HKSAR (CityU 11306018).

References

1 A. G. Slater and A. I. Cooper, *Science*, 2015, **348**, aaa8075.
2 S. Kramer, N. R. Bennedsen and S. Kegnæs, *ACS Catal.*, 2018, **8**, 6961–6982.
3 J. Zhang, J. Chen, S. Peng, S. Peng, Z. Zhang, Y. Tong, P. W. Miller and X.-P. Yan, *Chem. Soc. Rev.*, 2019, **48**, 2566–2595.
4 N. Chaoui, M. Trunk, R. Dawson, J. Schmidt and A. Thomas, *Chem. Soc. Rev.*, 2017, **46**, 3302–3321.
5 P. Kaur, J. T. Hupp and S. T. Nguyen, *ACS Catal.*, 2011, **1**, 819–835.
6 C. Xu, W. Zhang, J. Tang, C. Pan and G. Yu, *Front. Chem.*, 2018, **6**, 1–12.
7 H. Bildirir, V. G. Gregoriou, A. Avgeropoulos, U. Scherf and C. L. Chochos, *Mater. Horizons*, 2017, **4**, 546–556.
8 A. Thomas, *Angew. Chem. Int. Ed.*, 2010, **49**, 8328–8344.
9 M. Dusselier and M. E. Davis, *Chem. Rev.*, 2018, **118**, 5265–5329.
10 Y. Wei, T. E. Parmentier, K. P. De Jong and J. Zečević, *Chem. Soc. Rev.*, 2015, **44**, 7234–7261.
11 Z. A. Alothman, *Materials*, 2012, **5**, 2874–2902.
12 J. G. Croissant, X. Cattoën, M. Wong Chi Man, J. O. Durand and N. M. Khashab, *Nanoscale*, 2015, **7**, 20318–20334.
13 J. Li, X. Wang, G. Zhao, C. Chen, Z. Chai, A. Alsaedi, T. Hayat and X. Wang, *Chem. Soc. Rev.*, 2018, **47**, 2322–2356.
14 S. Yuan, L. Feng, K. Wang, J. Pang, M. Bosch, C. Lollar, Y. Sun, J. Qin, X. Yang, P. Zhang, Q. Wang, L. Zou, Y. Zhang, L. Zhang, Y. Fang, J. Li and H.-C. Zhou, *Adv. Mater.*, 2018, **30**, 1704303.
15 A. Kirchon, L. Feng, H. F. Drake, E. A. Joseph and H.-C. Zhou, *Chem. Soc. Rev.*, 2018, **47**, 8611–8638.
16 T. Ben and S. Qiu, *CrystEngComm*, 2013, **15**, 17–26.
17 Y. Yuan and G. Zhu, *ACS Cent. Sci.*, 2019, **5**, 409–418.
18 H. Furukawa and O. M. Yaghi, *J. Am. Chem. Soc.*, 2009, **131**, 8875–8883.
19 M.-X. Wu and Y.-W. Yang, *Chinese Chem. Lett.*, 2017, **28**, 1135–1143.
20 H. V. Babu, M. G. M. Bai and M. R. Rao, *ACS Appl. Mater. Interfaces*, 2019, **11**, 11029–11060.
21 J. L. Segura, M. J. Mancheño and F. Zamora, *Chem. Soc. Rev.*, 2016, **45**, 5635–5671.
22 M. S. Lohse and T. Bein, *Adv. Funct. Mater.*, 2018, **28**, 1705553.
23 X. Ma and T. F. Scott, *Commun. Chem.*, 2018, **1**, 98.
24 L. Tan and B. Tan, *Chem. Soc. Rev.*, 2017, **46**, 3322–3356.
25 N. B. McKeown and P. M. Budd, *Chem. Soc. Rev.*, 2006, **35**, 675–683.
26 D. Ramimoghadam, E. M. A. Gray and C. J. Webb, *Int. J. Hydrogen Energy*, 2016, **41**, 16944–16965.
27 N. B. McKeown and P. M. Budd, *Macromolecules*, 2010, **43**, 5163–5176.
28 N. B. McKeown, *Int. Sch. Res. Netw.*, 2012, e513986.
29 A. I. Cooper, *Adv. Mater.*, 2009, **21**, 1291–1295.
30 R. Dawson, A. I. Cooper and D. J. Adams, *Prog. Polym. Sci.*, 2012, **37**, 530–563.
31 S. Das, P. Heasman, T. Ben and S. Qiu, *Chem. Rev.*, 2017, **117**, 1515–1563.
32 J.-T. Chen and C.-S. Hsu, *Polym. Chem.*, 2011, **2**, 2707–2722.
33 F. Vilela, K. Zhang and M. Antonietti, *Energy Environ. Sci.*, 2012, **5**, 7819–7832.
34 S. K. Gupta, D. Kaleeswaran, S. Nandi, R. Vaidhyanathan and R. Murugavel, *ACS Omega*, 2017, **2**, 3572–3582.
35 J. L. Novotney and W. R. Dichtel, *ACS Macro Lett.*, 2013, **2**, 423–426.
36 X. Liu, Y. Xu and D. Jiang, *J. Am. Chem. Soc.*, 2012, **134**, 8738–8741.
37 Y.-L. Wong, J. M. Tobin, Z. Xu and F. Vilela, *J. Mater. Chem. A*, 2016, **4**, 18677–18686.
38 Y.-B. Zhou and Z.-P. Zhan, *Chem. - An Asian J.*, 2018, **13**, 9–19.
39 B. C. Ma, S. Ghasimi, K. Landfester, F. Vilela and K. A. I. Zhang, *J. Mater. Chem. A*, 2015, **3**, 16064–16071.
40 J. M. Tobin, J. Liu, H. Hayes, M. Demleitner, D. Ellis, V. Arrighi, Z. Xu and F. Vilela, *Polym. Chem.*, 2016, **7**, 6662–6670.
41 J.-X. Jiang, F. Su, A. Trewin, C. D. Wood, N. L. Campbell, H. Niu, C. Dickinson, A. Y. Ganin, M. J. Rosseinsky, Y. Z. Khimyak and A. I. Cooper, *Angew. Chem. Int. Ed.*, 2007, **46**, 8574–8578.
42 Q. Liu, Z. Tang, M. Wu and Z. Zhou, *Polym. Int.*, 2014, **63**, 381–392.
43 K. Zhang, Z. Vobecka, K. Tauer, M. Antonietti and F. Vilela, *Chem. Commun.*, 2013, **49**, 11158–11160.
44 Y. Xie, T.-T. Wang, R.-X. Yang, N.-Y. Huang, K. Zou and W.-Q. Deng, *ChemSusChem*, 2014, **7**, 2110–2114.
45 K. Zhang, D. Kopetzki, P. H. Seeberger, M. Antonietti and F. Vilela, *Angew. Chem. Int. Ed.*, 2013, **52**, 1432–1436.
46 M. Liras, M. Iglesias and F. Sánchez, *Macromolecules*, 2016, **49**, 1666–1673.
47 B. Huang, P. Zhao, Y. Dai, S. Deng and A. Hu, *J. Polym. Sci. Part A Polym. Chem.*, 2016, **54**, 2285–2290.
48 J.-X. Jiang, A. Laybourn, R. Clowes, Y. Z. Khimyak, J. Bacsa, S. J. Higgins, D. J. Adams and A. I. Cooper, *Macromolecules*, 2010, **43**, 7577–7582.
49 J. Schmidt, M. Werner and A. Thomas, *Macromolecules*, 2009, **42**, 4426–4429.
50 Y. Xu, L. Chen, Z. Guo, A. Nagai and D. Jiang, *J. Am. Chem. Soc.*, 2011, **133**, 17622–17625.
51 J.-X. Jiang, A. Trewin, D. J. Adams and A. I. Cooper, *Chem. Sci.*, 2011, **2**, 1777–1781.
52 K. Zhang, B. Tieke, F. Vilela and P. J. Skabara, *Macromol. Rapid Commun.*, 2011, **32**, 825–830.
53 S. Hayashi, Y. Togawa, J. Ashida, K. Nishi, A. Asano and T. Koizumi, *Polymer*, 2016, **90**, 187–192.
54 S. Hayashi, Y. Togawa, S.-I. Yamamoto, T. Koizumi, K. Nishi and A. Asano, *J. Polym. Sci. Part A Polym. Chem.*, 2017, **55**, 3862–3867.
55 H. Bohra, S. Y. Tan, J. Shao, C. Yang, A. Efrem, Y. Zhao and M. Wang, *Polym. Chem.*, 2016, **7**, 6413–6421.
56 H. Bohra, P. Li, C. Yang, Y. Zhao and M. Wang, *Polym. Chem.*, 2018, **9**, 1972–1982.
57 X. Jiang, Y. Liu, J. Liu, X. Fu, Y. Luo and Y. Lyu, *New J. Chem.*, 2017, **41**, 3915–3919.
58 B. Li, Z. Guan, X. Yang, W. D. Wang, W. Wang, I. Hussain, K. Song, B. Tan and T. Li, *J. Mater. Chem. A*, 2014, **2**, 11930–

11939.
59 X. Xie, J. Wang, J. Zheng, J. Huang, C. Ni, J. Cheng, Z. Hao and G. Ouyang, *Anal. Chim. Acta*, 2018, **1029**, 30–36.
60 S. Meng, H. Ma, L. Jiang, H. Ren and G. Zhu, *J. Mater. Chem. A*, 2014, **2**, 14536–14541.
61 X. Ding and B.-H. Han, *Chem. Commun.*, 2015, **51**, 12783–12786.
62 X. Ding and B.-H. Han, *Angew. Chem. Int. Ed.*, 2015, **54**, 6536–6539.
63 Z. Guo, P. Sun, X. Zhang, J. Lin, T. Shi, S. Liu, A. Sun and Z. Li, *Chem. - An Asian J.*, 2018, **13**, 2046–2053.
64 Z. J. Wang, R. Li, K. Landfester and K. A. I. Zhang, *Polymer*, 2017, **126**, 291–295.
65 Y. Wei, W. Chen, X. Zhao, S. Ding, S. Han and L. Chen, *Polym. Chem.*, 2016, **7**, 3983–3988.
66 C. Gu, N. Huang, J. Gao, F. Xu, Y. Xu and D. Jiang, *Angew. Chem. Int. Ed.*, 2014, **53**, 4850–4855.
67 C. Gu, N. Huang, Y. Chen, L. Qin, H. Xu, S. Zhang, F. Li, Y. Ma and D. Jiang, *Angew. Chem. Int. Ed.*, 2015, **54**, 13594–13598.
68 S. Bai, Q. Hu, Q. Zeng, M. Wang and L. Wang, *ACS Appl. Mater. Interfaces*, 2018, **10**, 11319–11327.
69 H. Bildirir, I. Osken, T. Ozturk and A. Thomas, *Chem. - A Eur. J.*, 2015, **21**, 9306–9311.
70 C. W. Kang, D. H. Lee, Y. J. Shin, J. Choi, Y.-J. Ko, S. M. Lee, H. J. Kim, K. C. Ko and S. U. Son, *J. Mater. Chem. A*, 2018, **6**, 17312–17317.
71 M. Xu, X. Han, T. Wang, S. Li and D. Hua, *J. Mater. Chem. A*, 2018, **6**, 13894–13900.
72 X. Han, M. Xu, S. Yang, J. Qian and D. Hua, *J. Mater. Chem. A*, 2017, **5**, 5123–5128.
73 Y. Xu, S. Jin, H. Xu, A. Nagai and D. Jiang, *Chem. Soc. Rev.*, 2013, **42**, 8012–8031.
74 H. Bildirir, J. P. Paraknowitsch and A. Thomas, *Chem. - A Eur. J.*, 2014, **20**, 9543–9548.
75 M. Liu, B. Zhou, L. Zhou, Z. Xie, S. Li and L. Chen, *J. Mater. Chem. A*, 2018, **6**, 9860–9865.
76 J. Wei, X. Zhang, Y. Zhao and R. Li, *Macromol. Chem. Phys.*, 2013, **214**, 2232–2238.
77 P. Ju, S. Wu, Q. Su, X. Li, Z. Liu, G. Li and Q. Wu, *J. Mater. Chem. A*, 2019, **7**, 2660–2666.
78 H. Zhou, Q.-Y. Zhang and X.-B. Lu, *RSC Adv.*, 2016, **6**, 44995–45000.
79 S. Ren, R. Dawson, A. Laybourn, J. X. Jiang, Y. Khimyak, D. J. Adams and A. I. Cooper, *Polym. Chem.*, 2012, **3**, 928–934.
80 A. Laybourn, R. Dawson, R. Clowes, T. Hasell, A. I. Cooper, Y. Z. Khimyak and D. J. Adams, *Polym. Chem.*, 2014, **5**, 6325–6333.
81 Z. Xie, Y. Wei, X. Zhao, Y. Li, S. Ding and L. Chen, *Mater. Chem. Front.*, 2017, **1**, 867–872.
82 S. Yuan, B. Dorney, D. White, S. Kirklin, P. Zapol, L. Yu and D.-J. Liu, *Chem. Commun.*, 2010, **46**, 4547–4549.
83 P. Kuhn, M. Antonietti and A. Thomas, *Angew. Chem. Int. Ed.*, 2008, **47**, 3450–3453.
84 E. Troschke, S. Grätz, T. Lübken and L. Borchardt, *Angew. Chem. Int. Ed.*, 2017, **56**, 6859–6863.
85 J. Liu, J. M. Tobin, Z. Xu and F. Vilela, *Polym. Chem.*, 2015, **6**, 7251–7255.
86 M. Trunk, A. Herrmann, H. Bildirir, A. Yassin, J. Schmidt and A. Thomas, *Chem. - A Eur. J.*, 2016, **22**, 7179–7183.
87 J. H. Choi, K. M. Choi, H. J. Jeon, Y. J. Choi, Y. Lee and J. K. Kang, *Macromolecules*, 2010, **43**, 5508–5511.
88 C. Monterde, R. Navarro, M. Iglesias and F. Sánchez, *ACS Appl. Mater. Interfaces*, 2019, **11**, 3459–3465.
89 R. S. Sprick, J.-X. Jiang, B. Bonillo, S. Ren, T. Ratvijitvech, P. Guiglion, M. A. Zwijnenburg, D. J. Adams and A. I. Cooper, *J. Am. Chem. Soc.*, 2015, **137**, 3265–3270.
90 S. Ghasimi, S. A. Bretschneider, W. Huang, K. Landfester and K. A. I. Zhang, *Adv. Sci.*, 2017, **4**, 1700101.
91 Y. Kou, Y. Xu, Z. Guo and D. Jiang, *Angew. Chem. Int. Ed.*, 2011, **50**, 8753–8757.
92 P. Pandey, A. P. Katsoulidis, I. Eryazici, Y. Wu, M. G. Kanatzidis and S. T. Nguyen, *Chem. Mater.*, 2010, **22**, 4974–4979.
93 Z. Li, X. Li and Y.-W. Yang, *Small*, 2019, **15**, 1805509.
94 Q. Huang, L. Guo, N. Wang, X. Zhu, S. Jin and B. Tan, *ACS Appl. Mater. Interfaces*, 2019, **11**, 15861–15868.
95 B. P. Biswal, D. Becker, N. Chandrasekhar, J. S. Seenath, S. Paasch, S. Machill, F. Hennersdorf, E. Brunner, J. J. Weigand, R. Berger and X. Feng, *Chem. - A Eur. J.*, 2018, **24**, 10868–10875.
96 H. Zhou, B. Zhao, C. Fu, Z. Wu, C. Wang, Y. Ding, B.-H. Han and A. Hu, *Macromolecules*, 2019, **52**, 3935–3941.
97 Z. H. Guo, C. Wang, Q. Zhang, S. Che, H. C. Zhou and L. Fang, *Mater. Chem. Front.*, 2018, **2**, 396–401.
98 Z. Chen, M. Chen, Y. Yu and L. Wu, *Chem. Commun.*, 2017, **53**, 1989–1992.
99 S. Ju, Y. Ding, Y. Yin, S. Cheng, X. Wang, H. Mao, Z. Zhou, M. Song, Q. Chang, C. Ban, Z. Liu and J. Liu, *RSC Adv.*, 2019, **9**, 17399–17404.
100 G. Cheng, T. Hasell, A. Trewin, D. J. Adams and A. I. Cooper, *Angew. Chem. Int. Ed.*, 2012, **51**, 12727–12731.
101 R. Dawson, A. Laybourn, R. Clowes, Y. Z. Khimyak, D. J. Adams and A. I. Cooper, *Macromolecules*, 2009, **42**, 8809–8816.
102 B. Kiskan and J. Weber, *ACS Macro Lett.*, 2012, **1**, 37–40.
103 H. Urakami, K. Zhang and F. Vilela, *Chem. Commun.*, 2013, **49**, 2353–2355.
104 T. Ratvijitvech, R. Dawson, A. Laybourn, Y. Z. Khimyak, D. J. Adams and A. I. Cooper, *Polymer*, 2014, **55**, 321–325.
105 T. Hasell, C. D. Wood, R. Clowes, J. T. A. Jones, Y. Z. Khimyak, D. J. Adams and A. I. Cooper, *Chem. Mater.*, 2010, **22**, 557–564.
106 J. Rouquerol, D. Avnir, C. W. Fairbridge, D. H. Everett, J. M. Haynes, N. Pernicone, J. D. F. Ramsay, K. S. W. Sing and K. K. Unger, *Pure Appl. Chem.*, 1994, **66**, 1739–1758.
107 B. D. Zdravkov, J. J. Čermák, M. Šefara and J. Janků, *Cent. Eur. J. Chem.*, 2007, **5**, 385–395.
108 J.-X. Jiang, F. Su, A. Trewin, C. D. Wood, H. Niu, J. T. A. Jones, Y. Z. Khimyak and A. I. Cooper, *J. Am. Chem. Soc.*, 2008, **130**, 7710–7720.
109 J.-X. Jiang, A. Trewin, F. Su, C. D. Wood, H. Niu, J. T. A. Jones, Y. Z. Khimyak and A. I. Cooper, *Macromolecules*, 2009, **42**, 2658–2666.

110 Y. Xu and D. Jiang, *Chem. Commun.*, 2014, **50**, 2781–2783.
111 R. Dawson, A. Laybourn, Y. Z. Khimyak, D. J. Adams and A. I. Cooper, *Macromolecules*, 2010, **43**, 8524–8530.
112 B. Kim, N. Park, S. M. Lee, H. J. Kim and S. U. Son, *Polym. Chem.*, 2015, **6**, 7363–7367.
113 L. J. Abbott and C. M. Colina, *J. Chem. Eng. Data*, 2014, **59**, 3177–3182.
114 S. Chakraborty, Y. J. Colón, R. Q. Snurr and S. T. Nguyen, *Chem. Sci.*, 2015, **6**, 384–389.
115 J. Lee, J. G. Kim and J. Y. Chang, *Sci. Rep.*, 2017, **7**, 13568.
116 Z. J. Wang, S. Ghasimi, K. Landfester and K. A. I. Zhang, *Chem. Commun.*, 2014, **50**, 8177–8180.
117 I. Pulko and P. Krajnc, *Macromol. Rapid Commun.*, 2012, **33**, 1731–1746.
118 J. Lee, O. Buyukcakir, T.-W. Kwon and A. Coskun, *J. Am. Chem. Soc.*, 2018, **140**, 10937–10940.
119 E. R. Andrew, A. Bradburgy and R. G. Eades, *Nature*, 1958, **182**, 1659–1659.
120 I. J. Lowe, *Phys. Rev. Lett.*, 1959, **2**, 285–287.
121 U. Sternberg, R. Witter, I. Kuprov, J. M. Lamley, A. Oss, J. R. Lewandowski and A. Samoson, *J. Magn. Reson.*, 2018, **291**, 32–39.
122 S. P. Brown, *Solid State Nucl. Magn. Reson.*, 2012, **41**, 1–27.
123 M. Thommes, K. Kaneko, A. V. Neimark, J. P. Olivier, F. Rodriguez-Reinoso, J. Rouquerol and K. S. W. Sing, *Pure Appl. Chem.*, 2015, **87**, 1051–1069.
124 J. Weber, J. Schmidt, A. Thomas and W. Böhlmann, *Langmuir*, 2010, **26**, 15650–15656.
125 D. Lozano-Castelló, D. Cazorla-Amorós and A. Linares-Solano, *Carbon N. Y.*, 2004, **42**, 1233–1242.
126 K. A. Cychosz and M. Thommes, *Engineering*, 2018, **4**, 559–566.
127 K. A. Cychosz, R. Guillet -Nicolas, J. García -Martínez and M. Thommes, *Chem. Soc. Rev.*, 2017, **46**, 389–414.
128 S. Brunauer, P. H. Emmett and E. Teller, *J. Am. Chem. Soc.*, 1938, **60**, 309–319.
129 I. Langmuir, *J. Am. Chem. Soc.*, 1917, **39**, 1848–1906.
130 H. Swenson and N. P. Stadie, *Langmuir*, 2019, **35**, 5409–5426.
131 F. Rouquerol, J. Rouquerol and K. S. W. Sing, *Adsorption by Powders and Porous Solids*, Elsevier, San Diego, 2nd edn., 2014.
132 J. Landers, G. Y. Gor and A. V. Neimark, *Colloids Surf. A*, 2013, **437**, 3–32.
133 J. Roncali, *Macromol. Rapid Commun.*, 2007, **28**, 1761–1775.
134 M. A. El-Sayed, *J. Chem. Phys.*, 1963, **38**, 2834–2838.
135 S. K. Lower and M. A. El-Sayed, *Chem. Rev.*, 1966, **66**, 199–241.
136 M. Baba, *J. Phys. Chem. A*, 2011, **115**, 9514–9519.
137 J. C. Koziar and D. O. Cowan, *Acc. Chem. Res.*, 1978, **11**, 334–341.
138 J. Zhao, K. Chen, Y. Hou, Y. Che, L. Liu and D. Jia, *Org. Biomol. Chem.*, 2018, **16**, 3692–3701.
139 M. A. Zwijnenburg, G. Cheng, T. O. McDonald, K. E. Jelfs, J.-X. Jiang, S. Ren, T. Hasell, F. Blanc, A. I. Cooper and D. J. Adams, *Macromolecules*, 2013, **46**, 7696–7704.
140 R. S. Sprick, B. Bonillo, M. Sachs, R. Clowes, J. R. Durrant, D. J. Adams and A. I. Cooper, *Chem. Commun.*, 2016, **52**, 10008–10011.
141 I. Pibiri, S. Buscemi, A. Palumbo Piccionello and A. Pace, *ChemPhotoChem*, 2018, **2**, 535–547.
142 A. A. Ghogare and A. Greer, *Chem. Rev.*, 2016, **116**, 9994–10034.
143 M. C. DeRosa and R. J. Crutchley, *Coord. Chem. Rev.*, 2002, **233–234**, 351–371.
144 J. Liu, J. Cui, F. Vilela, J. He, M. Zeller, A. D. Hunter and Z. Xu, *Chem Commun*, 2015, **51**, 12197–12200.
145 C. Su, R. Tandiana, B. Tian, A. Sengupta, W. Tang, J. Su and K. P. Loh, *ACS Catal.*, 2016, **6**, 3594–3599.
146 W. Huang, B. C. Ma, H. Lu, R. Li, L. Wang, K. Landfester and K. A. I. Zhang, *ACS Catal.*, 2017, **7**, 5438–5442.
147 C. Ayed, L. C. da Silva, D. Wang and K. A. I. Zhang, *J. Mater. Chem. A*, 2018, **6**, 22145–22151.
148 Q. Li, H.-G. Wang, Y. Li, Y. Li and Q. Duan, *Dye. Pigment.*, 2018, **149**, 261–267.
149 L. Cai, Y. Li, Y. Li, H. Wang, Y. Yu, Y. Liu and Q. Duan, *J. Hazard. Mater.*, 2018, **348**, 47–55.
150 Y. Li, Q. Duan, H. Wang, B. Gao, N. Qiu and Y. Li, *J. Photochem. Photobiol. A Chem.*, 2018, **356**, 370–378.
151 Z. Xiao, Y. Zhou, X. Xin, Q. Zhang, L. Zhang, R. Wang and D. Sun, *Macromol. Chem. Phys.*, 2016, **217**, 599–604.
152 C. H. A. Tsang, J. M. Tobin, J. Xuan, F. Vilela, H. Huang and D. Y. C. Leung, *Appl. Catal. B Environ.*, 2019, **240**, 50–63.
153 Y. Li, L. Wang, Y. Gao, W. Yang, Y. Li and C. Guo, *RSC Adv.*, 2018, **8**, 7330–7339.
154 B. Wang, Z. Xie, Y. Li, Z. Yang and L. Chen, *Macromolecules*, 2018, **51**, 3443–3449.
155 B. C. Ma, S. Ghasimi, K. Landfester and K. A. I. Zhang, *J. Mater. Chem. B*, 2016, **4**, 5112–5118.
156 S. Ghasimi, K. Landfester and K. A. I. Zhang, *ChemCatChem*, 2016, **8**, 694–698.
157 Y. Xiang, X. Zhang, X. Wang, X. Ding, D. Huang and H. Chen, *J. Catal.*, 2018, **357**, 188–194.
158 N. Kang, J. H. Park, K. C. Ko, J. Chun, E. Kim, H.-W. Shin, S. M. Lee, H. J. Kim, T. K. Ahn, J. Y. Lee and S. U. Son, *Angew. Chem. Int. Ed.*, 2013, **52**, 6228–6232.
159 V. R. Battula, H. Singh, S. Kumar, I. Bala, S. K. Pal and K. Kailasam, *ACS Catal.*, 2018, **8**, 6751–6759.
160 Z. J. Wang, K. Garth, S. Ghasimi, K. Landfester and K. A. I. Zhang, *ChemSusChem*, 2015, **8**, 3459–3464.
161 Z. J. Wang, S. Ghasimi, K. Landfester and K. A. I. Zhang, *Adv. Mater.*, 2015, **27**, 6265–6270.
162 C. Ayed, W. Huang, R. Li, L. C. da Silva, D. Wang, O. Suraeva, W. Najjar and K. A. I. Zhang, *Part. Part. Syst. Charact.*, 2018, **35**, 1700234.
163 Z. J. Wang, S. Ghasimi, K. Landfester and K. A. I. Zhang, *Adv. Synth. Catal.*, 2016, **358**, 2576–2582.
164 J.-X. Jiang, Y. Li, X. Wu, J. Xiao, D. J. Adams and A. I. Cooper, *Macromolecules*, 2013, **46**, 8779–8783.
165 C.-A. Wang, Y.-W. Li, X.-L. Cheng, J.-P. Zhang and Y.-F. Han, *RSC Adv.*, 2017, **7**, 408–414.
166 M. Liras, M. Pintado-Sierra, M. Iglesias and F. Sánchez, *J. Mater. Chem. A*, 2016, **4**, 17274–17278.

167 Z. J. Wang, S. Ghasimi, K. Landfester and K. A. I. Zhang, *Chem. Mater.*, 2015, **27**, 1921–1924.
168 C. K. Prier, D. A. Rankic and D. W. C. MacMillan, *Chem. Rev.*, 2013, **113**, 5322–5363.
169 M. H. Shaw, J. Twilton and D. W. C. MacMillan, *J. Org. Chem.*, 2016, **81**, 6898–6926.
170 N. A. Romero and D. A. Nicewicz, *Chem. Rev.*, 2016, **116**, 10075–10166.
171 W. Zhang, J. Tang, W. Yu, Q. Huang, Y. Fu, G. Kuang, C. Pan and G. Yu, *ACS Catal.*, 2018, **8**, 8084–8091.
172 Z. J. Wang, S. Ghasimi, K. Landfester and K. A. I. Zhang, *J. Mater. Chem. A*, 2014, **2**, 18720–18724.
173 W. Ou, G. Zhang, J. Wu and C. Su, *ACS Catal.*, 2019, **9**, 5178–5183.
174 B. Kiskan, M. Antonietti and J. Weber, *Macromolecules*, 2012, **45**, 1356–1361.
175 S. Dadashi-Silab, H. Bildirir, R. Dawson, A. Thomas and Y. Yagci, *Macromolecules*, 2014, **47**, 4607–4614.
176 Z. J. Wang, K. Landfester and K. A. I. Zhang, *Polym. Chem.*, 2014, **5**, 3559–3562.
177 G. Liao, Y. Gong, L. Zhang, H. Gao, G. J. Yang and B. Fang, *Energy Environ. Sci.*, 2019, **12**, 2080–2147.
178 X. Wang, K. Maeda, A. Thomas, K. Takanabe, G. Xin, J. M. Carlsson, K. Domen and M. Antonietti, *Nat. Mater.*, 2009, **8**, 76–80.
179 K. Kailasam, J. Schmidt, H. Bildirir, G. Zhang, S. Blechert, X. Wang and A. Thomas, *Macromol. Rapid Commun.*, 2013, **34**, 1008–1013.
180 Y. Xu, N. Mao, S. Feng, C. Zhang, F. Wang, Y. Chen, J. Zeng and J.-X. Jiang, *Macromol. Chem. Phys.*, 2017, **218**, 1700049.
181 Y. Xu, C. Zhang, P. Mu, N. Mao, X. Wang, Q. He, F. Wang and J.-X. Jiang, *Sci. China Chem.*, 2017, **60**, 1075–1083.
182 Y. Xu, N. Mao, C. Zhang, X. Wang, J. Zeng, Y. Chen, F. Wang and J.-X. Jiang, *Appl. Catal. B Environ.*, 2018, **228**, 1–9.
183 Z. Wang, X. Yang, T. Yang, Y. Zhao, F. Wang, Y. Chen, J. H. Zeng, C. Yan, F. Huang and J.-X. Jiang, *ACS Catal.*, 2018, **8**, 8590–8596.
184 Y. Zhao, W. Ma, Y. Xu, C. Zhang, Q. Wang, T. Yang, X. Gao, F. Wang, C. Yan and J.-X. Jiang, *Macromolecules*, 2018, **51**, 9502–9508.
185 R. S. Sprick, Y. Bai, A. A. Y. Guilbert, M. Zbiri, C. M. Aitchison, L. Wilbraham, Y. Yan, D. J. Woods, M. A. Zwijnenburg and A. I. Cooper, *Chem. Mater.*, 2019, **31**, 305–313.
186 Y. Zhang, Y. Zhang, Y. L. Sun, X. Du, J. Y. Shi, W. Wang and W. D. Wang, *Chem. - A Eur. J.*, 2012, **18**, 6328–6334.
187 F. Wei, X. Cai, J. Nie, F. Wang, C. Lu, G. Yang, Z. Chen, C. Ma and Y. Zhang, *Polym. Chem.*, 2018, **9**, 3832–3839.
188 D. Y. Kim, T. J. Choi, J. G. Kim and J. Y. Chang, *ACS Omega*, 2018, **3**, 8745–8751.
189 J. G. Kim, M. C. Cha, J. Lee, T. Choi and J. Y. Chang, *ACS Appl. Mater. Interfaces*, 2017, **9**, 38081–38088.
190 S. Katiyar, K. Mondal and A. Sharma, *RSC Adv.*, 2016, **6**, 12298–12310.
191 C. Broicher, S. R. Foit, M. Rose, P. J. C. Hausoul and R. Palkovits, *ACS Catal.*, 2017, **7**, 8413–8419.
192 J.-X. Jiang, C. Wang, A. Laybourn, T. Hasell, R. Clowes, Y. Z. Khimyak, J. Xiao, S. J. Higgins, D. J. Adams and A. I. Cooper, *Angew. Chem. Int. Ed.*, 2011, **50**, 1072–1075.
193 F. M. Wisser, Y. Mohr, E. A. Quadrelli, D. Farrusseng and J. Canivet, *ChemCatChem*, 2018, **10**, 1778–1782.
194 L. Chen, Y. Yang and D. Jiang, *J. Am. Chem. Soc.*, 2010, **132**, 9138–9143.
195 L. Chen, Y. Yang, Z. Guo and D. Jiang, *Adv. Mater.*, 2011, **23**, 3149–3154.
196 T.-T. Liu, Z.-J. Lin, P.-C. Shi, T. Ma, Y.-B. Huang and R. Cao, *ChemCatChem*, 2015, **7**, 2340–2345.
197 K. Zhang, O. K. Farha, J. T. Hupp and S. B. T. Nguyen, *ACS Catal.*, 2015, **5**, 4859–4866.
198 K. Cho, S. M. Lee, H. J. Kim, Y.-J. Ko and S. U. Son, *J. Mater. Chem. A*, 2018, **6**, 15553–15557.
199 S. Mondal, J. Mondal and A. Bhaumik, *ChemCatChem*, 2015, **7**, 3570–3578.
200 K. Cho, J. Yoo, H. W. Noh, S. M. Lee, H. J. Kim, Y. J. Ko, H. Y. Jang and S. U. Son, *J. Mater. Chem. A*, 2017, **5**, 8922–8926.
201 M. Du, A. M. Agrawal, S. Chakraborty, S. J. Garibay, R. Limvorapitux, B. Choi, S. T. Madrahimov and S. T. Nguyen, *ACS Sustain. Chem. Eng.*, 2019, **7**, 8126–8135.
202 Y.-B. Zhou, Y.-Q. Wang, L.-C. Ning, Z.-C. Ding, W.-L. Wang, C.-K. Ding, R.-H. Li, J.-J. Chen, X. Lu, Y.-J. Ding and Z.-P. Zhan, *J. Am. Chem. Soc.*, 2017, **139**, 3966–3969.
203 C.-A. Wang, K. Nie, G.-D. Song, Y.-W. Li and Y.-F. Han, *RSC Adv.*, 2019, **9**, 8239–8245.
204 R.-H. Li, Z.-C. Ding, C.-Y. Li, J.-J. Chen, Y.-B. Zhou, X.-M. An, Y.-J. Ding and Z.-P. Zhan, *Org. Lett.*, 2017, **19**, 4432–4435.
205 P. Zhang, Z. Weng, J. Guo and C. Wang, *Chem. Mater.*, 2011, **23**, 5243–5249.
206 X. Liu, S. A, Y. Zhang, X. Luo, H. Xia, H. Li and Y. Mu, *RSC Adv.*, 2014, **4**, 6447–6453.
207 Y. Xie, T.-T. Wang, X.-H. Liu, K. Zou and W.-Q. Deng, *Nat. Commun.*, 2013, **4**, 1960.
208 Y. Xie, R.-X. Yang, N.-Y. Huang, H.-J. Luo and W.-Q. Deng, *J. Energy Chem.*, 2014, **23**, 22–28.
209 X. Sheng, H. Guo, Y. Qin, X. Wang and F. Wang, *RSC Adv.*, 2015, **5**, 31664–31669.
210 D. S. Kundu, J. Schmidt, C. Bleschke, A. Thomas and S. Blechert, *Angew. Chem. Int. Ed.*, 2012, **51**, 5456–5459.
211 L. Ma, M. M. Wanderley and W. Lin, *ACS Catal.*, 2011, **1**, 691–697.
212 P. Mu, H. Sun, Z. Zhu, W. Liang, J. Liu and A. Li, *Macromol. Mater. Eng.*, 2016, **301**, 451–456.
213 J. Zang, Z. Zhu, P. Mu, H. Sun, W. Liang, F. Yu, L. Chen and A. Li, *Macromol. Mater. Eng.*, 2016, **301**, 1104–1110.
214 R.-X. Yang, T.-T. Wang and W.-Q. Deng, *Sci. Rep.*, 2015, **5**, 10155.
215 H. Plenio, *Chem. Rev.*, 1997, **97**, 3363–3384.
216 H. Takemura, S. Nakashima, N. Kon, M. Yasutake, T. Shinmyozu and T. Inazu, *J. Am. Chem. Soc.*, 2001, **123**, 9293–9298.
217 R. Xiao, J. M. Tobin, M. Zha, Y.-L. Hou, J. He, F. Vilela and Z. Xu, *J. Mater. Chem. A*, 2017, **5**, 20180–20187.
218 Y. Yang, Z. Yan, L. Wang, Q. Meng, Y. Yuan and G. Zhu, *J. Mater. Chem. A*, 2018, **6**, 5202–5207.

219 J. H. Ko, S. M. Lee, H. J. Kim, Y.-J. Ko and S. U. Son, *ACS Macro Lett.*, 2018, **7**, 1353–1358.

220 Y. Yuan, Y. Yang, X. Ma, Q. Meng, L. Wang, S. Zhao and G. Zhu, *Adv. Mater.*, 2018, **30**, 1–7.

221 G. Steinhauser, *Environ. Sci. Technol.*, 2014, **48**, 4649–4663.

222 J. Huve, A. Ryzhikov, H. Nouali, V. Lalia, G. Augé and T. J. Daou, *RSC Adv.*, 2018, **8**, 29248–29273.

223 W. Xie, D. Cui, S.-R. Zhang, Y. Xu and D. Jiang, *Mater. Horizons*, 2019, **6**, 1571–1595.

224 Y. Zhu, Y.-J. Ji, D.-G. Wang, Y. Zhang, H. Tang, X. R. Jia, M. Song, G. Yu and G.-C. Kuang, *J. Mater. Chem. A*, 2017, **5**, 6622–6629.

225 Y. Liao, J. Weber, B. M. Mills, Z. Ren and C. F. J. Faul, *Macromolecules*, 2016, **49**, 6322–6333.

226 P. Politzer, J. S. Murray and T. Clark, *Phys. Chem. Chem. Phys.*, 2013, **15**, 11178–11189.

227 J. P. M. Lommerse, A. J. Stone, R. Taylor and F. H. Allen, *J. Am. Chem. Soc.*, 1996, **118**, 3108–3116.

228 T. Geng, Z. Zhu, W. Zhang and Y. Wang, *J. Mater. Chem. A*, 2017, **5**, 7612–7617.

229 F. Ren, Z. Zhu, X. Qian, W. Liang, P. Mu, H. Sun, J. Liu and A. Li, *Chem. Commun.*, 2016, **52**, 9797–9800.

230 X. Qian, Z.-Q. Zhu, H. X. Sun, F. Ren, P. Mu, W. Liang, L. Chen and A. Li, *ACS Appl. Mater. Interfaces*, 2016, **8**, 21063–21069.

231 S. A, Y. Zhang, Z. Li, H. Xia, M. Xue, X. Liu and Y. Mu, *Chem. Commun.*, 2014, **50**, 8495–8498.

232 I. Ali, *Chem. Rev.*, 2012, **112**, 5073–5091.

233 W.-K. Meng, L. Liu, X. Wang, R.-S. Zhao, M.-L. Wang and J.-M. Lin, *Anal. Chim. Acta*, 2018, **1015**, 27–34.

234 R. Jiao, L. Bao, W. Zhang, H. Sun, Z. Zhu, C. Xiao, L. Chen and L. An, *New J. Chem.*, 2018, **42**, 14863–14869.

235 A. Li, H.-X. Sun, D.-Z. Tan, W.-J. Fan, S.-H. Wen, X.-J. Qing, G.-X. Li, S.-Y. Li and W.-Q. Deng, *Energy Environ. Sci.*, 2011, **4**, 2062–2065.

236 D. Tan, W. Xiong, H. Sun, Z. Zhang, W. Ma, C. Meng, W. Fan and A. Li, *Microporous Mesoporous Mater.*, 2013, **176**, 25–30.

237 D. Tan, W. Fan, W. Xiong, H. Sun, A. Li, W. Deng and C. Meng, *Eur. Polym. J.*, 2012, **48**, 705–711.

238 D. Tan, W. Fan, W. Xiong, H. Sun, Y. Cheng, X. Liu, C. Meng, A. Li and W.-Q. Deng, *Macromol. Chem. Phys.*, 2012, **213**, 1435–1440.

239 W.-J. Fan, G.-J. Yang, J.-W. Chi, Y. Yu and D.-Z. Tan, *RSC Adv.*, 2016, **6**, 54841–54847.

240 Y. Lim, M. C. Cha and J. Y. Chang, *Sci. Rep.*, 2015, **5**, 15957.

241 R. Du, N. Zhang, H. Xu, N. Mao, W. Duan, J. Wang, Q. Zhao, Z. Liu and J. Zhang, *Adv. Mater.*, 2014, **26**, 8053–8058.

242 R. Du, Z. Zheng, N. Mao, N. Zhang, W. Hu and J. Zhang, *Adv. Sci.*, 2015, **2**, 1400006.

243 Z. Xiao, M. Zhang, W. Fan, Y. Qian, Z. Yang, B. Xu, Z. Kang, R. Wang and D. Sun, *Chem. Eng. J.*, 2017, **326**, 640–646.

244 X. Sen Wang, J. Liu, J. M. Bonefont, D.-Q. Yuan, P. K. Thallapally and S. Ma, *Chem. Commun.*, 2013, **49**, 1533–1535.

245 Y. Liu, Y. Cui, C. Zhang, J. Du, S. Wang, Y. Bai, Z. Liang and X. Song, *Chem. - A Eur. J.*, 2018, **24**, 7480–7488.

246 J. H. Wang, Y. Zhang, L. C. An, W. H. Wang, Y. H. Zhang and X. H. Bu, *Chinese J. Chem.*, 2018, **36**, 826–830.

247 S.-J. Yang, X. Ding and B.-H. Han, *Macromolecules*, 2018, **51**, 947–953.

248 L. Zhou, Y. Hu and G. Li, *Anal. Chem.*, 2016, **88**, 6930–6938.

249 W. Yang, X. Wu, T. Liu, T. Wang and X. Hou, *Analyst*, 2018, **143**, 5744–5753.

250 Y. Peng, M. Huang, Y. Hu, G. Li and L. Xia, *J. Chromatogr. A*, 2019, **1594**, 45–53.

251 J.-Q. Ma, L. Liu, X. Wang, L.-Z. Chen, J.-M. Lin and R.-S. Zhao, *J. Hazard. Mater.*, 2019, **371**, 433–439.

252 H. Lei, Y. Hu and G. Li, *J. Chromatogr. A*, 2018, **1580**, 22–29.

253 F. Wang, F. Ren, P. Mu, Z. Zhu, H. Sun, C. Ma, C. Xiao, W. Liang, L. Chen and A. Li, *J. Mater. Chem. A*, 2017, **5**, 11348–11356.

254 X. Liu, Y. Xu, Z. Guo, A. Nagai and D. Jiang, *Chem. Commun.*, 2013, **49**, 3233–3235.

255 X. Shen, M. Faheem, Y. Matsuo, S. Aziz, X. Zhang, Y. Li, J. Song, Y. Tian and G. Zhu, *J. Mater. Chem. A*, 2019, **7**, 2507–2512.

256 R. Zhao, T. Ma, S. Li, Y. Tian and G. Zhu, *ACS Appl. Mater. Interfaces*, 2019, **11**, 16662–16673.

257 P. Markewitz, W. Kuckshinrichs, W. Leitner, J. Linssen, P. Zapp, R. Bongartz, A. Schreiber and T. E. Müller, *Energy Environ. Sci.*, 2012, **5**, 7281–7305.

258 B. Dutcher, M. Fan and A. G. Russell, *ACS Appl. Mater. Interfaces*, 2015, **7**, 2137–2148.

259 G. Kupgan, L. J. Abbott, K. E. Hart and C. M. Colina, *Chem. Rev.*, 2018, **118**, 5488–5538.

260 J. R. Holst and A. I. Cooper, *Adv. Mater.*, 2010, **22**, 5212–5216.

261 C. Xu and N. Hedin, *Mater. Today*, 2014, **17**, 397–403.

262 M. Oschatz and M. Antonietti, *Energy Environ. Sci.*, 2018, **11**, 57–70.

263 Z.-W. Liu and B.-H. Han, *Curr. Opin. Green Sustain. Chem.*, 2019, **16**, 20–25.

264 K. Sumida, D. L. Rogow, J. A. Mason, T. M. McDonald, E. D. Bloch, Z. R. Herm, T.-H. Bae and J. R. Long, *Chem. Rev.*, 2012, **112**, 724–781.

265 N. Huang, G. Day, X. Yang, H. Drake and H.-C. Zhou, *Sci. China Chem.*, 2017, **60**, 1007–1014.

266 L. Zou, Y. Sun, S. Che, X. Yang, X. Wang, M. Bosch, Q. Wang, H. Li, M. Smith, S. Yuan, Z. Perry and H. C. Zhou, *Adv. Mater.*, 2017, **29**, 1–35.

267 R. Dawson, A. I. Cooper and D. J. Adams, *Polym. Int.*, 2013, **62**, 345–352.

268 R. Dawson, D. J. Adams and A. I. Cooper, *Chem. Sci.*, 2011, **2**, 1173–1177.

269 C. Zhang, X. Yang, Y. Zhao, X. Wang, M. Yu and J.-X. Jiang, *Polymer*, 2015, **61**, 36–41.

270 X. Wang, Y. Zhao, L. Wei, C. Zhang, X. Yang, M. Yu and J.-X. Jiang, *Macromol. Chem. Phys.*, 2015, **216**, 504–510.

271 Y. Zhang, A. Sigen, Y. Zou, X. Luo, Z. Li, H. Xia, X. Liu and Y. Mu, *J. Mater. Chem. A*, 2014, **2**, 13422–13430.

272 Y. Yuan, H. Huang, L. Chen and Y. Chen, *Macromolecules*, 2017, **50**, 4993–5003.

273 C. Li, P. Li, L. Chen, M. E. Briggs, M. Liu, K. Chen, X. Shi, D. Han and S. Ren, *J. Polym. Sci. Part A Polym. Chem.*, 2017, **55**, 2383–2389.

274 C.-J. Sun, P. F. Wang, H. Wang and B.-H. Han, *Polym. Chem.*, 2016, **7**, 5031–5038.

275 Y. Xu, D. Cui, S. Zhang, G. Xu and Z. Su, *Polym. Chem.*, 2019, **10**, 819–822.

276 K. C. Park, J. Cho and C. Y. Lee, *RSC Adv.*, 2016, **6**, 75478–75481.

277 X. Wang, Y. Zhao, L. Wei, C. Zhang and J.-X. Jiang, *J. Mater. Chem. A*, 2015, **3**, 21185–21193.

278 L. Qin, G.-J. Xu, C. Yao and Y.-H. Xu, *Polym. Chem.*, 2016, **7**, 4599–4602.

279 D. Cui, C. Yao and Y. Xu, *Chem. Commun.*, 2017, **53**, 11422–11425.

280 Y. Liao, Z. Cheng, M. Trunk and A. Thomas, *Polym. Chem.*, 2017, **8**, 7240–7247.

281 A. Bhunia, D. Esquivel, S. Dey, R. Fernández-Terán, Y. Goto, S. Inagaki, P. Van Der Voort and C. Janiak, *J. Mater. Chem. A*, 2016, **4**, 13450–13457.

282 Z. Li, H. Li, H. Xia, X. Ding, X. Luo, X. Liu and Y. Mu, *Chem. - A Eur. J.*, 2015, **21**, 17355–17362.

283 S.-B. Ren, P.-X. Li, A. Stephenson, L. Chen, M. E. Briggs, R. Clowes, A. Alahmed, K.-K. Li, W.-P. Jia and D.-M. Han, *Ind. Eng. Chem. Res.*, 2018, **57**, 9254–9260.

284 A. Bhunia, V. Vasylyeva and C. Janiak, *Chem. Commun.*, 2013, **49**, 3961–3963.

285 Q. Chen, D.-P. Liu, J.-H. Zhu and B.-H. Han, *Macromolecules*, 2014, **47**, 5926–5931.

286 Y. Liao, J. Weber and C. F. J. Faul, *Chem. Commun.*, 2014, **50**, 8002–8005.

287 A. K. Sekizkardes, J. T. Culp, T. Islamoglu, A. Marti, D. Hopkinson, C. Myers, H. M. El-Kaderi and H. B. Nulwala, *Chem. Commun.*, 2015, **51**, 13393–13396.

288 R. Yuan, H. Ren, Z. Yan, A. Wang and G. Zhu, *Polym. Chem.*, 2014, **5**, 2266–2272.

289 P. Arab, A. Verlander and H. M. El-Kaderi, *J. Phys. Chem. C*, 2015, **119**, 8174–8182.

290 S. Altarawneh, T. Islamoɨlu, A. K. Sekizkardes and H. M. El-Kaderi, *Environ. Sci. Technol.*, 2015, **49**, 4715–4723.

291 A. K. Sekizkardes, S. Altarawneh, Z. Kahveci, T. Islamoɨlu and H. M. El-Kaderi, *Macromolecules*, 2014, **47**, 8328–8334.

292 A. K. Sekizkardes, T. Islamoğlu, Z. Kahveci and H. M. El-Kaderi, *J. Mater. Chem. A*, 2014, **2**, 12492–12500.

293 T. Islamoglu, T. Kim, Z. Kahveci, O. M. El-Kadri and H. M. El-Kaderi, *J. Phys. Chem. C*, 2016, **120**, 2592–2599.

294 P. Arab, E. Parrish, T. İslamoğlu and H. M. El-Kaderi, *J. Mater. Chem. A*, 2015, **3**, 20586–20594.

295 S. Mane, Y. X. Li, X. Q. Liu, M. B. Yue and L.-B. Sun, *ACS Sustain. Chem. Eng.*, 2018, **6**, 17419–17426.

296 I. Sreedhar, K. M. Kamani, B. M. Kamani, B. M. Reddy and A. Venugopal, *Renew. Sustain. Energy Rev.*, 2018, **91**, 838–860.

297 Y. H. Hu and L. Zhang, *Adv. Mater.*, 2010, **22**, 117–130.

298 J. Germain, J. M. J. Fréchet and F. Svec, *Small*, 2009, **5**, 1098–1111.

299 K. Cousins and R. Zhang, *Polymers*, 2019, **11**, 690.

300 D. P. Broom, C. J. Webb, G. S. Fanourgakis, G. E. Froudakis, P. N. Trikalitis and M. Hirscher, *Int. J. Hydrogen Energy*, 2019, **44**, 7768–7779.

301 J. X. Jiang, F. Su, H. Niu, C. D. Wood, N. L. Campbell, Y. Z. Khimyak and A. I. Cooper, *Chem. Commun.*, 2008, **8**, 486–488.

302 Q. Liu, G. Li, Z. Tang, L. Chen, B. Liao, B. Ou, Z. Zhou and H. Zhou, *Mater. Chem. Phys.*, 2017, **186**, 11–18.

303 A. Li, R.-F. Lu, Y. Wang, X. Wang, K.-L. Han and W.-Q. Deng, *Angew. Chem. Int. Ed.*, 2010, **49**, 3330–3333.

304 K. Srinivasu and S. K. Ghosh, *RSC Adv.*, 2014, **4**, 4170–4176.

305 K. R. S. Chandrakumar and S. K. Ghosh, *Chem. Phys. Lett.*, 2007, **447**, 208–214.

306 K. Srinivasu, K. R. S. Chandrakumar and S. K. Ghosh, *ChemPhysChem*, 2009, **10**, 427–435.

307 D. Xu, L. Sun, G. Li, J. Shang, R.-X. Yang and W.-Q. Deng, *Chem. - A Eur. J.*, 2016, **22**, 7944–7949.

308 Z. Xiang, D. Cao, W. Wang, W. Yang, B. Han and J. Lu, *J. Phys. Chem. C*, 2012, **116**, 5974–5980.

309 Q. Chen, M. Luo, T. Wang, J. X. Wang, D. Zhou, Y. Han, C. S. Zhang, C. G. Yan and B. H. Han, *Macromolecules*, 2011, **44**, 5573–5577.

310 M. G. Rabbani, A. K. Sekizkardes, O. M. El-Kadri, B. R. Kaafarani and H. M. El-Kaderi, *J. Mater. Chem.*, 2012, **22**, 25409–25417.

311 Q. Chen, J.-X. Wang, F. Yang, D. Zhou, N. Bian, X.-J. Zhang, C.-G. Yan and B.-H. Han, *J. Mater. Chem.*, 2011, **21**, 13554–13560.

312 J. Li, L. Huang, X. Zou, A. Zheng, H. Li, H. Rong and G. Zhu, *J. Mater. Chem. A*, 2018, **6**, 11163–11168.

313 D. Chen, C. Liu, J. Tang, L. Luo and G. Yu, *Polym. Chem.*, 2019, **10**, 1168–1181.

314 Q. Zhang, S. Yu, Q. Wang, Q. Xiao, Y. Yue and S. Ren, *Macromol. Rapid Commun.*, 2017, **38**, 1700445.

315 T.-M. Geng, D.-K. Li, Z.-M. Zhu, Y.-B. Guan and Y. Wang, *Microporous Mesoporous Mater.*, 2016, **231**, 92–99.

316 T.-M. Geng, D.-K. Li, Z. M. Zhu, W.-Y. Zhang, S.-N. Ye, H. Zhu and Z.-Q. Wang, *Anal. Chim. Acta*, 2018, **1011**, 77–85.

317 S. Krishnan and C. V. Suneesh, *J. Photochem. Photobiol. A Chem.*, 2019, **371**, 414–422.

318 T. Geng, Z. Zhu, X. Wang, H. Xia, Y. Wang and D. Li, *Sensors Actuators, B Chem.*, 2017, **244**, 334–343.

319 C. Gu, N. Huang, Y. Wu, H. Xu and D. Jiang, *Angew. Chem. Int. Ed.*, 2015, **54**, 11540–11544.

320 H. Namgung, J. J. Lee, Y. J. Gwon and T. S. Lee, *RSC Adv.*, 2018, **8**, 34291–34296.

321 V. S. Mothika, A. Räupke, K. O. Brinkmann, T. Riedl, G. Brunklaus and U. Scherf, *ACS Appl. Nano Mater.*, 2018, **1**, 6483–6492.

322 N. Park, K. C. Ko, H.-W. Shin, S. M. Lee, H. J. Kim, J. Y. Lee and S. U. Son, *J. Mater. Chem. A*, 2016, **4**, 8010–8014.

323 S. Bhunia, N. Dey, A. Pradhan and S. Bhattacharya, *Chem. Commun.*, 2018, **54**, 7495–7498.

324 P. Zhao, Y. Wu, C. Feng, L. Wang, Y. Ding and A. Hu, *Anal. Chem.*, 2018, **90**, 4815–4822.

325 M. Liu, C. Yao, C. Liu and Y. Xu, *Sci. Rep.*, 2018, **8**, 14072.

326 M. Liu, C. Yao, C. Liu and Y. Xu, *Sci. Rep.*, 2018, **8**, 14071.

327 S.-Y. Ding, M. Dong, Y.-W. Wang, Y. T. Chen, H.-Z. Wang, C.-Y. Su and W. Wang, *J. Am. Chem. Soc.*, 2016, **138**, 3031–3037.

328 N. Huang, L. Zhai, H. Xu and D. Jiang, *J. Am. Chem. Soc.*, 2017, **139**, 2428–2434.

329 Z. Li, Y. Zhang, H. Xia, Y. Mu and X. Liu, *Chem. Commun.*, 2016, **52**, 6613–6616.

330 T. Wang, R. Xue, H. Chen, P. Shi, X. Lei, Y. Wei, H. Guo and W. Yang, *New J. Chem.*, 2017, **41**, 14272–14278.

331 W.-R. Cui, C.-R. Zhang, W. Jiang, R.-P. Liang, S.-H. Wen, D. Peng and J.-D. Qiu, *ACS Sustain. Chem. Eng.*, 2019, **7**, 9408–9415.

332 G. Chen, H.-H. Lan, S.-L. Cai, B. Sun, X.-L. Li, Z.-H. He, S.-R. Zheng, J. Fan, Y. Liu and W.-G. Zhang, *ACS Appl. Mater. Interfaces*, 2019, **11**, 12830–12837.

333 C. Zhang, S. Zhang, Y. Yan, F. Xia, A. Huang and Y. Xian, *ACS Appl. Mater. Interfaces*, 2017, **9**, 13415–13421.

334 M. R. Rao, Y. Fang, S. De Feyter and D. F. Perepichka, *J. Am. Chem. Soc.*, 2017, **139**, 2421–2427.

335 G. Das, B. P. Biswal, S. Kandambeth, V. Venkatesh, G. Kaur, M. Addicoat, T. Heine, S. Verma and R. Banerjee, *Chem. Sci.*, 2015, **6**, 3931–3939.

336 L. Ascherl, E. W. Evans, M. Hennemann, D. Di Nuzzo, A. G. Hufnagel, M. Beetz, R. H. Friend, T. Clark, T. Bein and F. Auras, *Nat. Commun.*, 2018, **9**, 3802.

337 Y. Peng, Y. Huang, Y. Zhu, B. Chen, L. Wang, Z. Lai, Z. Zhang, M. Zhao, C. Tan, N. Yang, F. Shao, Y. Han and H. Zhang, *J. Am. Chem. Soc.*, 2017, **139**, 8698–8704.

338 M. Wang, M. Hu, J. Liu, C. Guo, D. Peng, Q. Jia, L. He, Z. Zhang and M. Du, *Biosens. Bioelectron.*, 2019, **132**, 8–16.

339 F.-Z. Cui, J.-J. Xie, S.-Y. Jiang, S.-X. Gan, D.-L. Ma, R.-R. Liang, G.-F. Jiang and X. Zhao, *Chem. Commun.*, 2019, **55**, 4550–4553.

340 R. Xue, H. Guo, T. Wang, L. Gong, Y. Wang, J. Ai, D. Huang, H. Chen and W. Yang, *Anal. Methods*, 2017, **9**, 3737–3750.

341 P. Samanta, A. V. Desai, S. Let and S. K. Ghosh, *ACS Sustain. Chem. Eng.*, 2019, **7**, 7456–7478.

342 A. P. Cote, A. I. Benin, N. W. Ockwig, M. O'Keeffe, A. J. Matzger and O. M. Yaghi, *Science*, 2005, **310**, 1166–1170.

343 J. Liu, K.-K. Yee, K. K.-W. Lo, K. Y. Zhang, W. P. To, C.-M. Che and Z. Xu, *J. Am. Chem. Soc.*, 2014, **136**, 2818–2824.

344 X.-P. Zhou, Z. Xu, M. Zeller and A. D. Hunter, *Chem. Commun.*, 2009, 5439.

345 J. He, K.-K. Yee, Z. Xu, M. Zeller, A. D. Hunter, S. S.-Y. Chui and C.-M. Che, *Chem. Mater.*, 2011, **23**, 2940–2947.

346 K.-K. Yee, N. Reimer, J. Liu, S.-Y. Cheng, S.-M. Yiu, J. Weber, N. Stock and Z. Xu, *J. Am. Chem. Soc.*, 2013, **135**, 7795–7798.

347 Y.-L. Hou, K. K. Yee, Y.-L. Wong, M. Zha, J. He, M. Zeller, A. D. Hunter, K. Yang and Z. Xu, *J. Am. Chem. Soc.*, 2016, **138**, 14852–14855.

348 Y. He, M. Huang, X. Deng, C. Shengxian, Y.-L. Wong, Y.-L. Hou, J. He, M. Zeller and Z. Xu, *Chem. Commun.*, 2019, **55**, 5091–5094.

349 M. Mon, F. Lloret, J. Ferrando-Soria, C. Martí-Gastaldo, D. Armentano and E. Pardo, *Angew. Chem. Int. Ed.*, 2016, **55**, 11167–11172.

350 X. Wu, X. Han, Q. Xu, Y. Liu, C. Yuan, S. Yang, Y. Liu, J. Jiang and Y. Cui, *J. Am. Chem. Soc.*, 2019, **141**, 7081–7089.

351 J.-S. M. Lee, T.-H. Wu, B. M. Alston, M. E. Briggs, T. Hasell, C.-C. Hu and A. I. Cooper, *J. Mater. Chem. A*, 2016, **4**, 7665–7673.

352 X.-C. Li, Y. Zhang, C.-Y. Wang, Y. Wan, W.-Y. Lai, H. Pang and W. Huang, *Chem. Sci.*, 2017, **8**, 2959–2965.

353 S. Chai, N. Hu, Y. Han, X. Zhang, Z. Yang, L. Wei, L. Wang and H. Wei, *RSC Adv.*, 2016, **6**, 49425–49428.

354 H. Zhang, Y. Zhang, C. Gu and Y. Ma, *Adv. Energy Mater.*, 2015, **5**, 1402175.

355 X. Feng, Y. Liang, L. Zhi, A. Thomas, D. Wu, I. Lieberwirth, U. Kolb and K. Müllen, *Adv. Funct. Mater.*, 2009, **19**, 2125–2129.

356 Y. Zhao, F. Xie, C. Zhang, R. Kong, S. Feng and J.-X. Jiang, *Microporous Mesoporous Mater.*, 2017, **240**, 73–79.

357 Y. Xu, S. Wu, S. Ren, J. Ji, Y. Yue and J. Shen, *RSC Adv.*, 2017, **7**, 32496–32501.

358 H. Wang, Z. Cheng, Y. Liao, J. Li, J. Weber, A. Thomas and C. F. J. Faul, *Chem. Mater.*, 2017, **29**, 4885–4893.

359 A. C. Lim, H. S. Jadhav and J. G. Seo, *Dalt. Trans.*, 2018, **47**, 852–858.

360 M. E. Bhosale, R. Illathvalappil, S. Kurungot and K. Krishnamoorthy, *Chem. Commun.*, 2016, **52**, 316–318.

361 Y. Li, S. Zheng, X. Liu, P. Li, L. Sun, R. Yang, S. Wang, Z.-S. Wu, X. Bao and W.-Q. Deng, *Angew. Chem. Int. Ed.*, 2018, **57**, 7992–7996.

362 J. Choi, J. H. Ko, C. W. Kang, S. M. Lee, H. J. Kim, Y.-J. Ko, M. Yang and S. U. Son, *J. Mater. Chem. A*, 2018, **6**, 6233–6237.

363 M. Li, J. Lu, Z. Chen and K. Amine, *Adv. Mater.*, 2018, **30**, 1800561.

364 G. Li, J.-F. Yin, H. Guo, Z. Wang, Y. Zhang, X. Li, J. Wang, Z. Yin and G.-C. Kuang, *ACS Omega*, 2018, **3**, 7727–7735.

365 W. Wei, G. Chang, Y. Xu and L. Yang, *J. Mater. Chem. A*, 2018, **6**, 18794–18798.

366 F. Xu, X. Chen, Z. Tang, D. Wu, R. Fu and D. Jiang, *Chem. Commun.*, 2014, **50**, 4788–4790.

367 J. Wang, Y. Lee, K. Tee, S. N. Riduan and Y. Zhang, *Chem. Commun.*, 2018, **54**, 7681–7684.

368 C. Zhang, Y. He, P. Mu, X. Wang, Q. He, Y. Chen, J. Zeng, F. Wang, Y. Xu and J.-X. Jiang, *Adv. Funct. Mater.*, 2018, **28**, 1705432.

369 J. Y. Hwang, S. T. Myung and Y. K. Sun, *Chem. Soc. Rev.*, 2017, **46**, 3529–3614.

370 C. Zhang, Y. Qiao, P. Xiong, W. Ma, P. Bai, X. Wang, Q. Li, J. Zhao, Y. Xu, Y. Chen, J. H. Zeng, F. Wang, Y. Xu and J.-X. Jiang, *ACS Nano*, 2019, **13**, 745–754.

371 A. A. Gewirth, J. A. Varnell and A. M. Diascro, *Chem. Rev.*, 2018, **118**, 2313–2339.

372 X. Zhuang, F. Zhang, D. Wu, N. Forler, H. Liang, M. Wagner, D. Gehrig, M. R. Hansen, F. Laquai and X. Feng, *Angew. Chem. Int. Ed.*, 2013, **52**, 9668–9672.

373 X. Zhuang, D. Gehrig, N. Forler, H. Liang, M. Wagner, M. R. Hansen, F. Laquai, F. Zhang and X. Feng, *Adv. Mater.*, 2015, **27**, 3789–3796.

374 S. Bhattacharyya, D. Samanta, S. Roy, V. P. H. Radhakantha

and T. K. Maji, *ACS Appl. Mater. Interfaces*, 2019, **11**, 5455–5461.
375 P. Mu, W. Bai, Z. Zhang, J. He, H. Sun, Z. Zhu, W. Liang and A. Li, *J. Mater. Chem. A*, 2018, **6**, 18183–18190.
376 X. Lin, J. Chen, Z. Yuan, M. Yang, G. Chen, D. Yu, M. Zhang, W. Hong and X. Chen, *J. Mater. Chem. A*, 2018, **6**, 4642–4648.
377 J. Chen, J. Feng, Z. Li, P. Xu, X. Wang, W. Yin, M. Wang, X. Ge and Y. Yin, *Nano Lett.*, 2019, **19**, 400–407.
378 L. Sun, Z. Li, R. Su, Y. Wang, Z. Li, B. Du, Y. Sun, P. Guan, F. Besenbacher and M. Yu, *Angew. Chem. Int. Ed.*, 2018, **57**, 10666–10671.
379 T. Li, Q. Fang, X. Xi, Y. Chen and F. Liu, *J. Mater. Chem. A*, 2019, **7**, 586–593.
380 P. Mu, H. Sun, Z. Zhu, J. He, W. Liang and A. Li, *J. Mater. Chem. A*, 2018, **6**, 11676–11681.
381 C. Zhu, R. T. K. Kwok, J. W. Y. Lam and B. Z. Tang, *ACS Appl. Bio Mater.*, 2018, **1**, 1768–1786.
382 Y. Xu, A. Nagai and D. Jiang, *Chem. Commun.*, 2013, **49**, 1591–1593.
383 J. Brandt, J. Schmidt, A. Thomas, J. D. Epping and J. Weber, *Polym. Chem.*, 2011, **2**, 1950–1952.
384 B. Bonillo, R. S. Sprick and A. I. Cooper, *Chem. Mater.*, 2016, **28**, 3469–3480.
385 Y. Yuan, W. Chen, Z. Ma, Y. Deng, Y. Chen, Y. Chen and W. Hu, *Chem. Sci.*, 2019, **10**, 2206–2211.
386 J.-M. Lehn, *From Molecular to Supramolecular Chemistry*, Wiley-VCH Verlag GmbH & Co. KGaA, Weinheim, 2006.
387 L. Xu and Y. Li, *Sci. Rep.*, 2016, **6**, 28784.
388 R. Zhao, J. Han, M. Huang, F. Liu, L. Wang and Y. Ma, *Macromol. Rapid Commun.*, 2017, **38**, 1700274.
389 E. Busseron, J. Lux, M. Degardin and J. Rebek, *Chem. Commun.*, 2013, **49**, 4842–4844.
390 F. A. Arroyave and P. Ballester, *J. Org. Chem.*, 2015, **80**, 10866–10873.
391 L. Osorio-Planes, M. Espelt, M. A. Pericàs and P. Ballester, *Chem. Sci.*, 2014, **5**, 4260–4264.
392 L. Chen, Y. Honsho, S. Seki and D. Jiang, *J. Am. Chem. Soc.*, 2010, **132**, 6742–6748.
393 K. Venkata Rao, R. Haldar, T. K. Maji and S. J. George, *Phys. Chem. Chem. Phys.*, 2016, **18**, 156–163.
394 K. V. Rao, S. Mohapatra, T. K. Maji and S. J. George, *Chem. - A Eur. J.*, 2012, **18**, 4505–4509.
395 P. Zhang, K. Wu, J. Guo and C. Wang, *ACS Macro Lett.*, 2014, **3**, 1139–1144.
396 V. M. Suresh, S. Bonakala, S. Roy, S. Balasubramanian and T. K. Maji, *J. Phys. Chem. C*, 2014, **118**, 24369–24376.
397 S. N. Talapaneni, D. Kim, G. Barin, O. Buyukcakir, S. H. Je and A. Coskun, *Chem. Mater.*, 2016, **28**, 4460–4466.
398 X. Li, Z. Li and Y.-W. Yang, *Adv. Mater.*, 2018, **30**, 1800177.
399 Z. Xu, S. Lee, Y.-H. Kiang, A. B. Mallik, N. Tsomaia and K. T. Mueller, *Adv. Mater.*, 2001, **13**, 637–641.
400 Y.-L. Hou, M.-Q. Li, S. Cheng, Y. Diao, F. Vilela, Y. He, J. He and Z. Xu, *Chem. Commun.*, 2018, **54**, 9470–9473.
401 J. He, S. Cheng and Z. Xu, *Chem. – A Eur. J.*, 2019, **25**, 8654–8662.
402 S.-J. Yang, X. Ding and B.-H. Han, *Langmuir*, 2018, **34**, 7640–7646.
403 H. Wei, F. Wang, H. Sun, Z. Zhu, C. Xiao, W. Liang, B. Yang, L. Chen and A. Li, *J. Mater. Chem. A*, 2018, **6**, 8633–8642.
404 F. Wang, W. Liang, X. Qian, C. Ma, A. Li, H. Wei, Z. Hu, H. Sun, Z. Zhu and S. Li, *Chem. Eng. J.*, 2018, **351**, 856–866.
405 A. Singh, D. Samanta, M. Boro and T. K. Maji, *Chem. Commun.*, 2019, **55**, 2837–2840.
406 A. Singh, S. Roy, C. Das, D. Samanta and T. K. Maji, *Chem. Commun.*, 2018, **54**, 4465–4468.
407 S. Roy, A. Bandyopadhyay, M. Das, P. P. Ray, S. K. Pati and T. K. Maji, *J. Mater. Chem. A*, 2018, **6**, 5587–5591.
408 H. Liang, A. Acharjya, D. A. Anito, S. Vogl, T.-X. Wang, A. Thomas and B.-H. Han, *ACS Catal.*, 2019, **9**, 3959–3968.
409 K. Kinastowska, J. Liu, J. M. Tobin, Y. Rakovich, F. Vilela, Z. Xu, W. Bartkowiak and M. Grzelczak, *Appl. Catal. B Environ.*, 2019, **243**, 686–692.
410 Y. Dai, W. Li, Z. Chen, X. Zhu, J. Liu, R. Zhao, D. S. Wright, A. Noori, M. F. Mousavi and C. Zhang, *J. Mater. Chem. A*, 2019, **7**, 16397–16405.
411 L. Li, Z. Cai, Q. Wu, W. Y. Lo, N. Zhang, L. X. Chen and L. Yu, *J. Am. Chem. Soc.*, 2016, **138**, 7681–7686.
412 F. C. Krebs, R. B. Nyberg and M. Jørgensen, *Chem. Mater.*, 2004, **16**, 1313–1318.
413 C. Bracher, H. Yi, N. W. Scarratt, R. Masters, A. J. Pearson, C. Rodenburg, A. Iraqi and D. G. Lidzey, *Org. Electron.*, 2015, **27**, 266–273.
414 D. Cambié, C. Bottecchia, N. J. W. Straathof, V. Hessel and T. Noël, *Chem. Rev.*, 2016, **116**, 10276–10341.
415 M. B. Plutschack, B. Pieber, K. Gilmore and P. H. Seeberger, *Chem. Rev.*, 2017, **117**, 11796–11893.
416 F. Politano and G. Oksdath-Mansilla, *Org. Process Res. Dev.*, 2018, **22**, 1045–1062.
417 J. Shen, R. Steinbach, J. M. Tobin, M. Mouro Nakata, M. Bower, M. R. S. McCoustra, H. Bridle, V. Arrighi and F. Vilela, *Appl. Catal. B Environ.*, 2016, **193**, 226–233.
418 J. M. Tobin, T. J. D. McCabe, A. W. Prentice, S. Holzer, G. O. Lloyd, M. J. Paterson, V. Arrighi, P. A. G. Cormack and F. Vilela, *ACS Catal.*, 2017, **7**, 4602–4612.
419 L. Pessoni, S. Lacombe, L. Billon, R. Brown and M. Save, *Langmuir*, 2013, **29**, 10264–10271.
420 M. I. Burguete, F. Galindo, R. Gavara, S. V. Luis, M. Moreno, P. Thomas and D. A. Russell, *Photochem. Photobiol. Sci.*, 2009, **8**, 37–44.
421 Z. Xiang, H. Sun, Z. Zhu, W. Liang, B. Yang and A. Li, *RSC Adv.*, 2015, **5**, 24893–24898.

